



VYSOKÉ UČENÍ TECHNICKÉ V BRNĚ

BRNO UNIVERSITY OF TECHNOLOGY



FAKULTA CHEMICKÁ  
ÚSTAV CHEMIE MATERIÁLŮ

FACULTY OF CHEMISTRY  
INSTITUTE OF MATERIALS SCIENCE

## SURFACE ANALYSIS OF XGNP/PEI NANOCOMPOSITE

POVRCHOVÁ ANALÝZA NANOKOMPOZITU XGNP/PEI

DIPLOMOVÁ PRÁCE

MASTER'S THESIS

AUTOR PRÁCE

AUTHOR

Bc. JIŘÍ ČERVENKA

VEDOUCÍ PRÁCE

SUPERVISOR

prof. RNDr. VLADIMÍR ČECH, Ph.D.

BRNO 2012



Brno University of Technology  
**Faculty of Chemistry**  
Purkyňova 464/118, 61200 Brno 12

## Master's thesis Assignment

Number of master's thesis: **FCH-DIP0634/2011** Academic year: **2011/2012**  
Institute: Institute of Materials Science  
Student: **Bc. Jiří Červenka**  
Study programme: Chemistry, Technology and Properties of Materials (N2820)  
Study field: Chemistry, Technology and Properties of Materials (2808T016)  
Head of thesis: **prof. RNDr. Vladimír Čech, Ph.D.**  
Supervisors:

### Title of master's thesis:

Surface analysis of xGnP/PEI nanocomposite

### Master's thesis assignment:

- background research in polymer nanocomposites and interface/interphase phenomena
- surface modification using plasma etching
- SEM analysis, AFM analysis, nanoindentation

### Deadline for master's thesis delivery: 11.5.2012

Master's thesis is necessary to deliver to a secretary of institute in three copies and in an electronic way to a head of master's thesis. This assignment is enclosure of master's thesis.

-----  
Bc. Jiří Červenka  
Student

-----  
prof. RNDr. Vladimír Čech, Ph.D.  
Head of thesis

-----  
prof. RNDr. Josef Jančář, CSc.  
Head of institute

In Brno, 17.4.2012

-----  
prof. Ing. Jaromír Havlica, DrSc.  
Dean

## **ABSTRACT**

This Diploma thesis deals with surface analysis of nanocomposite foil – poly(etherimide) matrix (PEI) reinforced by exfoliated graphite nanoplatelets (xGnP). The PEI foil without reinforcement and separate xGnP particles were also analysed. Samples of the nanocomposite and the PEI foil were etched for various times by argon plasma. Scanning electron microscopy (SEM) was used to characterize xGnP agglomerates dispersed over silicon wafer and pristine/etched samples of PEI foil and nanocomposite xGnP/PEI foil. Graphite nanoplatelets were identified at surface of etched nanocomposite foil. Atomic force microscopy (AFM) was used for surface topography imaging of separate nanoplatelets and those uncovered at the surface of etched nanocomposite. Surface roughness (root mean square, peak to peak) of etched nanocomposite increased with prolonged etching time. Atomic force acoustic microscopy (AFAM) was used to characterize elastic anisotropy of etched nanocomposite. Nanoindentation measurements were employed to characterize the local mechanical properties of PEI and nanocomposite foils.

## **ABSTRAKT**

Tato Diplomová práce se zabývá povrchovou analýzou nanokompozitní folie polyetherimidu (PEI) vyztužené exfoliovanými grafitickými nanodestičkami (xGnP). Analyzovány byly také vzorky nevyztužené PEI folie a samostatné nanodestičky. Vzorky nanokompozitu a PEI folie byly plazmaticky leptány s využitím argonového plazmatu po dobu 1, 3 a 10 hod. Skenovací elektronová mikroskopie (SEM) byla použita pro charakterizaci samostatných nanodestiček rozptýlených na křemíkovém substrátu, původních či leptaných vzorků PEI folie a nanokompozitu. Nanodestičky byly identifikovány při povrchu leptané nanokompozitní folie. Mikroskopie atomárních sil (AFM) byla použita pro zobrazení povrchové topografie separovaných nanodestiček a odkrytých destiček při povrchu leptaného kompozitu. Povrchová drsnost (střední kvadratická hodnota, vzdálenost nejnižšího a nejvyššího bodu) leptaného nanokompozitu narůstala s prodlužující se dobou leptání. Akustická mikroskopie atomárních sil (AFAM) byla použita pro charakterizaci elastické anizotropie leptaných kompozitních vzorků. Nanoindentační měření umožnila charakterizaci lokálních mechanických vlastností PEI a nanokompozitních folií.

## **KEYWORDS**

Nanocomposite, poly(etherimide), scanning electron microscopy (SEM), atomic force microscopy (AFM), nanoindentation, nanoscratch test

## **KLÍČOVÁ SLOVA**

Nanokompozit, polyetherimid, skenovací elektronová mikroskopie (SEM), mikroskopie atomární síly (AFM), nanoindentace, nanovrypová zkouška

ČERVENKA, J; *Surface analysis of nanocomposite xGnP/PEI*, Brno, Faculty of Chemistry, Brno University of technology, 2012. 87 p. Supervisor prof. RNDr. Vladimír Čech, Ph.D.

#### *DECLARATION*

*I declare that the diploma thesis has been worked out by myself and that all the quotations from the used literary sources are accurate and complete. The content of the diploma thesis is the property of the Faculty of Chemistry of Brno University of Technology and all commercial uses are allowed only if approved by both the supervisor and the dean of the Faculty of Chemistry, BUT.*

.....  
student's signature

#### **Acknowledgments**

I would like to thank prof. RNDr. Vladimír Čech, Ph.D., Ing. Erik Pálesch, Ing. Lukáš Hoferek and Ing. Adam Bábík for valuable advice and comments.

Diploma thesis was supported by project P106/11/0738, Czech Science Foundation.

## **OBSAH**

1	INTRODUCTION.....	7
2	THEORETICAL PART .....	7
2.1	Nanocomposites .....	7
2.1.1	Basic characteristic .....	7
2.1.2	Types of nanocomposites .....	8
2.1.2.1	Nanolayered composites .....	8
2.1.2.2	Nanofilamentary and nanowire composites.....	9
2.1.2.3	Nanoparticulate composites .....	10
2.1.3	Interface/interphase in composites .....	11
2.2	Polyetherimide (PEI) .....	16
2.2.1	PEI chemistry .....	16
2.2.2	Physical properties of PEI .....	17
2.3	Graphite.....	18
2.4	Exfoliated graphite nanoplatelets (xGnP).....	19
2.4.1	xGnP nanocomposites .....	21
2.5	Surface analysis of nanocomposites .....	22
2.5.1	Optical microscopy (OM).....	22
2.5.2	Scanning electron microscopy (SEM).....	23
2.5.3	Atomic force microscopy (AFM).....	24
2.5.4	Nanoindentation (NI).....	29
2.5.5	Further methods for thin-film testing .....	30
3	AIMS.....	32
4	EXPERIMENTAL PART .....	32
4.1	Sample preparation .....	32
4.2	Optical microscopy .....	35
4.3	Scanning electron microscope .....	36
4.4	Scanning Probe Microscope .....	39
4.4.1	Scanning Probe Microscope basic setup .....	39
4.4.2	NTEGRA Prima specification .....	42
4.4.3	SPM probes.....	43
4.4.4	AFM imaging modes .....	44
4.5	Nanoindentation techniques.....	45
4.5.1	Introduction of Hysitron equipment .....	45
4.5.2	Nanoindentation measurements.....	47
4.5.3	Nanoscratch test.....	51
5	RESULTS AND DISCUSSION .....	53
5.1	Plasma etching and optical microscopy.....	53
5.2	Scanning electron microscopy .....	54
5.3	Atomic force microscopy.....	62
5.3.1	AFM analysis of separate xGnP .....	71
5.3.2	Atomic force acoustic microscopy (AFAM).....	73
5.4	Nanoindentation test .....	74
5.5	Nanoscratch test .....	77
5.6	Wear test .....	79

6	CONCLUSION .....	81
7	REFERENCES.....	82
8	LIST OF USED SYMBOLS AND ABBREVIATIONS .....	86

# 1 INTRODUCTION

Nanocomposites are very interesting group of materials. Their mechanical and physical properties predetermine it for many special applications. It exist a lot of kinds of nanocomposites, divided by used material of matrix, reinforcement and its geometry.

Carbon reinforced nanocomposites are one of the most investigated group of nanocomposites. Carbon fibres (CF), carbon nanotubes (CNTs) and their modifications (SWCNTs, MWCNTs, whiskers) and graphite particles can be used as reinforcement.

Last one of them is researched in this thesis. Nanocomposite composed from the conventional polymer poly(etherimide) (PEI) as a matrix reinforced by exfoliated graphite nanoplatelets (xGnP) in the form of thin film embodies crucial mechanical, optical, electrical and optoelectronic properties.

## 2 THEORETICAL PART

### 2.1 Nanocomposites

Nanocomposites can be defined as multiphase materials where one or more of the phases have at least dimension of order 100 nm or less. Most nanocomposites that have been developed and that have demonstrated technological importance have been composed of two phases.

Material of matrix is usually polymer, metal or ceramics. It depends on the applications of used materials. Reinforcement can be both organic and inorganic, in the form of layer, fibre or particle. [1]

In recent years, polymeric nanocomposites have attracted research interest both in industry and in academia, which represent a radical alternative to conventional filled polymers or polymer blends. The potential advantage of nanoreinforcements is that because of their small size, they can produce improved mechanical properties without degrading the energy absorption (impact) properties of the composites at the same time as is the case for conventional reinforcements. [2]

#### 2.1.1 Basic characteristic

As with conventional composites, the properties of nanocomposites can display synergistic improvements over those of a component phases individually. However, by reducing the physical dimension(s) of the phase(s) down to the nanometer length scale, unusual and often enhanced properties can be realized.

An important microstructural feature of nanocomposites is their large ratio of interphase surface area to volume. For example, in dispersions of layered clay (aluminosilicates) in nanocomposite polymers, this ratio can approach  $700 \text{ m}^2/\text{cm}^3$ , which is of order the area of a football field within the volume of a raindrop. This large surface area can result in novel and often enhanced properties that can be exploited technologically.

In terms of engineering applications, nanocomposites can be classified either as a functional materials (based on their electrical, magnetic, and/or optical behaviour) or as structural materials (based on their mechanical properties). [1]

The main advantages of using of nanoparticles as reinforcements are following. Failure of macroscopic specimens is primarily due the existence of critical size defects, i.e. material size decreases, the probability of critical size flaws decreases as well allowing the material to approach its intrinsic strength. Nanoparticles are more effective reinforcements than their

conventional counterparts because a smaller amount of nanoparticles could lead to a larger improvement in the mechanical properties of the polymer matrix. In addition, nanoparticles serve as a more efficient stress transfer medium to transfer the stress from the matrix to the reinforcements due to the increased surface area and good adhesion at the interface. [2], [3]

### **2.1.2 Types of nanocomposites**

Nanocomposites can be divided in light of used material for matrix and reinforcement, geometry of reinforcement and last but not least in light of applications.

Material of matrix is usually polymer, metal or ceramics. It depends on the applications of used materials. Reinforcement can be both organic and inorganic. Next paragraphs will engage by differentiation of nanocomposites in light of shape of reinforcement.

Nanocomposites can be microstructurally classified into three principal types, namely nanolayered composites composed of alternating layers of nanoscale dimensions, nanofilamentary composites composed of a matrix with embedded (and generally aligned) nanoscale diameter filaments and nanoparticulate composites composed of a matrix with embedded nanoscale particles. [1]

The most common nanoreinforcements used are layered silicate nanoclays and carbon nanotubes, however graphite platelets are also among the leading nanoscale fillers in research and development and commercial projects. [2]

Example on nanolayered filler is mica, clay or expanded graphite (EG). Carbon nanotubes (CNTs) or whiskers has a two-dimensional nanometer range and fumed silica dioxide or nanometallic particles are characterizes by three-dimensional nanometer range. [4]

#### **2.1.2.1 Nanolayered composites**

The ability to fabricate high quality artificially multilayered materials coincide with the advent of advanced thin film deposition methods. These methods allow the production of materials with precise control of the composition and thickness of the layers. Compared to conventional bulk laminate composites, the individual layer thicknesses can be reduced to atomic dimensions, resulting in the epitome of microstructural engineering. [1]

The characteristic microstructural length scale for nanolayered materials composed from of periodically alternating two phase layers is the bilayer repeat length (or bilayer period)  $A$ , equal to the combined thickness of two adjacent layers, (Fig. 1a).

Artificially multilayered materials composed of the layers of different phase are generically known as heterostructures, whether they consist of only a few layers or of many layers. Multilayers composed of many single crystal layers that posses the same crystal structure and where there is a perfect lattice matching at the surfaces (interphase interfaces) are called superlattices.

Most widespread group of these materials are metallic nanolayered composites. The requirement of metallic nanolayered composites that the layers be single crystals is often relaxed, so that a large grained, highly textured metallic multilayer is often referred to as a superlattice.

Most common method of producing inorganic nanolayered materials involves standard thin film deposition methods that have modified to allow for the alternate deposition of two or more different materials. Physical vapor deposition (PVD) methods, such as evaporation and sputtering, have been widely used to produce metallic, ceramic, and semiconductor artificially

layered thin films. It is useful when attempting to produce films composed of alternating metal and ceramic layers such as Al-Al<sub>2</sub>O<sub>3</sub>. This can be performed either by alternate sputtering from two different targets composed of the layer materials, or by sputtering from the single metal target (Al) while alternatively opening and closing a valve that bleeds in oxygen to reactively sputter the ceramic layer. Also, sputtering has been used to produce amorphous metallic and amorphous ceramic materials.

In the case of semiconductor films, such as GaAs/GaAl<sub>x</sub>As<sub>1-x</sub> superlattices are needed to fabricate high quality single crystal materials for most applications have required to use of molecular beam epitaxy (MBE). Process runs under ultra high vacuum conditions and generally a variety of in situ characterization methods, such as reflection high energy electron diffraction and Auger electron spectroscopy are available to monitor film deposition.

Pulsed laser deposition (PLD) involves the use of short pulse from a focused output of a laser to vaporize a material from a target and collect it onto a substrate inside a vacuum chamber. An important feature of PLD is that it allows deposition of a multicomponent material from a target of the same composition, and therefore has become a popular method to produce ceramic systems such as high temperature semiconductors and ferroelectrics. Multiple targets are used to deposit multilayered films.

Polymer multilayers where the layers have different refractive indices have been produced. They reflect ultraviolet or near-infrared radiation as well as displaying iridescent colour effects.

Coextruded polymer multilayers composed of alternating brittle and ductile materials have displayed increased fracture toughness that makes them attractive for heavy-duty wrapping and packaging materials. [1]

### ***2.1.2.2 Nanofilamentary and nanowire composites***

Nanofilamentary composites are generally associated with mechanical processing methods to produce materials with enhanced mechanical strength as well as other properties.

They can be considered as wires that are composed of a metal matrix with aligned second phase metal filaments (Fig. 1b).

They are produced by starting with a bulk two-phase ingot produced using conventional metallurgical fabrication methods such as casting or powder processing. Nanofilamentary composites often display significantly enhanced tensile strength as well as high electrical conductivity. As an example it is possible specify Cu/Nb, where Nb is superconductor. Because of this behaviour, these nanocomposites have applications as windings for high field pulsed magnets.

Nanowire composites are often referred to as an embedded nanowire array and are generally produced by electrodeposition in a compliant matrix. The interest of these materials is in functional properties of the nanowires. Behaviour of these materials is generally associated with quantum confinement effects. With regard to producing composites involving a matrix with embedded and aligned nanowires, electrodeposition has become an extremely important synthesis method. This approach uses a nanoporous membrane such polycarbonate. The pores are produced by exposing the membrane to a radioactive source that creates nuclear tracks that are subsequently etched. In this way, it is possible to form high aspect ratio pores with diameters down to tens of nanometers. Prior to electrodeposition, a thin layer of an electrical conductor such as gold is deposited by, e.g., sputtering, on one side of the membrane. This conductive layer is used as an electrode in an electrochemical cell.

During the plating, the pores are filled with the deposited material, resulting in an array of nanowires within the membrane. Examples of potential applications for these systems include field emitter areas for flat panel displays and magnetic data storage.

The extraordinary electrical, thermal and mechanical properties of carbon nanotubes (CNTs) make them promising candidates as fillers for conducting polymer composites, capable of dissipating electrostatic charges and of shielding devices from electromagnetic radiation. In the fabrication of composite materials, good dispersion and interfacial adhesion of nanofillers with the polymer matrices play important roles towards obtaining composite materials with anticipated and reproducible properties and performances. CNTs have been used to modify many polymers, but one of the most serious drawbacks in developing CNT composites is that CNTs are expensive due to low yield, low production and purification rates commonly associated with all of the current CNT preparation processes. [1], [5], [6]

### 2.1.2.3 Nanoparticulate composites

These materials are composed of nanoscale metal particles embedded in an immiscible metal, ceramic, or semiconductor matrix. Since that time, there has been an explosion in the number and types of systems that have been developed and investigated, involving a wide variety of processing approaches (Fig. 1c).

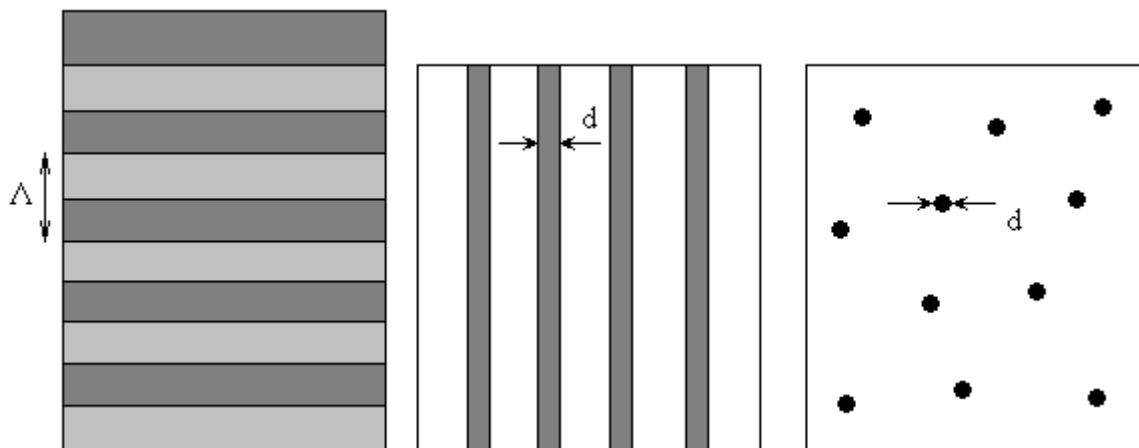


Fig. 1: Scheme of a) nanolayered composite, b) nanofilamentary, c) nanoparticulate composite [1]

As with other types of nanocomposite materials, thin film processing methods have been used extensively to produce nanoparticulate composites. Granular metals have been generally produced by simultaneous thin film deposition of two immiscible phases by, for example evaporation or sputtering. [1]

Recently, other novel processing routes to producing metal-based nanoparticulate composites have been developed. One approach involves partially devitrifying bulk metallic glasses. This can be performed by annealing the glassy precursor or by direct quenching from the liquid state. The materials produced are composed of nanoscale metal crystals embedded in an amorphous metal matrix. Another processing approach involves self-assembly of nanoscale particles. This method has been used to produce three-dimensional FePt/Fe<sub>3</sub>O<sub>4</sub> nanocomposite assemblies. [1]

A variety processing routes has been developed to fabricate ceramic-based nanocomposites, such as  $\text{Al}_2\text{O}_3/\text{SiC}$ , where particles of carbide are used to reinforce the alumina for structural material applications. One common approach involves powder processing, where mixtures of ultrafine powders of the two phases are homogenized by, for example, wet ball milling in an organic or aqueous medium. After drying of the slurries, the nanocomposite is consolidated; this has been generally performed by hot-pressing. Other approaches have been developed, for example pyrolysis of a silicon-containing polymer precursor. Sol gel processing has also been investigated. Boehmite gels are used as a source of alumina that is either coated onto SiC particles or mixed with SiC precursor polysilastyrene. After drying and calcination, the powder is consolidated by hot-pressing.

Polymer-based nanocomposites for structural and functional material applications have received a great deal of recent attention. In terms of commercial importance, structural nanocomposites produced by using layered clay minerals, such as montmorillonite and hectorite are the most significant. The layered clay (aluminosilicates) materials are synthesized by mixing the layered clay with the monomer, followed by polymerization, by melt mixing the layered clay with the polymer, or by mixing the layered clay with a solvated polymer followed by solvent removal. Other types of commercially important nanocomposites are thermoplastics reinforced with carbon nanotubes formed by extrusion and injection molding. The high modulus and tensile strength of carbon nanotubes make them extremely attractive filler materials for nanocomposite polymers. [1]

### **2.1.3 Interface/interphase in composites**

It is thin border layer on the interface fibre-polymer determining an amount of transferring of load from matrix to structure of reinforcing fibres. Thus interphase is crucial for general endurance of composite structure against the impingement of outer ambient. In the case of full adhesion of fibres to polymer matrix is all loading in composite supported by reinforcing fibres and deformable matrix is almost not stressed.

Interphase can be controlled or uncontrolled. In the case of uncontrolled reinforcement fibres are not surface modified and polymer matrix could be or need not influenced by presence of fibres. Character of interphase chemical structure is same as a polymer but with different microstructure. Thickness of uncontrolled reinforcement is in range from 1 to 100 nm. Adhesion of not modified fibres is with regard to matrix commonly bad. In comparison with controlled interphase, (Fig. 2) realised as a deposition of a thin reactive layer on the surface of reinforcing fibre allows much better adhesion of fibre to matrix and simultaneously allows bonding both to matrix and fibres. Deposited layers have defined structure and properties. Special surface treatments realised abreast with producing of fibres can be ranked among them. Real composite has also both controlled and uncontrolled interphases. [7]

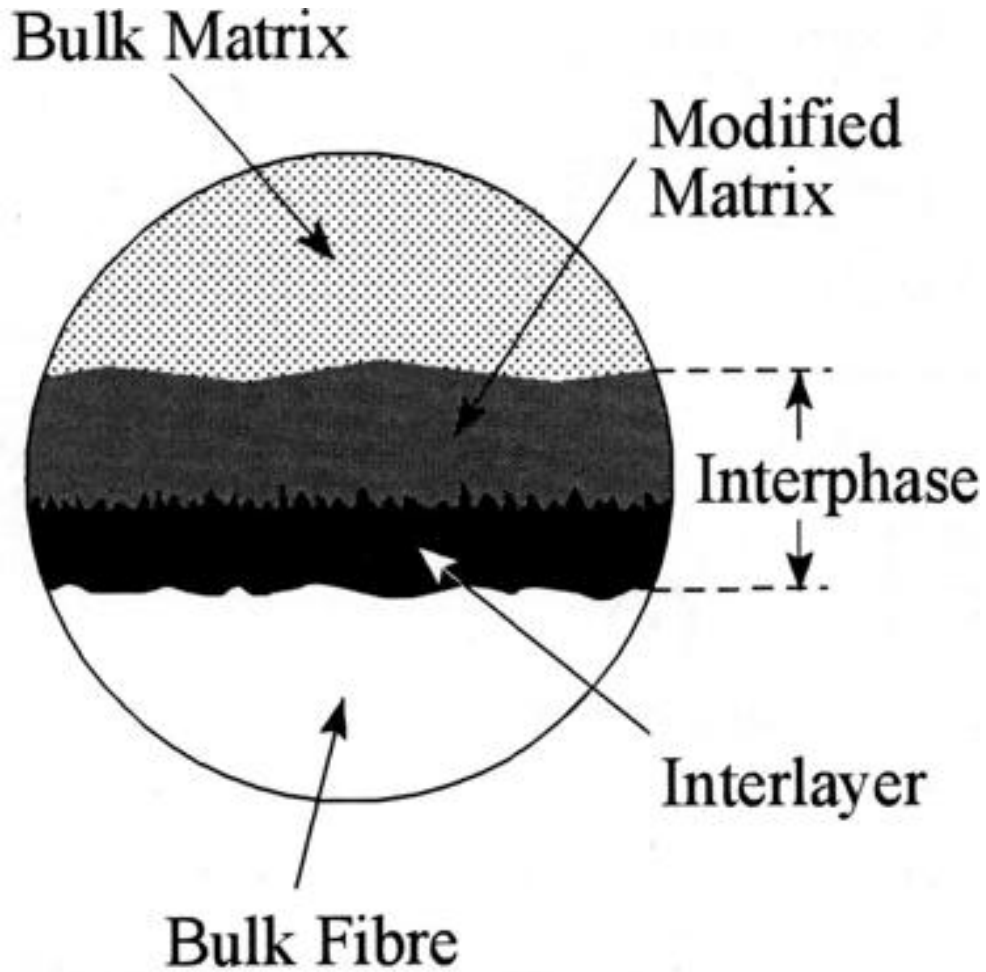


Fig. 2: Scheme of surface modified composite interphase [7]

Materials with good mechanical properties have usually controlled interphase for optimal transfer of load. Adhesion between reinforcing and matrix could be divided into two parts: interface between fibre and interlayer and interphase between interlayer and matrix. Adhesion is primarily caused by van der Waals forces, although other types of bonding may reinforce these. [7]

Important presumption for good adhesion is full contact of surfaces of two materials on atomic level. In the case of liquid and solid we discuss about wetting of solid material (fibre) by liquid (polymer). If we make a drop on the surface of bulk material, after exact time it takes place equilibrium establishment between cohesive forces in liquid and adhesive forces between solid and liquid and resulting contact angle  $\theta$  characterizes surface wetting of solid by liquid (Fig. 3) Equilibrium of horizontal components in point on the ledge of drop is expressed by Young's equation

$$\gamma_l \cos\theta = \gamma_s - \gamma_{sl}, \quad (1)$$

where  $\gamma_l$  is surface energy of liquid (surface tension),  $\gamma_s$  is surface energy of solid and  $\gamma_{sl}$  is surface energy of interface of solid and liquid. This equation demonstrates that the more surface energy of solid and the less surface energy of interface will be, the less contact angle

will be. It exist two extremes. The first is when  $\gamma_s = \gamma_l$  and  $\gamma_{sl} = 0$  and contact angle  $\theta = 0^\circ$ , it is agree with ideal wetting. In the second extreme when liquid is not in interaction with solid,  $\theta = 180^\circ$ . [8]

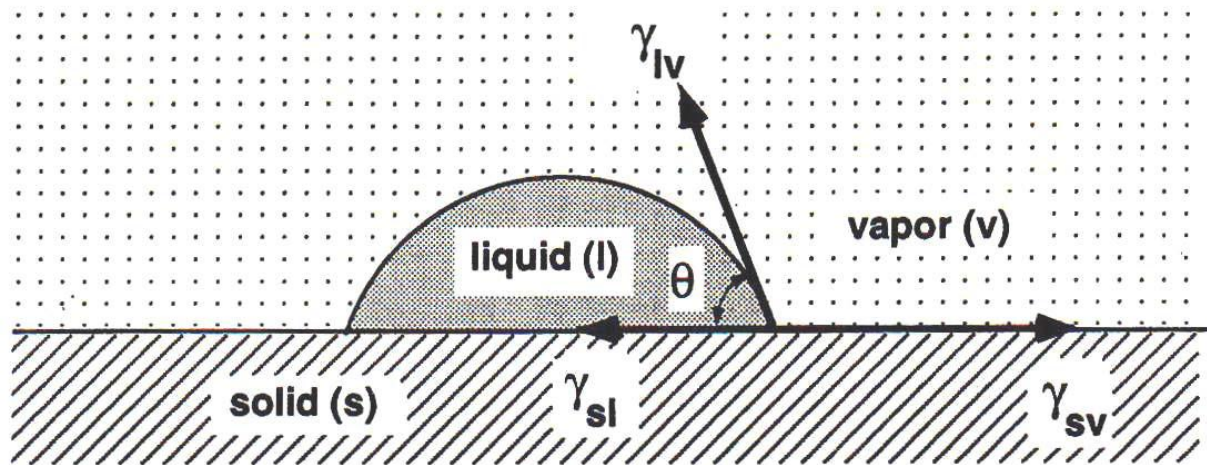
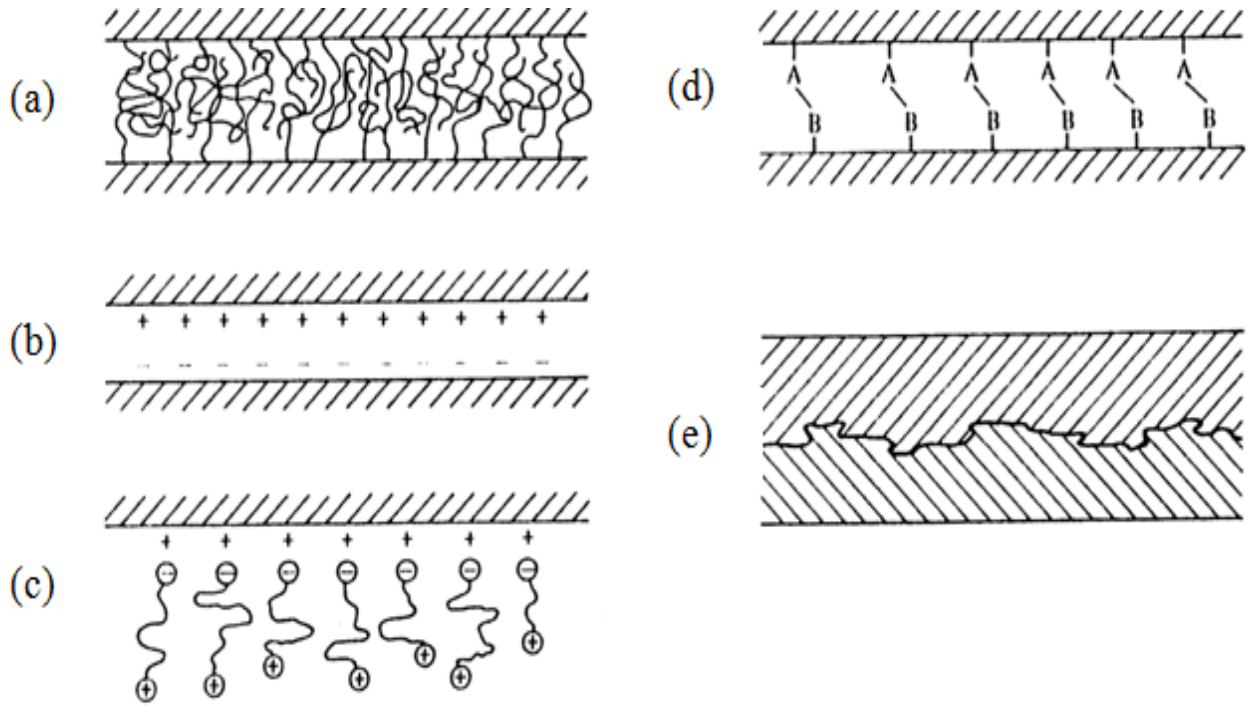


Fig. 3: Wetting of solid material by liquid [8]

In the interface region are possible a lot of types of bonding mechanisms. One of them is interdiffusion and chemical reaction. Various types of diffusional process which promote adhesion can take place at interface. Fig. 4a shows the diffusion of free chain ends at the interface between two polymers, which leads to chain entanglements and a rise in the adhesive strength. This effect is employed in some coupling agents used on fibres in thermoplastic matrices. Interdiffusion can also take place in non-polymeric, particularly if it is accompanied by a chemical reaction. The adhesive strength depends on the nature of the resultant interatomic bonds. Various types of chemical reaction may occur at the interface, either deliberately promoted or inadvertent. These can be represented as a Fig. 4d, by new A–B bonds being forms as a result of interfacial reactions. [8]

Electrostatic attraction is takes place, when the surfaces carry net electrical charges of opposite sign, (Fig. 4b), then a sustained adhesive force may result. This effect is utilised in the certain fibre treatments, as in the deposition of coupling agents of glass fibres. The surface can exhibit anionic or cationic properties, depending on the oxide in the glass and the pH of the aqueous solution used to apply the coupling agents. Thus, if ionic functional silanes are used, it is expected that the cationic functional groups will be attracted to an anionic surface and vice versa (Fig. 4c). [8]

Mechanical keying takes place, when is a contribution to the strength of the interface from the surface roughness of the fibres if good wetting has occurred, (Fig. 4e). The effects are much more significant under shear loading than for decohesion as a result of tensile stresses. Some improved resistance to tensile failure results if re-entrant angles are present and there is an increase in strength under all types of loading as a consequence of the increased area of contact. [8]



*Fig. 4: Interfacial bonds formed by (a) molecular entanglement following interdiffusion, (b) electrostatic attraction, (c) cationic groups at the end of molecules attracted to an anionic surface, resulting in polymer orientation at the surface, (d) chemical reaction and (e) mechanical keying [8]*

Development of using thin layers for surface treatments of fibres is in parallel with development of applications of composite materials. Aim of these treatments is assuring of better wetting and covalent bond fibre-matrix. Thin layers, which fulfil these conditions, are termed as coupling agents. Glass fibres are the most explored for this application. For surface treatments are most often used organosilicates (silanes), but investigated alternative is also chemical grafting. Nowadays applications of thin layers of plasma polymers are developed. Plasma polymers have wide range of applications. [8]

Some of oxides in glass, such as  $\text{SiO}_2$ ,  $\text{Fe}_2\text{O}_3$  and  $\text{Al}_2\text{O}_3$ , form links to hydroxyl groups during contact with water molecules, so that glass picks up water very rapidly. In time, this can leach out other species in the glass, notably Na and Ca, to leave a weak, porous surface. The primary function of the coupling agents is to provide a strong chemical link between the oxide groups on the fibre surface and the polymers molecules of the resin. A wide variety of coupling agents have been developed but the principles can be illustrated by the simple example shown in Fig. 7. This refers to the silane coupling agents, which have the general chemical formula  $\text{R-Si-X}_3$ . This is the multifunctional molecule which reacts at one end with the surface of the glass fibre and at the other side with the polymer phase. The X units represent hydrolysable groups such as the ethoxy groups ( $-\text{OC}_2\text{H}_5$ ). The silane is hydrolysed to the corresponding silanol (Fig. 5a) in the aqueous solution to which the fibres are exposed. These silanol molecules compete with water molecules to form hydrogen bonds with the hydroxyle groups bound to the fibre surface (Fig. 5b). When the fibres are dried, the free water is driven off and condensation reactions then occur, both at the silanol/fibre junction and between neighbouring silanol molecules, see on the Fig. 5c. The result is

a polysiloxane layer bonded to the glass surface, presenting an array of R groups to the environment.

This coating is water-resistant and can also form a strong bond to the polymer matrix. If the matrix is to be a thermosetting resin, then an R group is chosen which reacts with the resin during polymerisation, thus forming a permanent link. For a thermoplastic matrix, on the other hand, all the covalent links have been formed during manufacture of the polymer. However, choice of R with a fairly short chain which can interdiffuse with the chains of the matrix allows the strong bond to form. [8]

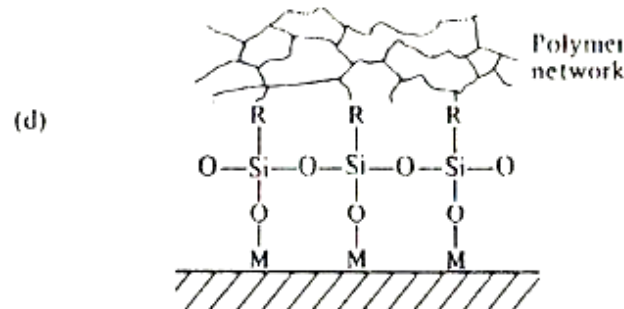
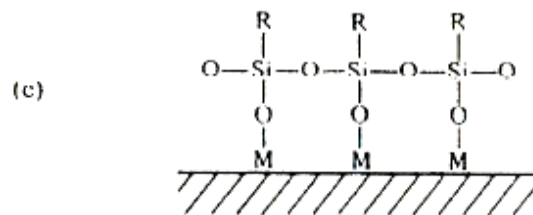
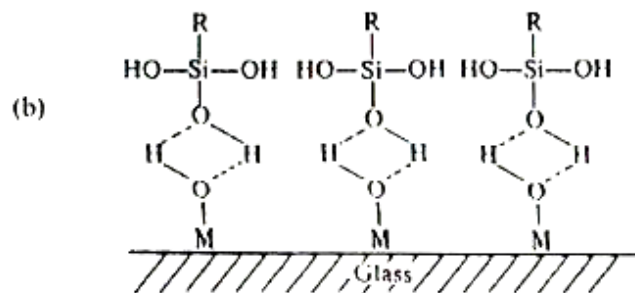


*Fig. 5: Silane coupling agents (a) hydrolysis of an organo-silane to the corresponding silanol, (b) hydrogen bonding between hydroxyl groups of the silanol and those attached to the glass surface, (c) polysiloxane bonded to the glass after condensation reactions during drying and (d) bonding between the functional group R and the polymer matrix [8]*

In the presence of small quantities of water, surfaces may be able to slide past each other without permanent bond failure. For metal matrix composites (MMCs), it is less common for the promotion of good bonding to be necessary, because some local chemical reaction often occurs naturally during fabrication. There are, however, some systems in which wetting is very poor and coatings have been to improve this. For ceramic matrix composites (CMCs),

although various types of bondings have been developed, these are rarely designed to improve wetting or adhesion. Fibres are normally added to ceramic matrices in order to improve the toughness and a relatively low debonding stress is usually preferred to promote frictional sliding during fibre pull-out. [8]

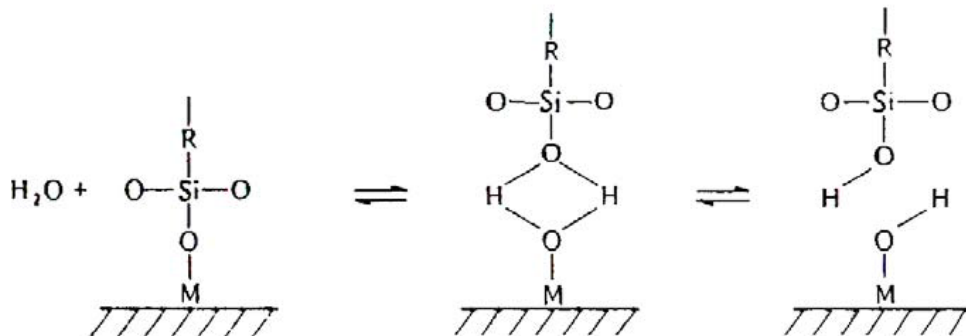


Fig. 6: Mechanisms of reversible bond formation associated with hydrolysis [8]

## 2.2 Poly(etherimide) (PEI)

Specialty engineering thermoplastics are used as matrices for advanced composites because of their additional advantages such as higher specific strength, thermal stability, resistance to fatigue and crack, recyclability, unlimited shelf life, etc. In such composites, its role is to stabilize the fibres in compression (providing lateral support), translate the fibre properties into the laminate, minimize damage due to impact by exhibiting plastic deformation, and provide out-of-plane properties to the laminate. [5], [9]

Aromatic poly(imides) (PIs) are versatile engineering polymers that have been widely used in many advanced technology applications due to their outstanding thermal stability, mechanical properties, and low dielectric constants. However, PIs are difficult to process and the research in the last few years has been directed toward novel linear polymers that are soluble in organic solvents or melt-processable when fully imidized. The most important of them, based on the production figures, are poly(etherimides) (PEIs). Poly(etherimide) (PEI) is a high performance, high temperature ( $T_m \sim 380\text{--}400\text{ }^\circ\text{C}$ ) versatile polymer that possesses good tribological properties. PEI resins are advanced polymers developed by General Electric Co. These polymers are amorphous thermoplastic materials that result from the combination of ether units and aromatic imides. Ether units supply the chain flexibility and good melt flow characteristics to PEI, while the aromatic imide units provide thermal resistance and mechanical properties. One commercialized PEIs is Ultem<sup>®</sup> 1000, which is synthesized via the polycondensation of a dianhydride, 4,4' - (4,4' isopropylidene diphenoxy) bis(phthalic anhydride), with *m*-phenylene diamine (*m*PDA). Although Ultem 1000 has good melt processability and solubility in some solvents, its relatively poor thermal stability limits its application in the aerospace and automotive fields. [10], [11]

### 2.2.1 PEI chemistry

Poly(etherimide) is synthesized by sol-gel process. One of commercial types is PEI Ultem 1000. Poly(etherimide) was synthesized by reacting *m*-phenylenediamine (*m*PDA) with 4,4'-(4,4'-isopropylidene diphenoxy) bis(phthalic anhydride) (BPADA). Poly(amic acid)

PAA was first synthesized as described above. 20 ml of toluene was then added and the mixture was heated to ~160 °C at reflux for ~12 h until the water was azeotropically distilled off via a Dean-Stark trap. Heating was continued to distill off the residual toluene. After the completion of polymerization, the viscous PEI solution was cooled, and the polymer solution was ready for the preparation of nanocomposites. [10]

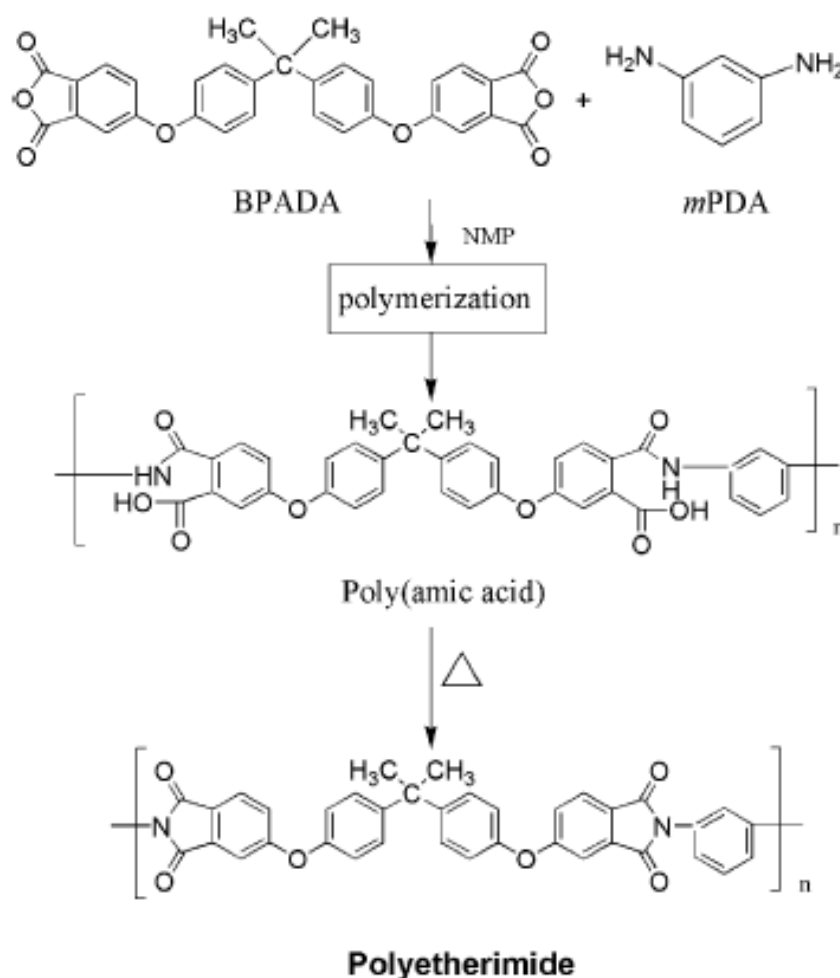


Fig. 7: Scheme of PEI preparation [10]

### 2.2.2 Physical properties of PEI

Poly(etherimide) (PEI) is a type of high performance thermoplastic with high modulus and strength, and also exhibits superior high temperature stability. It performs successfully in aerospace, electronic and other applications under extreme conditions. Widening its field of applications would be readily embraced by many industry sectors. However, when PEI is combined with nanoparticles, for example when developing an electrically conductive polymer, its extremely high viscosity severely impedes the uniform dispersion of nanoparticles and makes processing the nanocomposite challenging. PEI exhibits 60 % elongation to break, it not not a very ductile polymer. In the Table 1 we can see some of the physical properties. [5], [12]

Table 1: Some physical properties of PEI [12]

Properties	Standard	Value
Density (g/cm <sup>3</sup> )	ASTM A 792	1.27
Tensile strength (MPa)	ASTM 638	105
Tensile modulus (GPa)	ASTM 638	3
Elongation at break (%)	ASTM 638	60
Flexural strength (MPa)	ASTM 790	150
Flexural modulus (MPa)	ASTM 790	3.3
Glass transition (°C)		215
Melting point range (°C)		380-400

### 2.3 Graphite

Graphite is a layered material composed of weakly bonded large number of graphene sheets which are held together by van der Waals forces with a large aspect ratio. Carbon atoms are in hybridized state with  $sp^2$  configuration. The carbon atoms are bonded covalently in a hexagonal arrangement within the layer. The  $\alpha$ -spacing between the carbon layers is 0.335 nm. Since the van der Waals forces are relatively weak, it is possible for a wide range of atoms, molecules and ions intercalate between graphite layers to form graphite intercalation compounds (GICs). Single crystal graphite is one of the stiffest materials in nature with an elastic modulus of over 1 TPa, which is many times greater than nanoclay. Unlike clay, graphite is thermally and electrically conductive. It also has a lower density than clay. Graphite has been known as a host material for many chemicals, including metal halides, metal oxides, and mineral acids. [2], [13], [14]

Expandable graphite (EG), which is also called acid-intercalated graphite flake, can be expanded up to the hundreds of times over its initial volume at high temperature, resulting in separation of the graphene sheets at the nanoscopic level along the  $c$  axis of graphene layers. During the last several years, a number of papers have studied material preparation and characterization of various polymer nanocomposite systems reinforced with EG. Expanded graphite is generally produced by using  $H_2SO_4$ -GICs.  $H_2SO_4$ -GICs are widely used for the exfoliation process, because they can give a high expansion volume during thermal treatment. EG maintains the layered structure similar to the natural graphite flake, but produces tremendous different size of pores and nanosheets with very high aspect ratio. [6], [15]

One layer of graphite structure is graphene. It is a two-dimensional semimetal with a tiny overlap between valence and conductance bands. It was discovered in 2004 by the group of Professor Andre Geim at Manchester. It is a one-atom-thick planar film of  $sp^2$ -bonded carbon atoms which are densely packed in a honeycomb crystal lattice. It is the basic structural element of all other graphite materials. Graphene has remarkably high electron mobility at room temperature, as compared to those of silicon-based semiconductors. Since the identification of graphene in 2004, discoveries have been made to demonstrate graphene-based single-atom-layer transistors and chemical nanosensors for single-molecule gas detection. The electron mobility-related resistivity of graphene is about 35 percent less than that of copper, which is known to be the least resistive material at room temperature. Owing

to its super mechanical electronic properties, graphene is predicted to be a very promising material for widespread applications at various scales, ranging from macroaircraft to microdevices. [14], [16]

## 2.4 Exfoliated graphite nanoplatelets (xGnP)

Recently, the two-dimensional carbon graphene has attracted great attention, due to its exceptionally high crystal and electronic quality. Growth of large area of high-quality graphene was developed on metal substrates, and individual graphene sheets can be also prepared by micromechanical cleavage. Unfortunately, these approaches are technically complex and difficult to mass production. In addition, these two-dimensional crystals cannot theoretically exist in the free state. The most commonly used nano sized form of graphite nanoplatelets, which have a few layers of graphene sheets stacked together and are produced by the exfoliation of graphite via an acid intercalation, followed by ultrasonic irradiation to isolated graphite nanosheets. [5], [17]

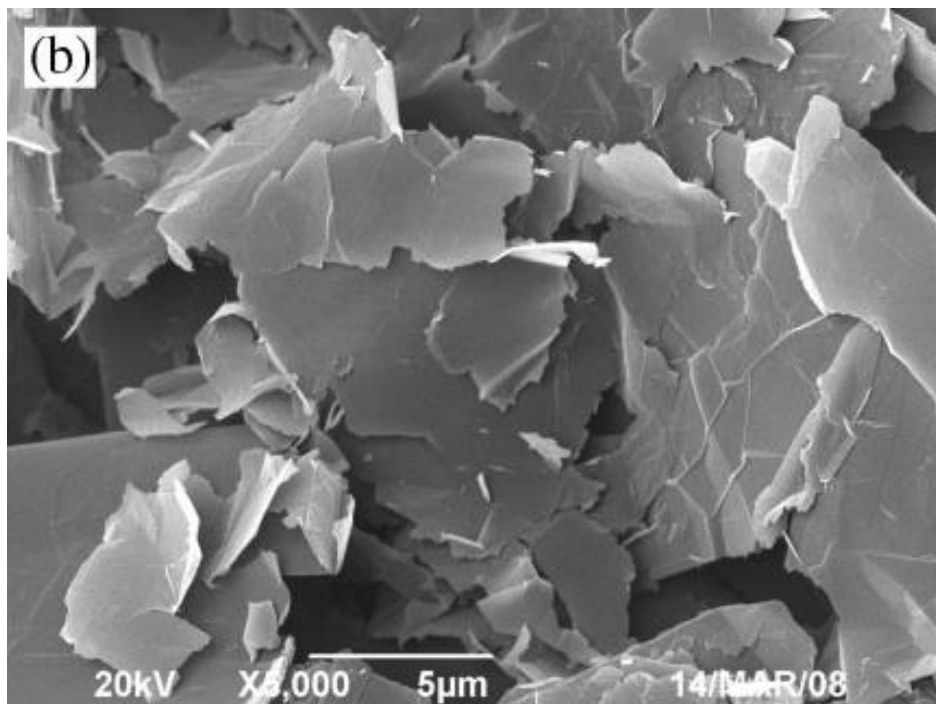
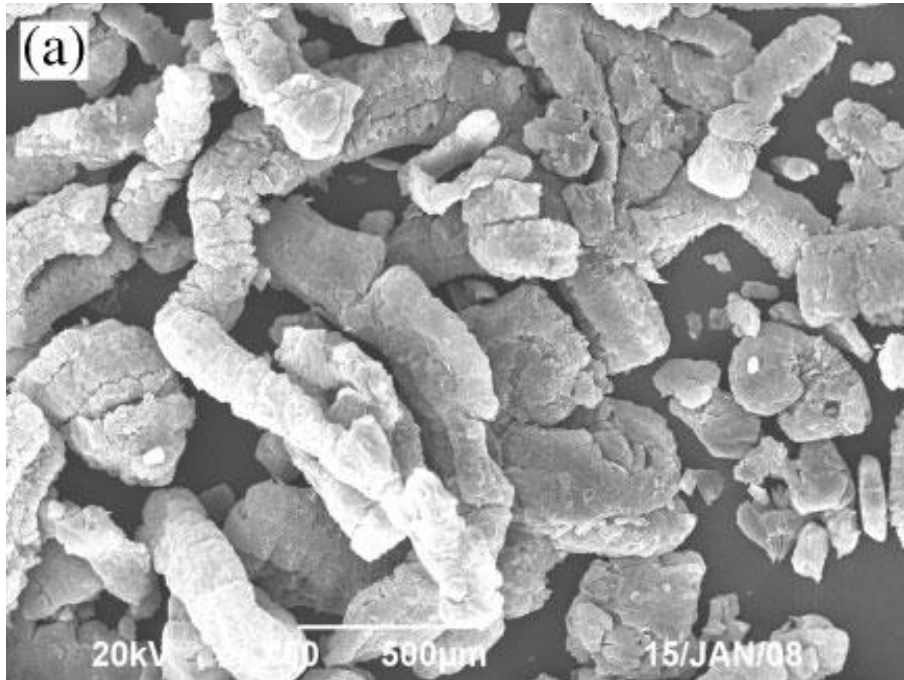
Research at Michigan State University (MSU) has led to process that can successfully produce exfoliated graphite nanoplatelets (xGnP), which are 1–10 nm in thickness and from 100 to 1000 nm in diameter. The surface of graphite nanoplatelets is pure graphene where the carbon is in  $sp^2$  configuration. This presents a uniformly homogeneous and moderately energetic surface that has been shown to be an excellent nucleating surface for both polar and nonpolar polymers. Furthermore, these graphite nanoplatelets possess the high electric conductivity of graphene. [6], [13], [15]

Exfoliated graphite nanoplatelets (xGnP) combining the layered structure and low price of nanoclays with the superior mechanical, electrical and thermal properties of carbon nanotubes (CNTs) are very cost effective and can simultaneously provide a multitude of physical and chemical property enhancements. xGnP–reinforced thermosetting and thermoplastic polymer nanocomposites showed excellent mechanical and electrical properties. xGnP can be effective alternatives to CNTs and still provide excellent and competitive functional properties. [2], [3]

Exfoliated graphite nanoplatelets (xGnP) can be prepared by intercalation on natural graphite followed by rapid exfoliation in a microwave environment. Intercalation takes place in the presence of sulphuric and nitric acid. Nitric acid acts as oxidizer while sulphuric acid acts as intercalate. [18] The graphite rapidly heats as a result of coupling with the microwave radiation and the entrapped intercalants vaporize. The exfoliated graphite particles undergo significant expansion (500×) forming a worm-like structure (Fig. 8a). This worm-like structure is then mechanically grounded to form the individual graphite nanoplatelets which have the thickness less than 5 nm and a diameter around 15  $\mu\text{m}$  (xGnP-15) (Fig. 8b). xGnP-15 can be further reduced in diameter by vibratory milling, resulting in graphite nanoplatelets in the same thickness but having the diameter about 1  $\mu\text{m}$  (xGnP-1). Dimensions of xGnP can be determined by TEM. Two types of xGnP mentioned above, have same thicknesses and can consist from more than ten grapheme sheets. Taking into account that the basal plane distance of graphite is 0.335 nm it is estimated that the average thickness of the graphite nanoflakes is 5–10 nm with a distribution of platelets having thicknesses in the nanometer range expected. On Fig. 8c is TEM image side view of xGnP. Table 2 summarizes the basic dimensional data of these carbon materials. [5], [16], [17]

Table 2: Basic dimensional data of xGnP [18]

Carbon material	Length [ $\mu\text{m}$ ]	Thickness [nm]	Aspect ratio	Surface area [ $\text{m}^2 \cdot \text{g}^{-1}$ ]
xGnP-1	0.86	5–10	86	$94 \pm 5$
xGnP-15	15	5–10	$\sim 1500$	$105 \pm 7$



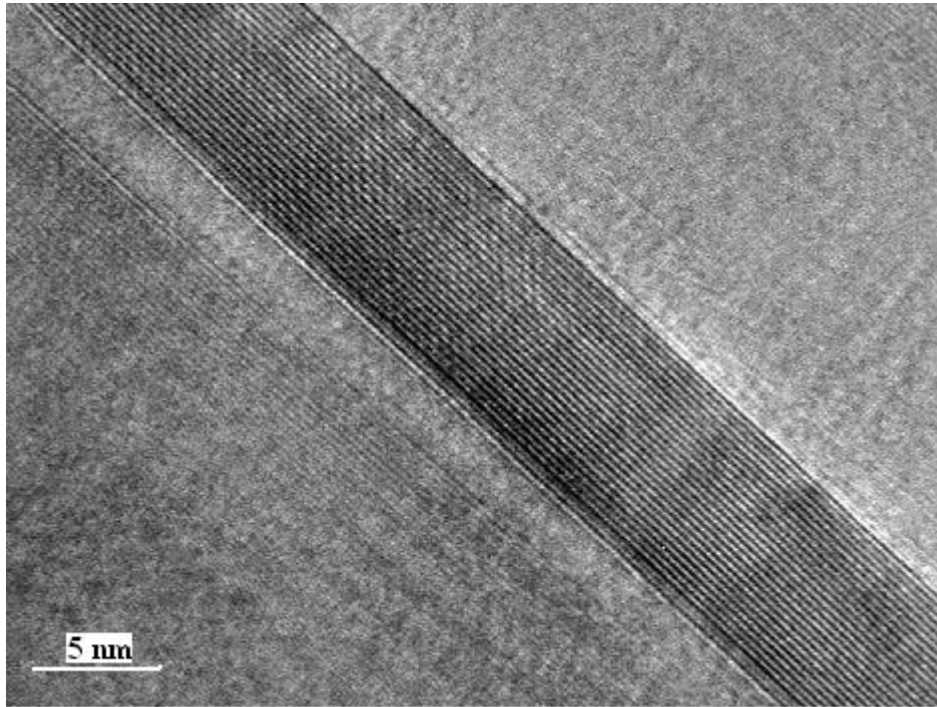


Fig. 8 a) SEM image of worm-like exfoliated graphite (EG) particles, b) SEM image xGnP, c) TEM image of side view of xGnP [13], [19]

#### 2.4.1 xGnP nanocomposites

Graphite nanocomposites can offer advanced properties such as electrical and thermal conductivity at reasonable cost. If the appropriate process conditions are applied, graphite nanocomposites offer the potential to produce materials with excellent mechanical, electrical, and thermal properties at reasonable cost, which opens up many new applications. Thus, graphite nanoflakes offer an alternative source for producing nano-scale materials for producing polymer nanocomposites. Since late 1990's, there are multiple reports of intercalated, expanded, or exfoliated graphite nanoflakes that were added to polymer systems to fabricate graphite nanocomposite materials. [18]

The most heavily studied graphite oxide (GO) or GNP – polymer composite systems have been poly(methylmethacrylate) (PMMA) and poly(styrene) (PS) based composites. Also studied were composites based on other matrices, including nylon, poly(propylene), poly(arylenedisulfide) and epoxy resins. In the most of these investigations, composites were prepared via monomer intercalation of exfoliated graphite (mostly GO), followed by polymerization. In all cases, graphite was intercalated in an acid-oxidizer mixture solution, which was thermally exfoliated at a temperature typically in the range 800–1100 °C.

Combination of PEI/xGnP composites allows better results than with single-wall or multi-wall carbon nanotubes (SWCNTs, MWCNTs), especially electrical resistivity and thermal conductivity. [11]

The use of exfoliated graphite flakes (xGnP) in composites opens up many new applications where electromagnetic shielding, high thermal conductivity, gas barrier resistance or low flammability is required. [20]

## 2.5 Surface analysis of nanocomposites

### 2.5.1 Optical microscopy (OM)

Optical microscopy (OM) is microscopic techniques, which creates images by classical technique, i.e. at once with using lenses. Basic parts of the optical microscope are illumination and imaging system. Sample is located on the path of light between illumination and imaging system. Lighting system consists of a light source and condenser lens, the imaging system of objective lens and ocular. The image is directly observed by eye, photographic film or digital camera. Part of imaging system can be also a beam splitter, which divides the beam, which can then be observed in several ways at once or both eyes simultaneously (binocular microscope). The binocular microscope is necessary to have in mind that both eyes see the same image cannot be confused with microscope, which have two independent optical systems and allow observation of the spatial image. Lighting and imaging system is stored in a tube, into which the possibility of introducing other elements, such a various compensators, filters, optical plates, etc. Special type of OM is Polarized optical microscopy (POM). Polarizing microscopes tend to have a two polarizing filters, one of them, called the polarizer, which is stored in condenser, can illuminate a sample of linearly polarized light. The second one, called analyzer, is stored in imaging system. Crossing both filters allows to see depolarization of light caused by the sample. The reason may be the presence of double quarry departments or units of the interface between different refractive indices. Scheme of imaging process in optical microscope is below (Fig. 9). [21]

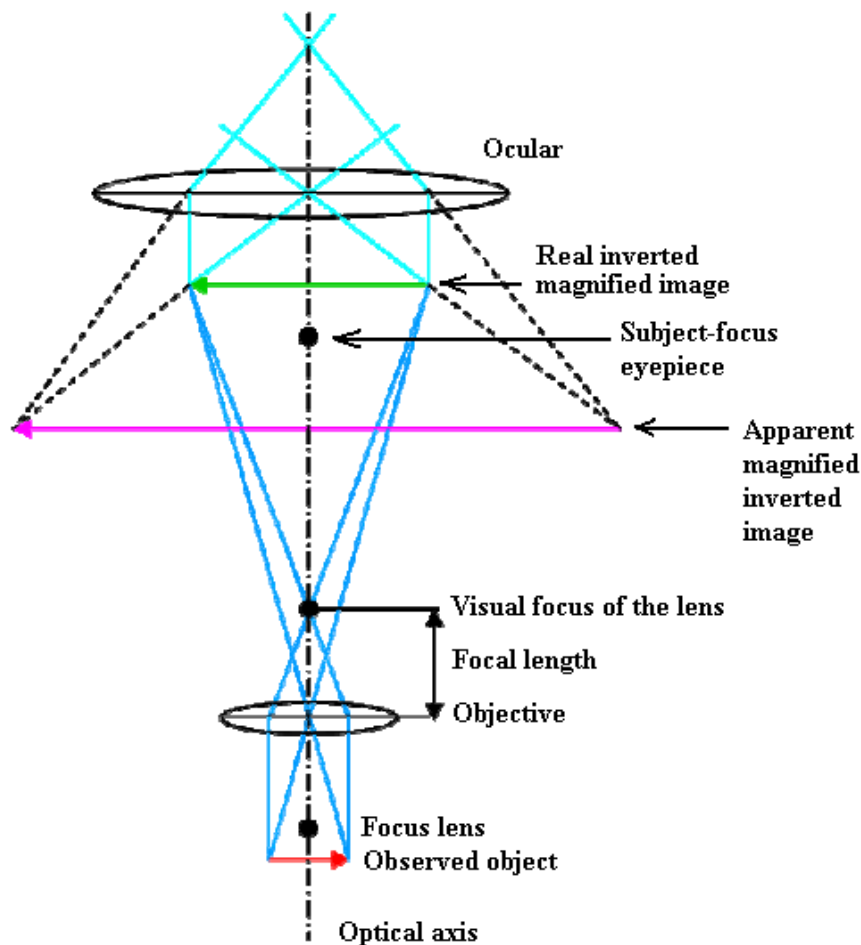


Fig. 9: Scheme of image formation in optical microscope [21]

## 2.5.2 Scanning electron microscopy (SEM)

Scanning electron microscopy is perhaps the most widely employed thin-film and coating characterization instrument. Small portion of the total image is probed in SEM at any instant and the image builds up serially by scanning the probe. Strictly speaking, the SEM has more in common with the Auger electron spectroscopy (AES) and Secondary-ion mass spectrometry (SIMS). A schematic of the typical SEM is shown in Fig. 10. Electrons thermionically emitted from a tungsten or LaB<sub>6</sub>-cathode filament are drawn to an anode and focused by two successive condenser lenses into a beam with a very fine spot size that is typically 10 Å in diameter. Pairs of scanning coils located at the objective lens deflect the beam either linearly or in raster fashion over a rectangular area of the specimen surface. Electron beams having energies ranging from a few keV to 50 keV, with 20 keV a common value, are utilized. Upon impinging on the specimen, the primary electrons decelerate and in losing energy, transfer it inelastically to other atomic electrons and to the lattice. [22]

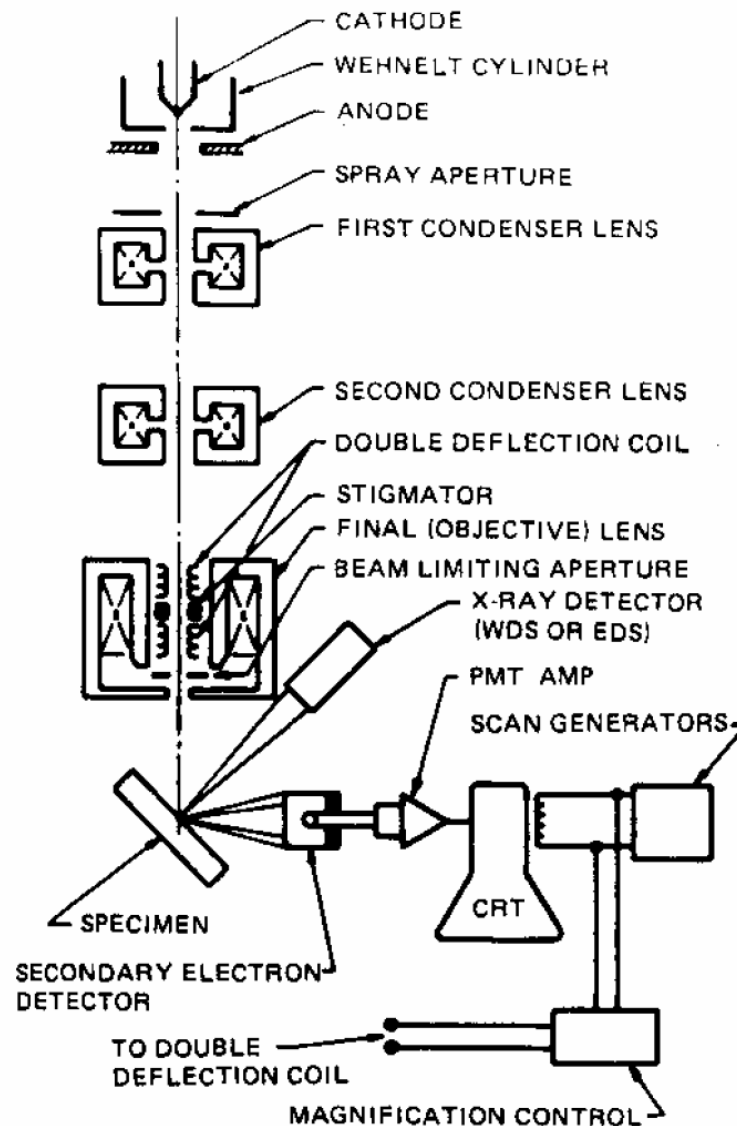


Fig. 10: Schematic of the scanning electron microscope [22]

Through continuous random scattering events the primary beam effectively spreads and fills a teardrop-shaped interaction volume (Fig. 11) with a multitude of electron interactions. The result is a distribution of electrons which manage to leave the specimen with an energy spectrum shown at Fig. 11. In addition, target X-rays are emitted and other signals such as light, heat, and specimen current are produced; the sources of their origin can be imaged with appropriate detectors. Various SEM techniques are differentiated on the basis of what is subsequently detected and imaged. [22]

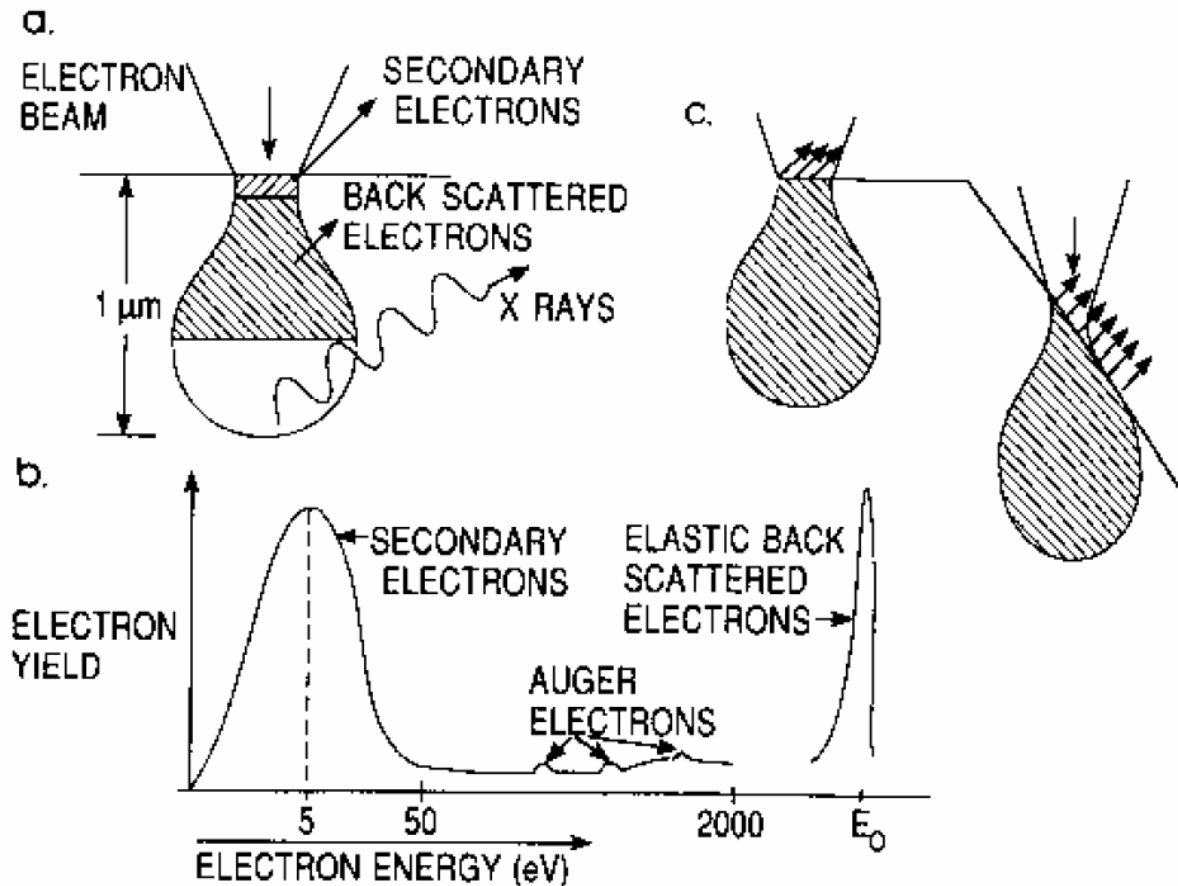


Fig. 11: a) Electron and photon signal emanating from tear-shaped interaction volume during electron-beam impingement on specimens surface, b) energy spectrum of electron emitted from specimen surface, c) effect of surface topography on electron emission [22]

### 2.5.3 Atomic force microscopy (AFM)

The Atomic Force Microscopy (AFM) is also known as the Scanning Force Microscopy (SFM). The AFM is the most widely used technique of Scanning Probe Microscopy (SPM) families because of its experimental flexibility and broad applicability. The AFM can produce very high resolution, 3D images of sample surfaces. The main working principle in AFM is the measurement of ultra small forces (less than 1 nN) present between an AFM tip and a sample surface. AFMs are capable of investigating the surfaces of both conductive and insulating sample at an atomic scale. On the base of construction, there are two different kind of AFMs are available commercially – (1) small sample AFMs and (2) large sample AFMs. In the case of small sample AFMs, during analysis of sample surface, the sample is generally scanned instead of the tip (i.e. tip is remains in stationary position and sample is moving

under the tip) because the AFM measures the relative displacement between the AFM tip surface and reference surface and any cantilever movement would add vibrations. Hence, it can produce very high-resolution surface images. While in the case of measurement of large samples, AFMs are available, where the tip is scanner (moving) and the sample is stationary. Because of vibrations added by tip movement, lateral resolutions are poor compare to the previous case.

The principle of operation of commercially small sample AFM is shown in Fig. 12. The sample is generally smaller than  $10\text{ mm} \times 10\text{ mm}$ . It is mounted on a piezoelectric tube (PZT) scanner, which controls the movement of sample in x-y plane in a raster pattern and to move the sample in z direction. A sharp tip at the free end of the cantilever is brought in contact with the sample. The features on the sample surface cause the tip and its cantilever to deflect vertical and lateral directions as the sample is scanned under the tip. A laser beam from a diode is focused on the backside of the cantilever at an angle of  $10^\circ$ . Hence, the reflected beam is captured by the photo diode. The photo diode is connected with the feedback systems. According to the twist and movement of tip cantilever captured by photodiode, the feedback system is used to modulate the voltage applied to the PZT scanner to adjust the height of PZT. [23], [24]

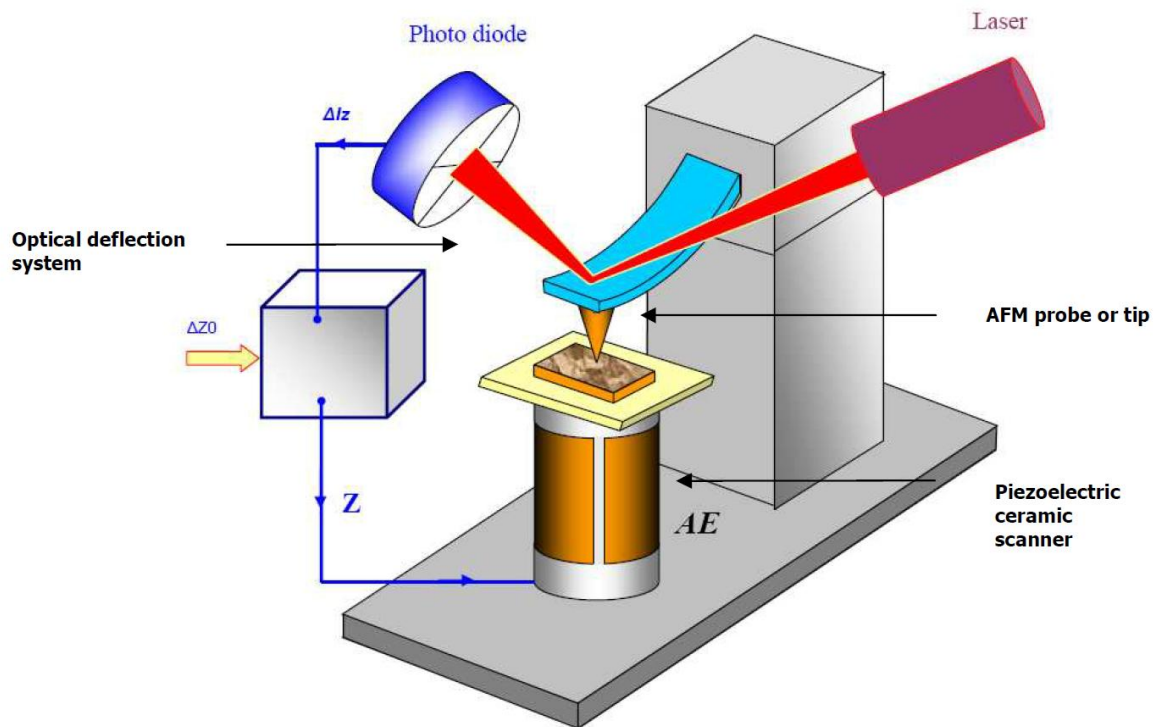


Fig. 12: Simplified scheme of the feedback in an optical lever detection AFM [23]

In the AFM microscope construction, there are three main parts:

- (a) AFM probe or tip,
- (b) Sample stage and piezoelectric ceramic scanner, and
- (c) Optical deflection system consisting of a laser diode and photo detector (or photo diode).

In AFMs, the images are generated by tip-sample interactions during the raster scanning of a sharp probe over a sample. A well-characterized tip is the key element in AFMs for good data interpretation and it is typically the limiting factor. Commercially available AFM probes are made from silicon and silicon nitride. They are microfabricated by lithographic and anisotropic etching techniques. The qualities of newly produced AFM probes can be characterized by imaging the nanometer scale standard materials of known geometry and dimensions. For AFM tips, the scan image resolution roughly corresponds to the radius of curvature of the tip, the tip aspect ratio and the sample height. The schematic image of AFM probe and its electron microscope image is mentioned in Fig. 13. [23]



Fig. 13: a) Schematic image of AFM probe, b) SEM image of AFM probe [23]

A high-resolution surface image is obtained by SPM method, by monitoring the tip-sample distance with high accuracy (at a level of Angstrom fractions). The position between tip-sample distances is monitored by scanners. The scanning elements of probe microscopy are made of piezoelectric materials – the materials having piezoelectric properties (i.e. materials change their sizes in external electric field). The scanner moves the sample relative to the cantilever in three dimensions. There are many different kinds of scanner designs available. In which, the piezo tripod is one way to achieve three-dimensional movement of a tip attached to its centre. However, the tripod needs large area (~50 mm) for its construction. Hence, its large size and asymmetric shape makes it susceptible to thermal drift error. The scanners made based on one tubular element are most widely used in the scanning probe microscopy. These scanner probes ample scanning range with small size. Control electronics systems for AFMs can use either analog or digital feedback. It is suitable for ultra low noise operation. The general view of a tubular scanner and arrangement of electrodes are presented on Fig. 14.

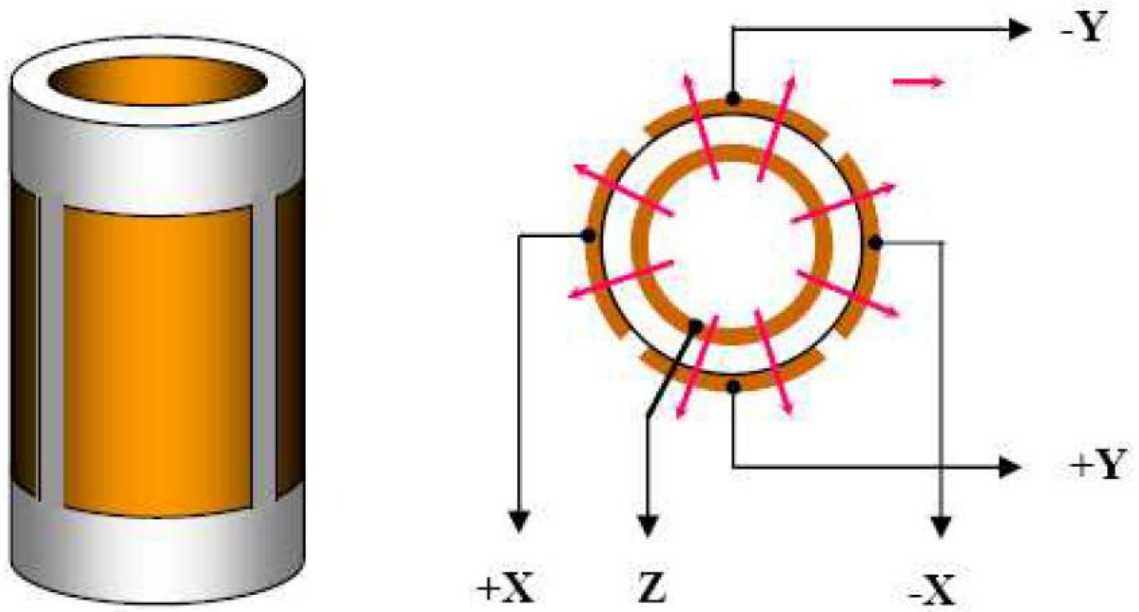


Fig. 14: Tubular piezo-scanner [23]

The key component in AFM design is the sensor for measuring the tip movement because of the tip – sample interactions. The force on the tip due to its interaction is sensed by detecting the deflection of the compliant lever with a known spring constant. There are number methods used to measure the cantilever deflection. Compare to other methods, the optical techniques are believed to be more sensitive, reliable and easily implemented than others. The optical beam deflection method (Fig. 15) has the largest working distance and capable of measuring angular changes (because of friction forces). Hence, it is the most commonly used in the commercial AFMs (i.e. SPMs).

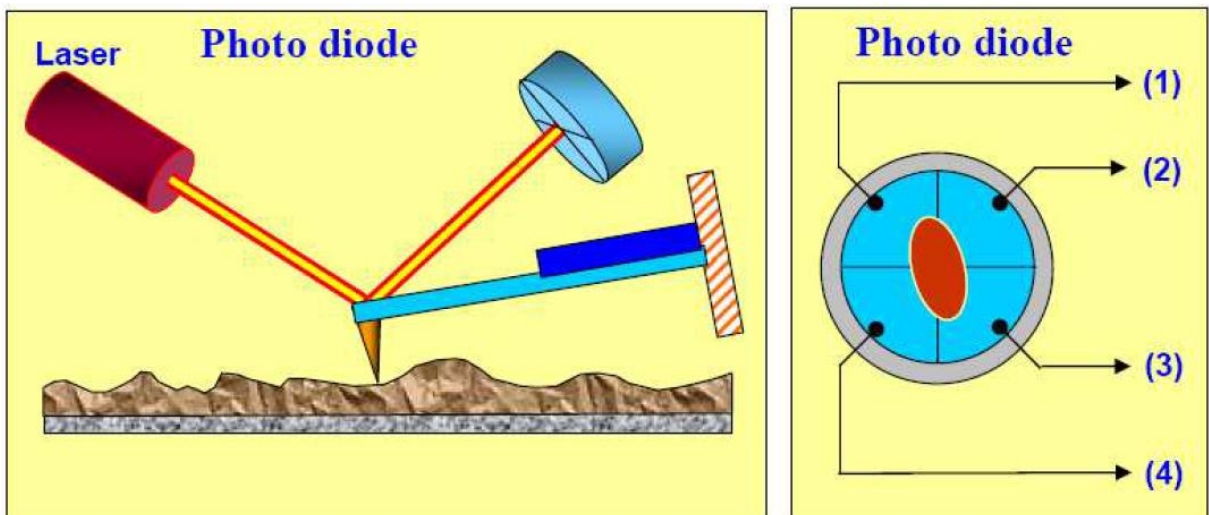


Fig. 15: Schematic description of the optical system to detect the cantilever bending [23]

The schematic diagram of optical system used to measure a probe deflection is described in Fig. 16. The laser diode stage is a tilt stage used to adjust the position of a laser beam on the backside of the cantilever. It consists of the laser diode, collimator, focusing lens, photodiode. The laser beam is reflected off the backside of the cantilever. A four quadrant photodetector gives the opportunity to measure both normal bending (1-2) and torsion (2-3) of the cantilever, corresponding to normal and lateral forces. [23]

The AFM can be used either in static or dynamic mode. In the static mode, also referred to repulsive mode or contact mode, the tip at the free end of the cantilever is brought in contact with the sample surface. During initial contact, the atoms at the end of tips experience a very weak repulsive force due to the electronic orbital overlap with the atoms of the sample surface, as mentioned in Fig. 16. The force acting on the tip causes the cantilever deflection, which is detected by the optical deflection system. The up and down motion of the sample is therefore a record of the sample topography. The dragging motion of the tip, however, combined with adhesive and lateral forces, can cause substantial damage to both the tip and sample. [23]

To alleviate this problem, the dynamic mode operation of the AFM, also referred as tapping or intermittent contact mode. In this mode, the cantilever is oscillating at or near its resonant frequency using a piezoelectric actuator. The oscillation amplitude of the cantilever in air can be greater than 20 nm when tip is out of the contact of the sample. When tip is approaching the sample, and when it begins to lightly touch or tap the sample surface. The oscillation amplitude of the tips is reduced. This reduction in oscillation amplitude is now becomes the feedback control signal which can be used to produce the surface topography. Here, the oscillating amplitude is kept large enough so that the tip does not stick to the sample. The mode is used in topography measurements to minimize effect of friction and other lateral forces to measure the topography of soft surfaces. [23]

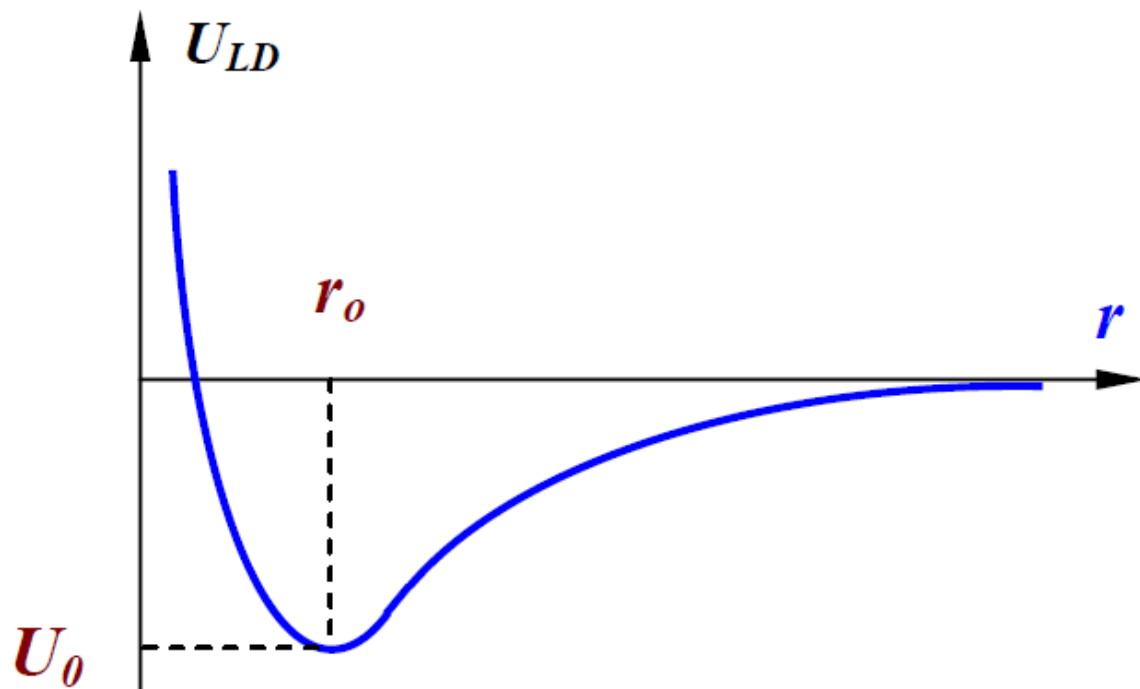


Fig. 16: Lennard-Jones potential qualitative form [23]

#### 2.5.4 Nanoindentation (NI)

In such developments, a good understanding of the surface analysis and mechanical properties of thin films is essential. It is, however, not a simple undertaking to evaluate the mechanical properties of a thin structure unit at submicron level using conventional testing methods. However, recent years, several techniques have been developed to study the nanomechanical properties of thin films. Among these, nanoindentation is a widely used technique for evaluating nanomechanical properties such as elastic modulus, hardness, and stiffness. Although nanoindentation is an excellent tool, good interpretation of the indentation data is important in order to achieve reliable and repeatable results regarding the mechanical behaviour of the thin films.

The goal of majority nanoindentation tests is to extract elastic modulus and hardness of the specimen material from load-displacement measurements. The idea of nanoindentation test came from the traditional indentation test (macro or micro indentation), which is an excellent way to measure mechanical properties of thick coatings. The traditional indentation test involves the measurement of the size of a residual plastic impression in the specimen as a function of the indentation load, which provides a measure of the contact area for that particular indenter load.

The same concept is applied for the nanoindentation test but the problem is determining the indentation contact area, which is very small. It can be difficult to see without a powerful microscope. To solve this problem depth sensing indentation methods were developed. In this method, the load and displacement of the indenter is recorded during the indentation process and these data are analyzed to obtain the contact area, and thereby mechanical properties, without having to see the indentations.

In simple word, nanoindentation refers to a depth-sensing testing in the submicrometer range. It has been made possible by the development of (1) machines that can make such tiny indentations while recording load and displacement with very high accuracy and precision, and (2) analysis models by which the load displacement data can be interpreted to obtain hardness, modulus, and other mechanical properties. [25]

To run a successful nanoindentation test, a well-defined geometrical indenter tip is very important. There are numerous geometries available for the nano indenter such as three sided pyramids, four sided pyramids, wedges, cones, cylinders or spheres. The tip end of the indenter can be made sharp or flat or rounded to a cylindrical or spherical shape.

The nano indenter is mostly made up from diamond and sapphire materials. In some cases, other hard materials can also be used to make a nanoindenter such as quartz, silicone, tungsten, steel, tungsten carbide and almost any other hard metal or ceramic. Some widely used nano indenters are known as Berkovich, cube corner, Vickers, conospherical, knoop etc. Nano indenters are mounted on holders, which could be the standard design from a manufacturer of nano indenting equipment, or a custom design. The holder material can be steel, titanium, ceramic or other suitable material.

The Berkovich tip is the standard nanoindentation tip, which is widely used for the nanoindentation experiments of thin films. The geometry of a Berkovich tip can be described as a three-sided pyramidal tip with a total included angle of 142.35 degrees and a half-angle of 65.35 degrees mentioned in Fig. 17. The standard Berkovich tip is available with radius of curvature of 150 nm while the sharper ones are with a radius of curvature of 50 nm. Such pyramidal tips are commonly used in nanoindentation of ceramics, glass, metals, hard polymers, hard and smoothed biomaterial and thin films. [25]

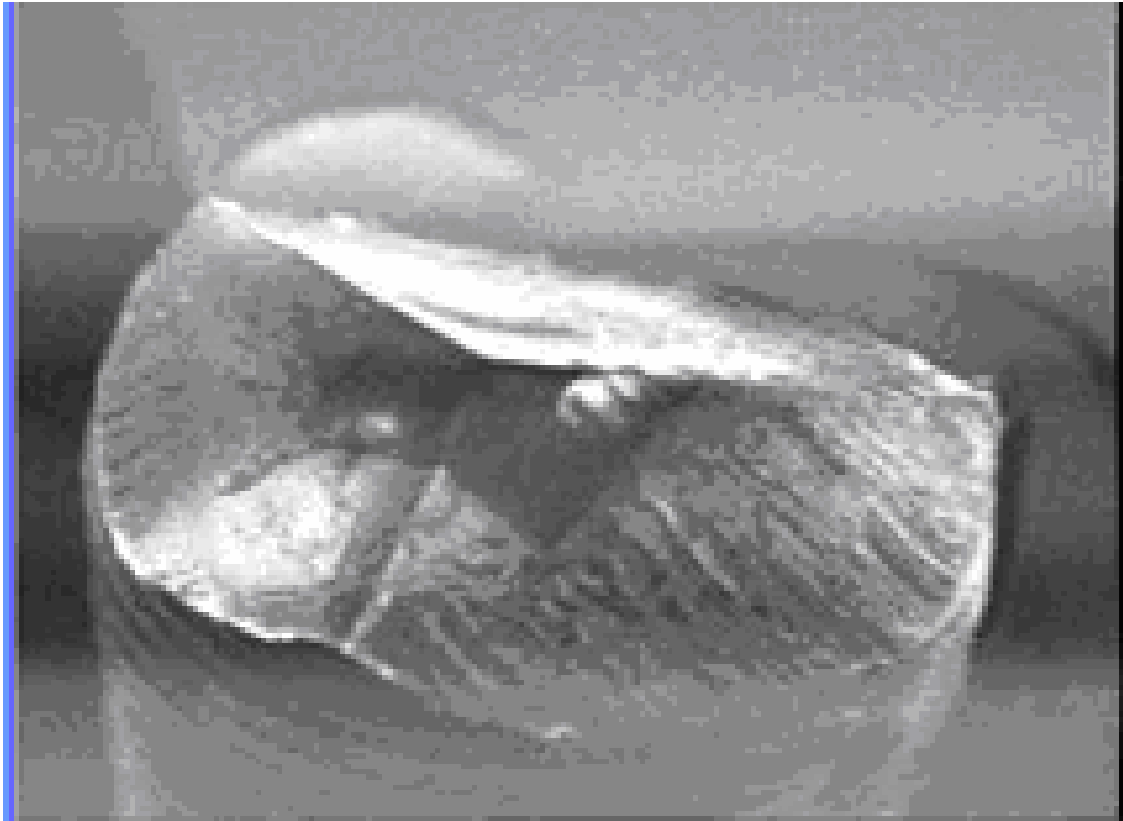


*Fig. 17: Optical microscopy image of Berkovich diamond probe [26]*

### **2.5.5 Further methods for thin-film testing**

Scientific disciplines are identified and differentiated by the experimental equipment and measurement techniques they employ. The same is true of thin-film science and technology. For the first half of this century interest in thin film centered on optical applications. The role played by films was largely a utilitarian one necessitating measurement of film thickness and optical properties. At first single films on thick substrates were involved. However, with the explosive growth of thin-film utilization in microelectronics there was an important need to understand to intrinsic nature of films in more complex materials environment. Increasingly, the benefits of multilayer film structures have been realized in an assortment of high-technology applications. Examples include multilayer metal and insulating films in microelectronics, compound semiconductor films in optoelectronics, dielectric-film stacks for optical coatings, and ceramic film layers in hard coatings.

With the increasingly interdisciplinary nature of applications, new demands for film characterization and property measurements in both individual films and multilayer coatings have arisen. It was this necessity that drove the creativity and inventiveness that culminated in the development of an impressive array of commercial analytical instruments. These are now ubiquitous in the thin-film, coating, and broader scientific communities. In many instances it was a question of borrowing and adapting existing techniques employed in the study of bulk materials (e.g. X-ray diffraction, microscopy, mechanical testing) to meet the challenges posed by thin-film applications. In other cases well-known physical phenomena (e.g. electron spectroscopy, nuclear scattering, mass spectroscopy) were exploited.

A partial list of the modern techniques employed in the characterization of thin-film materials and devices appears in Table 3. Among their characteristics are the unprecedented structural resolution and chemical analysis capabilities over both small lateral and depth dimensions. Some techniques only sense and provide information on the first few atom layers of the surface. Others probe more deeply but in most cases depth of a micron or less are analyzed. Virtually all of these techniques require a high or ultra-high vacuum ambient. Some are non-destructive while others are not. All of them utilize incident electron, or ion, or photon beams. These interact with the surface and excite it in such a way that some combination of secondary beams of electrons, ions, or photons are emitted, carrying off valuable structural and chemical information in the process. [22]

Table 3: Analytical techniques employed in thin-film science and technology [22]

Primary Beam	Energy range	Secondary signal	Acronym	Technique	Application
Electron	20–200 eV	Electron	LEED	Low-energy electron diffraction	Surface structure
	0,3–30 keV	Electron	SEM	Scanning electron microscopy	Surface morphology
	1–3 keV 500 eV–10 keV	X-ray	EPM (EDX)	Electron microprobe	Surface region composition
		Electron	AES	Auger electron spectroscopy	Surface layer composition
	100–400 keV	Electron	TEM	Transmission electron microscopy	High-resolution structure
	100–400 keV	Electron, X-ray	STEM	Scanning TEM	Imaging, X-ray analysis
	100–400 keV	Electron	EELS	Electron energy loss spectroscopy	Local small-area composition
Ion	0,5–2,0 keV	Ion	ISS	Ion-scattering spectroscopy	Surface composition
	1–15 keV	Ion	SIMS	Secondary ion mass spectrometry	Trace composition vs. depth
	1–15 eV	Atom	SNMS	Secondary neutral mass spectrometry	Trace composition vs. depth
	1keV and up	X-ray	PIXE	Particle-induced X-ray emission	Trace composition
	5–20 keV	Electron	SIM	Scanning ion microscopy	Surface characterization
Photon	>1 MeV	Ion	RBS	Rutherford backscattering	Composition vs. depth
	>1 keV	X-ray	XRF	X-ray fluorescence	Composition (1 mm depth)
	>1 keV	X-ray	XRD	X-ray diffraction	Crystal structure
	>1 keV	Electron	ESCA, XPS	X-ray photoelectron spectroscopy	Surface composition
	Laser	Ion	–	Laser microprobe Laser emission	Composition of irradiated area
Laser	Light	LEM	microprobe	Trace element analysis	

### 3 AIMS

In this thesis should be achieved:

- preparation of the sample surface by plasma etching
- SEM analysis
- AFM analysis
- nanoindentation

### 4 EXPERIMENTAL PART

Nanocomposite foil, PEI foil and graphite nanoplatelets were supplied by Michigan State University (MSU). Foil from pure PEI was transparent and nanocomposite foil was black due the nanoparticles. Thickness of the nanocomposite and pure PEI foil is 0.06 mm, it was measured by microscrew. Average of graphite nanoplatelets is in range 1–10  $\mu\text{m}$ .

#### 4.1 Sample preparation

Sample preparation included three steps:

- foil cutting to size  $(10 \times 10) \text{ mm}^2$
- adhesive bonding of the foil on the silicon substrate
- argon plasma etching

Piece of foil was supplied in envelope because outer influences like a dust or fingerprints can devalue surface of the foil. The samples were stored in LD-PE bags after cutting and bonding procedure.

Eight samples were prepared, four pure PEI samples and four xGnP/PEI composite samples. Prepared samples were etched by argon plasma using tubular plasmachemical equipment in laboratory of plasmachemistry at Brno University of Technology, Faculty of Chemistry. Etching times were chosen 0, 1, 3, and 10 hours, it means that two samples do not undergo to plasma etching (Table 4).

Table 4: Etching times of samples

Etching times [hours]	
pure PEI	xGnP/PEI
0	0
1	1
3	3
10	10

Argon gas was used as a working gas. Its properties are in Table 5.

Table 5: Properties of argon gas

Name	Argon
Formula	Ar
Purity	100,00 %
Molecular weight	$39,944 \text{ g}\cdot\text{mol}^{-1}$
Producer	Linde Gas

As mentioned, specimens were bonded on the Si wafer (Table 6), which is also used as substrate in plasma depositions.

Table 6: Silicon wafer

Name	Formula	Dimensions	Producer
Silicon	Si	(10×10×0.6) mm <sup>3</sup>	ON SEMICONDUCTOR CZECH REPUBLIC, s.r.o. (Roznov pod Radhostem)

Deposition system:

Helical (capacitive coupling) deposition system was used for plasma etching. Scheme and picture of device is shown on the Fig. 17 and 18. The plasma chamber is made up from Pyrex-glass tube, which is 400 mm long, and its inner diameter is 40 mm. The inductive coil wrapped around the outside of the Pyrex tube (plasma chamber) is connected to a radiofrequency (RF) generator, operating at a frequency of 13.56 MHz, through the matching network. The system is able to work with power up to 500 W. The system enables a thin film deposition on planar substrate, single filament and continuously rewound bundle of fibres. [26]

Pumping system

Due to the fact that the reactor operates with a technical vacuum in a few orders, different types of gauges with required measuring range were used. Pumping system is selected with regard to required working pressures and vacuum gauges were selected according to the measuring ranges. The basis of a pumping system is a rotary vacuum pump Leybold-Trivac D16B, which works in the pressure range from 101 kPa to 10<sup>-1</sup> Pa with a pumping speed 16 m<sup>3</sup> per hour and diffusion pump with pressure range from 10<sup>-1</sup> to 10<sup>-4</sup> Pa with a pumping speed 110 dm<sup>3</sup> per hour. Drawback of diffusion pump is oil content which could pollute vacuum and therefore liquid nitrogen is used for device cold. The producer of pumping system of plasma equipment is Lavat Chotutice. Device component for pressure measuring is vacuum gauge Pirani VPM 01 with measuring range from 10<sup>5</sup> to 10<sup>1</sup> Pa, vacuum gauge Penning VPG 01 with measuring range from 10<sup>-1</sup> to 10<sup>-6</sup> Pa and vacuum gauge Capacitron with measuring range from 133 to 10<sup>-2</sup> Pa. Pumping system consists cooling of diffusion pump by water and pneumatic valves.

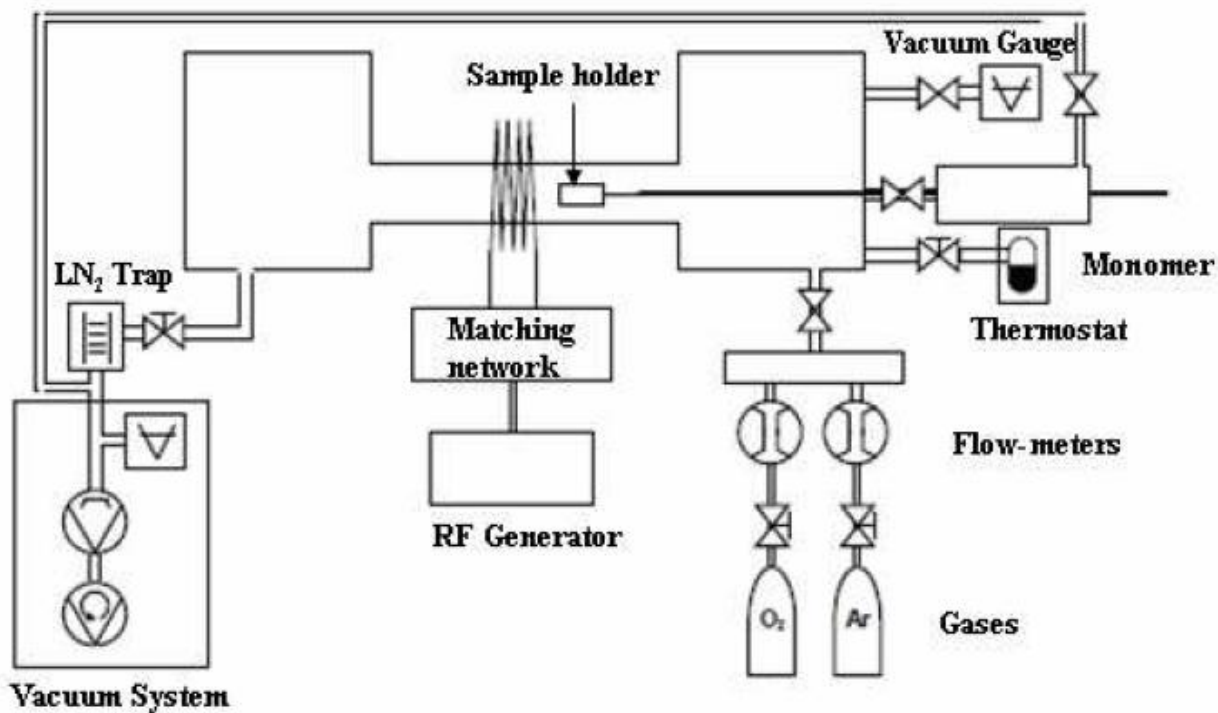


Fig. 17: Scheme of plasmachemical device

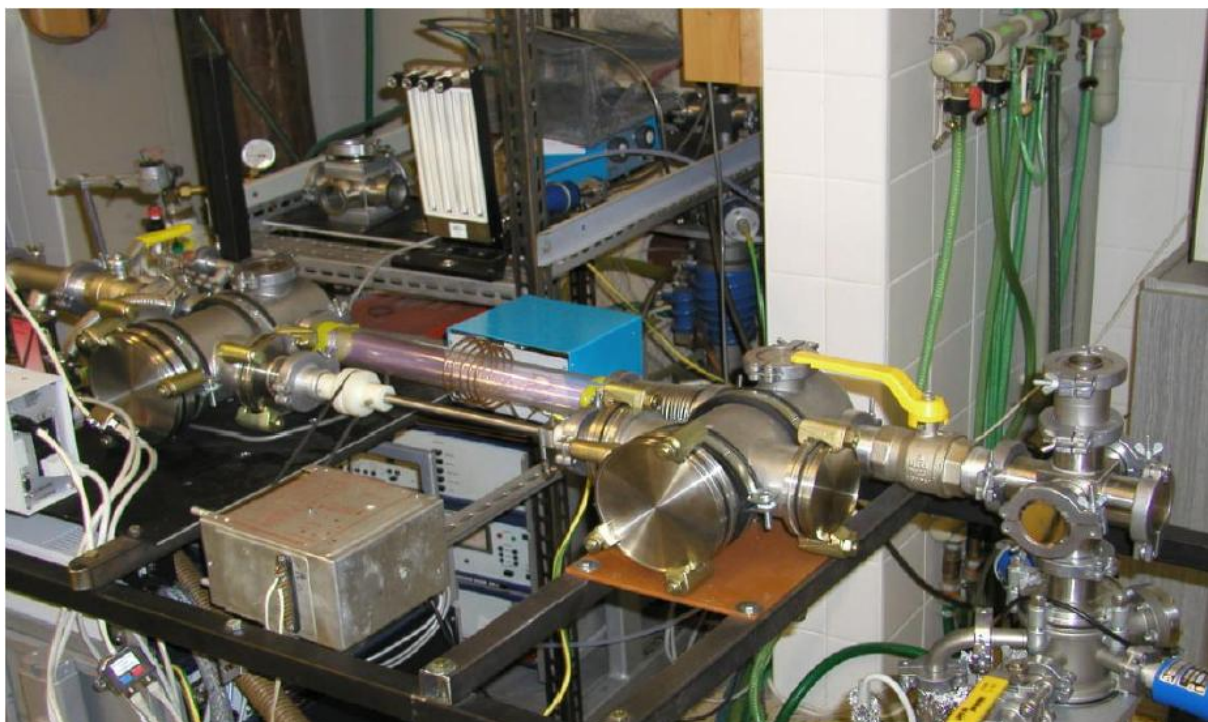


Fig. 18: Photo of plasmachemical device

Etching conditions were the same for all the samples, assumed in Table 7.

Table 7: Etching conditions for sample preparation

Etching time [hours]	1, 3, 10
Argon flow [sccm]	10
Pressure [Pa]	10
Mode	pulsed 1 : 1 <sup>1</sup>

<sup>1</sup> – Pulsed mode 1 : 1 means that 1 ms is discharge active and 1 ms not active

The general procedure steps for plasma etching by helical coupling system are mentioned below:

- I. Controlling of switched on buttons *pumping* and *high vacuum* on the device (diodes with 200 °C and B3 must be lit)
- II. Fill the diffusion pump by (liquid nitrogen) LN<sub>2</sub> half an hour before etching
- III. Closing of separation valve on the wave tube, further valves are opened, waiting for 30 minutes
- IV. Check the pressure on the Penning gauge, value should be about  $1-2 \times 10^{-3}$  Pa
- V. Calibration of Capatitron gauge to 0 Pa
- VI. Switch on PC and click on the Controller icon
- VII. Set up 10 sccm Ar on PC and 10 Pa on the strangulate valve, push the START button
- VIII. Moving of magnetic manipulator with specimen into the chamber
- IX. Tune the discharge with the coil and turn on countdown
- X. Filling the diffusion pump by LN<sub>2</sub> every 30–45 minutes
- XI. Switch off the discharge by STOP button after the etching time is reached
- XII. Opening of separation valve and let flow Ar in device next 1 hour
- XIII. After this time, turn off Ar intake and permit of strangulate valve

## 4.2 Optical microscopy

Optical microscopy was used only for composite xGnP/PEI, to image xGnP particles. This method was only approximate, if it is possible display nanoparticles. We were able to distinguish approximately size of the particles with using of scale.

Polarization optical microscope Olympus BX50 was used for imaging. This microscope is equipped with a heated stage Linkam LTS350 and digital camera Olympus Camedia 5060. Image of equipment is on Fig. 19.



*Fig. 19: Polarization optical microscope Olympus BX50 with heated stage Linkam LTS350*

### **4.3 Scanning electron microscope**

This method was used in two different cases. It is well known that samples analysed by SEM methods should be metallized. At the beginning of the analysis it was important to know something about sample surfaces before AFM analysis. Some prepared samples were analysed on the SEM. We were able to distinguish etched surfaces. These samples were not covered by metal layer. Some images exhibited white stripes across the width of scan and this is a consequence of sample charging. In the second case samples were coated by thin gold layer by magnetron sputtering. This process was performed after AFM and NI/NS analysis, because metallized samples were devalued for further analyses.

Analysis on Scanning Electron Microscope was performed in TESCAN, a.s. using a High Resolution Schottky MIRA3 Field Emission Scanning Electron Microscope (FE-SEM) XMU. This type of microscope can be classified to MIRA3 – Univac devices, models with adjustable pressure. [27]

Table 8 shows resolution of this type of microscope in the high-vacuum mode and low-vacuum mode for various values of voltage.

Table 8: Comparison of resolutions of FE SEM MIRA 3 XMU in various modes [27]

Voltage [kV]	High Vacuum Mode (SE) <sup>1</sup> [nm]	In Beam SE (option) [nm]	Low Vacuum Mode (LVSTD) <sup>2</sup> [nm]
30	1.2	1	1.5 - 2
15	1.5	1.2	-
3	2.5	2	-
1	4.5	3.5	3

<sup>1</sup> – SE – scattered electrons

<sup>2</sup> – LVSTD – low vacuum secondary electron TESCAN detector

Important properties of microscope are summarized in Table 9.

Table 9: Specific properties of FE SEM MIRA 3 XMU

Magnification at 30 kV	2× - 1000000× <sup>1</sup>
Accelerating Voltage	200 V to 30 kV
Electron Gun	High brightness Schottky emitter
Probe Current	2 pA to 100 nA

<sup>1</sup> – for 5" image in Continual Width Field / Resolution Mode

#### Vacuum system

Chamber vacuum could be divided into two types – the first is High vacuum mode, where is reachable pressure  $9 \cdot 10^{-3}$  Pa and second type is Low vacuum mode with reachable pressure in range from 7 to 150 Pa. Vacuum in electron gun is about  $3 \cdot 10^{-7}$  Pa. If the specimen is exchanged, time of pumping is approximately 3.5 minutes. Dimensions of chamber are 300 mm (width) × 330 mm (depth). Door dimensions are 280 mm (width) × 310 mm (depth).

#### Stage properties

Specimen stage is compucentric and fully motorized and its movements in X direction are 130 mm (-50 mm to +80 mm), Y = 130 mm (-65 mm to +65 mm) and Z = 100 mm. Stage could rotate in 360 ° continuously and can be tilted from -30 ° to +90 °. Maximum specimen height could be 145 mm without rotation stage.

#### Detectors

Standard:

SE – Secondary electron detector Everhart-Thornley type (Yttrium Aluminium Garnet YAG Crystal)

Retractable BSE<sup>1</sup> – Annular scintillator backscattered electron detector (YAG crystal), retractable type, with high sensitivity and atomic number resolution (0.1)

Touch Alarm – stops stage movements when sample touches any part of chamber

IR TV-camera – for the live chamber view

Options:

In-Beam detector – Detector of secondary electron located in the objective and intended for the highest resolution, especially at low voltages

LVSTD – Original SE detector for low vacuum operations, modified Everhart-Thornley type, U.S. Patent No. 7,193,222 B2

Retractable Dual Scintillator BSE Detector

Retractable 4-Quadrant Semiconductor BSE Detector

TE Detector – Transmission electron detector (STEM adaptor) allows Bright and Dark Field imaging modes

CL Detector<sup>1</sup> – Panchromatic cathodoluminescence detector, two available wavelengths ranges: 350–650 nm and 185–850 nm

EBIC – Electron beam induced current detection

EDX<sup>2</sup> – Energy Dispersive X-ray spectrometry; Take off angle 35 ° at WD 15 mm, 30 ° at WD 10 mm

WDX<sup>2,3</sup> – Wavelength Dispersive X-ray spectroscopy; Take off angle 35 ° at WD 15 mm, 30 ° at WD 10 mm

EBS<sup>2</sup> – Backscattered Electron Diffraction

<sup>1</sup> – motorized mechanics as an option

<sup>2</sup> – fully integrated third party products

<sup>3</sup> – configuration with In-Beam detector to be approved with TESCAN Brno

Arrangement of microscope and its equipment is imaged below on Fig. 20.

Table 10 shows installation and environmental requirements for using of microscope MIRA3 FE-SEM XMU. [27]

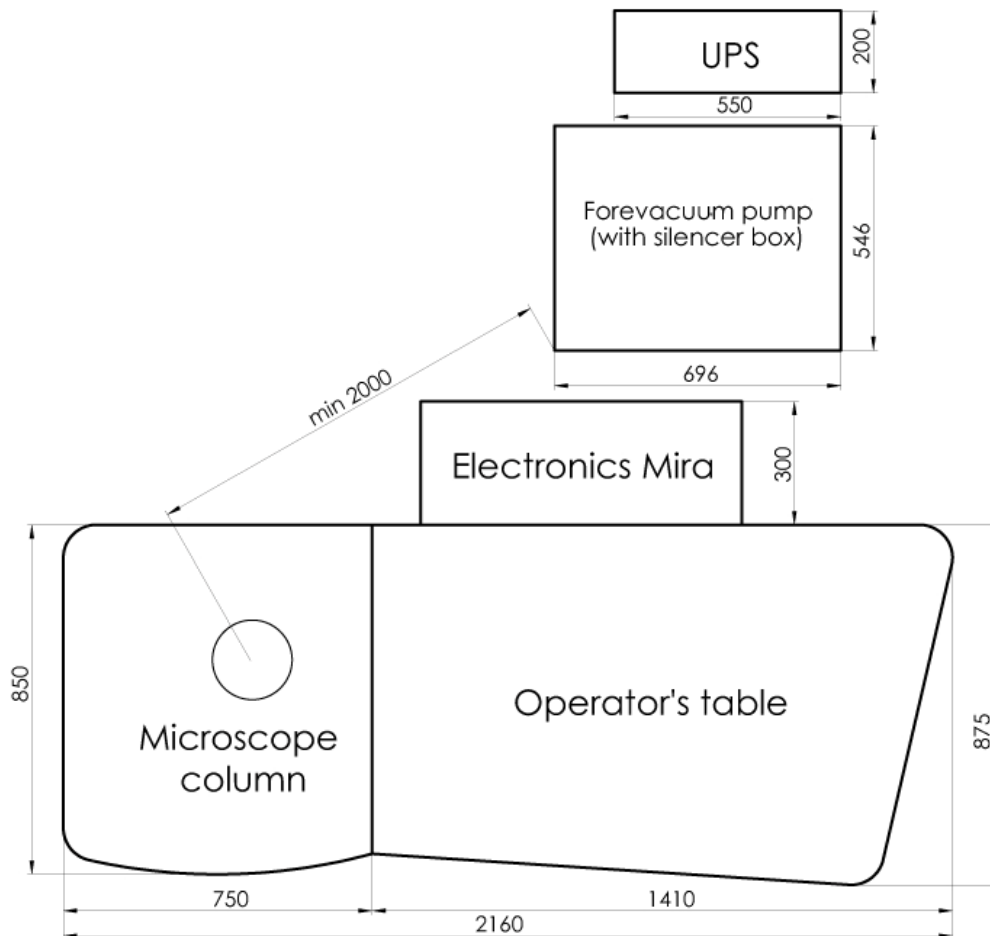


Fig. 20: Footprint of the Microscope (all dimensions are in mm) [27]

Table 10: Conditions for smooth function of microscope [27]

<b>Installation requirements</b>	
Power:	230 V $\pm$ 10 % / 50 Hz, 2200 VA, no water cooling
Dry nitrogen for venting:	150–500 kPa (1.5–5 Bars)
Compressed air:	450–600 kPa (4.5–6 Bars)
System dimension:	2.160 m $\times$ 1.185 m
Room for installation:	min. 3 m $\times$ 3 m, min. door width 0.90 m
<b>Environment requirement</b>	
Temperature of environment:	17–24 °C
Relative humidity:	max 80 %
Acoustic:	<60 dBC
Background magnetic field:	
- synchronous	<1 $\cdot$ 10 <sup>-7</sup> T
- asynchronous	<3 $\cdot$ 10 <sup>-7</sup> T
Vibrations:	
- passive isolation	<5 $\mu$ m/s below 30 Hz; <10 $\mu$ m/s above 30 Hz
- active isolation (option)	<10 $\mu$ m/s below 30 Hz; <20 $\mu$ m/s above 30 Hz

#### 4.4 Scanning Probe Microscope

Scanning probe microscopy experiments discussed in this Diploma thesis were done by a NT-MDT NTegra Prima scanning probe microscope with optical viewing system (Optical microscope). This part of the chapter introduces the basic design of NT-MDT scanning microscope, microscope head, scanner, specification of NTegra Prima instrument and SPM probe. Finally, the characterization steps and Nova software of NTegra Prima Scanning Probe Microscope is discussed.

##### 4.4.1 Scanning Probe Microscope basic setup

The NTegra Prima scanning probe microscope includes the following basic systems and set up:

- Base unit, which supports the completely scanning probe microscope operating system,
- Measuring module, which is made up of measuring head, exchangeable mount, scanner and heating stages, liquid cells etc.,
- Protective hood – to protect the scanning probe microscope from external vibrations
- Optical viewing system, and
- Vibration isolation system, which is manufactured by Table stable Ltd., Switzerland under brand name of TS–150. It is a vibration damping system, which is protecting the SPM system from vibration coming through ground.

The schematic illustration of basic modes of the NTegra Prima SPM is mentioned in Fig. 21 (a) and the NT-MDT SPM mentioned in Fig. 21 (b). By making changes in measuring modules, it is possible to operate different scanning probe microscopy methods such as Atomic Force Microscopy (AFM), Scanning Tunnelling Microscopy (STM), Lateral Force Microscopy (LFM), Atomic Force Acoustic Microscopy (AFAM), Magnetic Force

Microscopy (MFM), Electrical Force Microscopy (EFM), Kelvin Probe Microscopy (KPM), Lithography etc. The detail discussion about some of the main method is mentioned in the following part the chapter.

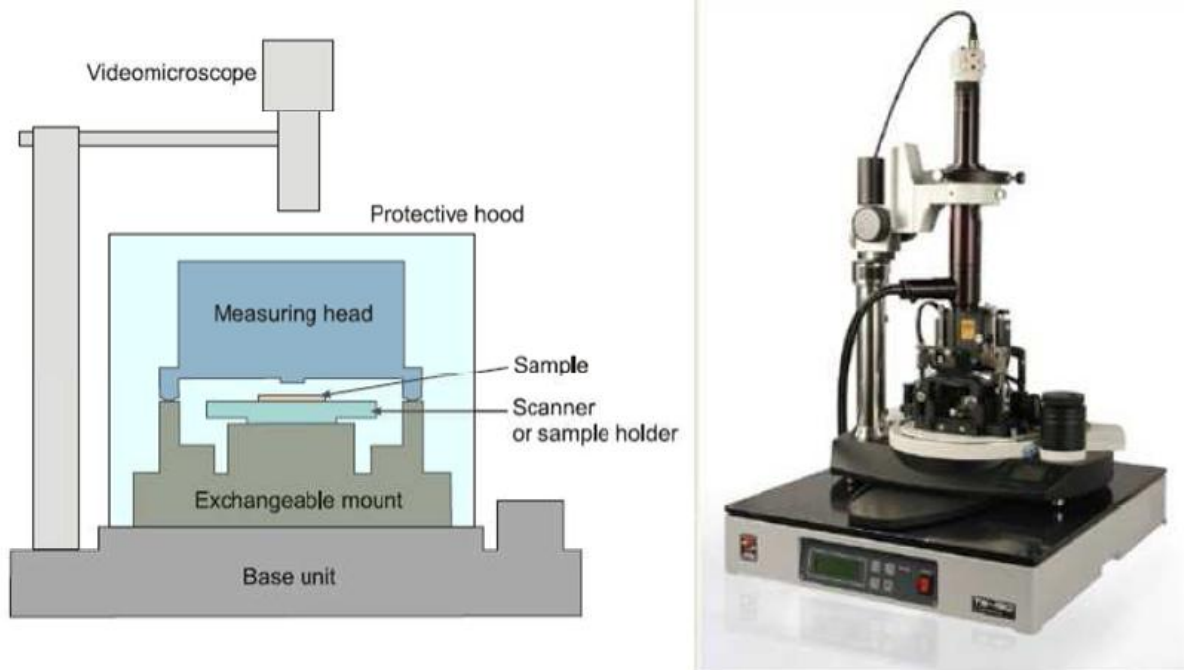


*Fig. 21: a) Schematic illustration of basic modes of NTegra Prima SPM, b) image of NTegra Prima SPM [28]*

### SPM measuring heads

There are three types of measuring head available with NTegra Prima system (a) Universal measuring head, (b) Scanning measuring head, (c) Scanning Tunnelling Microscopy (STM) head.

#### (a) Universal measuring head

The universal measuring head can be used to realize almost all SPM techniques both in air and in liquid. A broad range of measurement techniques is realized by using a set of adjustment units, which are specially designed for particular techniques and for measurements of certain parameters. An overview of the universal measuring head with the adjustment unit connected to it is presented in Fig. 22.

The universal measuring head is widely used in small sample AFM analysis. It consists of diode laser and lens, mirrored prism, mirror and a quad photodetector. (Split photodetector with four quadrants). By the help of adjustment screw, one can set the laser beam at the back side of the cantilever and also the reflected beam from the back side of cantilever strikes to the centre of the photodiode. The adjustment unit accommodates the probe holder.

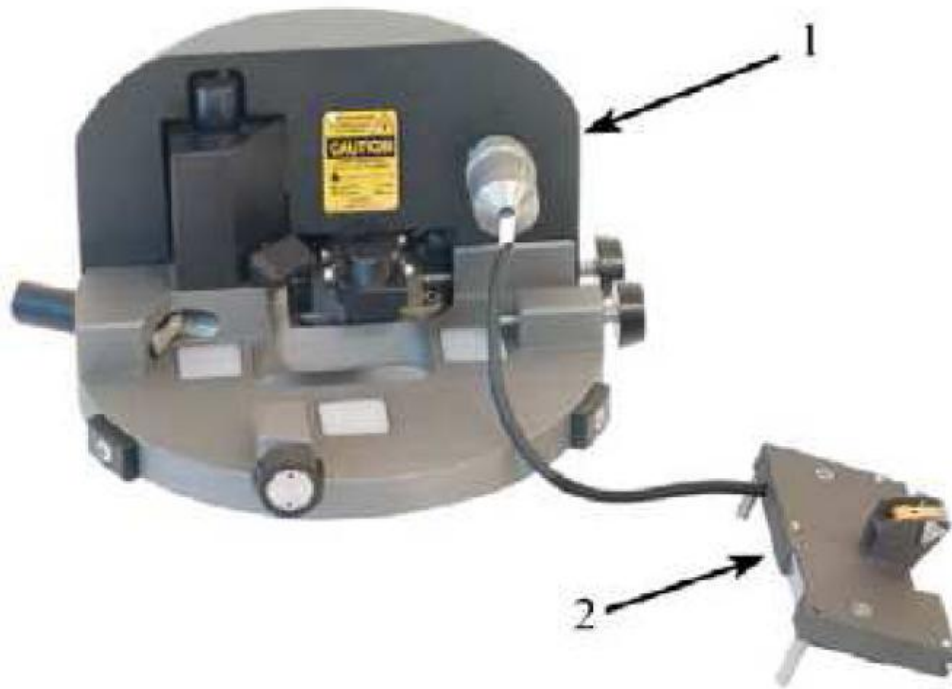


*Fig. 22: SPM measuring head: (1) Universal measuring head, (2) adjustment unit [28]*

(b) Scanning measuring head

It is also called as the large sample AFM head. It consists of both force sensors using optical deflection system (laser diode, mirrored prism, mirror and quad photodetector) and scanning unit. Because of the vibration added by cantilever movement, the lateral resolution of this design is somewhat poorer than the universal measuring head. It is also used for AFAM measurement, where sample is mounted on piezoelectric transducer.

(c) STM head

This head is specially used for Scanning Tunneling Microscopy (STM) measurement. The head consists of probe holder part which can hold sharpened part of a PtIr or W wire of 8–10 mm length and of 0.25–0.5 mm diameter. This wire is used as an STM probe. [28]

Scanners

The piezo-electric tube (PZT) scanner is widely used for SPM method. It consists of separated electrodes to scan precisely the sample in the  $x - y$  plane in a raster pattern and to move the sample in the vertical ( $z$ ) direction. There are two types of scanners available with NTEGRA Prima instrument.

- 1) Scanner without capacitance sensors. This scanner is connected to the base unit through the connected Scanner.
- 2) Scanner with capacitance sensors. This scanner is connected to the base unit through the connector Scan + Sensor.

A piezo ceramic tube, which is enclosed within a metal housing (Fig. 23), is the basic component of the exchangeable scanner. Carriage mentioned as 2 in Fig. 23 is fastened to the housing.

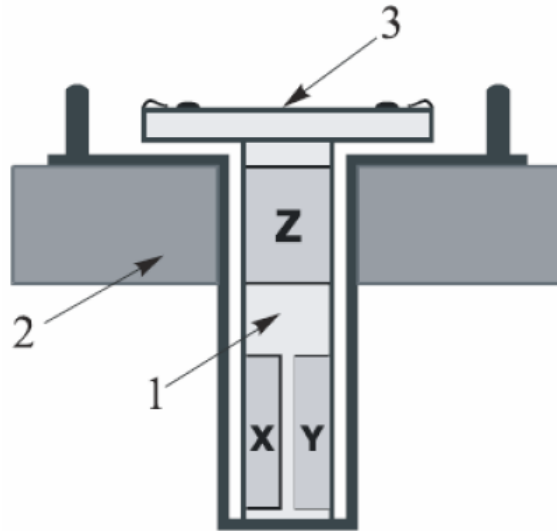


Fig. 23: PZT scanner design and arrangement for NTEGRA Prima SPM measurement:  
1) piezo ceramic tube for scanner, 2) carriage, 3) sample stage [28]

#### 4.4.2 NTEGRA Prima specification

The NTEGRA Prima SPM instrument is able to operate AFM (contact + semi-contact + noncontact), Lateral Force Microscopy (LFM), Phase imaging, force modulation, adhesion force imaging and lithography (AFM force) techniques in air and also in liquid medium. While, some other methods such as Scanning Tunnelling Microscopy STM, Magnetic Force Microscopy (MFM), Electrostatic Force Microscopy (EFM), Scanning Capacitance Microscopy (SCM), Kelvin Probe Microscopy (KPM), spreading resistance imaging, Atomic Force Acoustic Microscopy (AFAM), lithography (AFM current) are only possible to operate in air. The specification of NTEGRA Prima is mentioned in the following Table 11.

Table 11: NTEGRA Prima specifications

Specification	Scan type	Scanning by sample	Scanning by Probe
Sample Size		Up to the 40 mm in diameter, to 15 mm in height	Up to the 100 mm in diameter, to 15 mm in height
Sample weight		Up to 100 g	Up to 300 g
XY sample positioning range, resolution		5 × 5 mm, 5 μm	
Positioning sensitivity		2 μm	
Scan range		100 × 100 × 10 μm 3 × 3 × 2.6 μm less than 1 × 1 × 1 μm	100 × 100 × 10 μm 50 × 50 × 5 μm
Noise level, Z (RMS in band width 1000 Hz)	With sensors	0.04 nm (typically), ≤0.06 nm	0.06 nm (typically), ≤0.07 nm
	Without sensors	0.03 nm	0.05 nm
Noise level, XY (RMS in band width 200 Hz)	With sensors	0.2 nm (typically), ≤0.3 nm (XY 100 μm)	0.1 nm (typically), ≤0.2 nm (XY 50 μm)
	Without sensors	0.02 nm (XY 100 μm) nm (XY 3 μm)	0.01 nm (XY 50 μm)

### 4.4.3 SPM probes

In scanning probe microscopy analysis, the tip-sample interaction is the most important parameter to produce the images. For that purpose, a well-characterized tip is the key element in data interpretation. The schematic diagram of a rectangular cantilever is mentioned in Fig. 24. The probe has the form of an elastic girder called “cantilever” (mentioned as 2, in Fig. 24), which is fixed to the silicon base, called chip, of the probe. The probe tip which is in the form of a sharp pin is located on the free end of the cantilever.

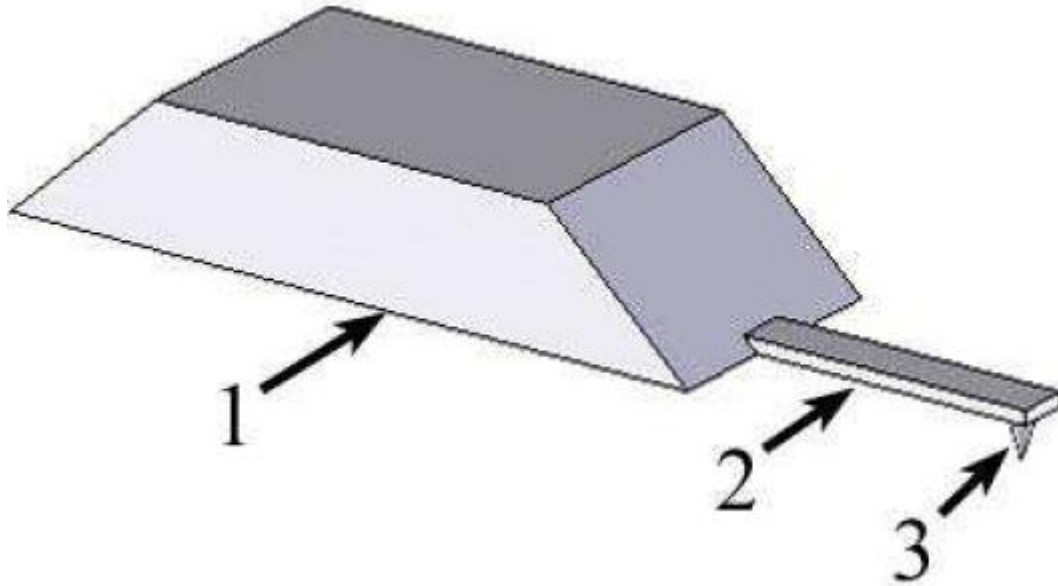


Fig. 24: Scheme of SPM probe: 1) chip, 2) cantilever, 3) probe tip [28]

The probes used for SPM analysis were supplied by NT-MDT company. The detailed description about the cantilever’s shape, size and their properties are mentioned in Table 12.

Table 12: Properties and applications of various types of SPM probes [28]

Cantilever	Properties					Applications
	Cantilever length, $L \pm 5 \mu\text{m}$	Cantilever width, $L \pm 5 \mu\text{m}$	Cantilever thickness, $L \pm 5 \mu\text{m}$	Resonant frequency, kHz	Force constant, N/m	
NSG10/Au	100	35	1.7 – 2.3	190 – 325	5.5 – 22.5	AFM (non-contact)
NSG10/W <sub>2</sub> C						SKM, SCM
NSG03/Au	100	35	0.9 – 1.5	62 – 123	0.4 – 2.7	AFM (non-contact)
NSG03/Co						MFM
CSG10/Au	250	35	0.7 – 1.3	14 – 28	0.03 – 0.2	AFM contact mode, LFM, AFAM
CSG10/Pt						SRI

Characteristics of NT-MDT probes are:

- have Au high reflectivity coating on backside of the cantilever (reflectivity property is increased by 3 times in comparison with uncoated cantilevers)
- tip side of the conductive chip NSG10/W<sub>2</sub>C series is coated by W<sub>2</sub>C (tungsten Carbide), CSG10/Pt is coated by Pt, thickness of W<sub>2</sub>C/Pt film is 20–30 nm;
- tip NSG03/Co series is coated by Co (Cobalt) for Magnetic force microscopy (MFM).
- high aspect ratio conical tips (cone angle is less than 22 °);
- typical curvature radius of the uncoated tip is 10 nm, of the coated tip is 35 nm

#### 4.4.4 AFM imaging modes

In this thesis three modes of scanning was used. Brief description of these modes is below.

##### Height Mode:

In this mode height map is recorded. Z axis represents the moving of the scanner in the vertical direction. Software settings allow colour differentiation. Acquired image has information about surface topography.

##### Semicontact Error Mode

When scanning in Semicontact mode, the value of the cantilever oscillation amplitude varies following the surface topography of the surface sample. The feedback loop tries to preserve the given level of the cantilever oscillation amplitude (Set Point) by maintaining the reference signal linked with the oscillation amplitude (in our case, this is the signal Mag). However the feedback loop cannot compensate for variations of the Mag signal instantaneously as it has some inertia (characterized by a time delay).

During scanning, the current value of the Mag signal (which is linked with the cantilever oscillation amplitude) is the error signal of the feedback loop and it contains additional information on surface topography. This signal can be used for a more detailed reproduction of topography. The mode that allows imaging of surface topography by the constant force mode simultaneously with measurements of the error signal (the Mag signal) is called Semicontact Error Mode.

The Semicontact Error Mode, similarly to the Contact Error Mode, can be considered as an intermediate mode between the Constant Force Mode and Constant Height Mode. This is possible providing that the speed of the error signal data processing (the feedback gain factor) is optimized so that feedback loop is able to trace smooth topography variations while not been able to recognize sharp features. Then, scanning of smooth surfaces with smooth and extended features is performed with a piezo-scanner of almost constant length. As a result, the final image will have higher contrast for smooth and large ones. This can be useful for identification of small features in the background of large and relatively smooth variations of the surface. [28]

##### Phase Imaging Mode

When scanning in the Phase Imaging mode, the tip of the oscillating probe periodically comes in touch with the sample surface. Its behaviour is affected by the influence of various repulsive, adhesive, capillary and other forces. This can affect both the oscillation amplitude

and phase. If the sample surface is inhomogeneous by its properties, this correspondingly results in some shift of the phase.

The phase shift distribution over the sample surface visualizes distributions of characteristics of sample substance.

The Phase Imaging Mode yields valuable information for a broad area of applications. In some cases it is uncover hidden contrasts in materials properties. This mode is employed, for example, in study of biological objects, samples with electrical and magnetic properties and a number of other areas. [28]

## **4.5 Nanoindentation techniques**

The nanoindentation experiment discussed in this thesis was carried out on Triboscope system from Hysitron, Minneapolis, USA. This instrument can be attached to any commercially available Scanning Probe Microscopy system to produce the qualitative depth-sensing nanoindentation experiment with in-situ imaging. This part of the chapter introduces the design of Hysitron Triboscope equipment, different nanoindentation methods and scratch testing. [29]

### **4.5.1 Introduction of Hysitron equipment**

We have the 2D Triboscope (Hysitron) system attached to an NTegra Prima Scanning Probe Microscope (NT-MDT, Russia). The displacement and load resolutions of the Triboscope (Hysitron) instrument are 0.0004 nm and <1 nN, respectively. While, the noise floor for displacement and load are 0.2 nm and 100 nN, respectively.

The detailed description about Hysitron Triboscope system is mentioned in diagram Fig. 25. The Triboscope nanoindenter is attached to NTegra Prima SPM via a cord, which could be seen in Fig. 25a. Complete system is placed on the vibration isolation system (Table Stable Ltd, Switzerland) which can act as vibration dumping system during the experiment and protects the instrument and experiment from error. The close up look of Triboscope head is mentioned in Fig. 25b, which is consists of a three-plate capacitive force/displacement transducer. It maintains the movement of tip. To protect the whole system and experiment from external acoustic noise, a protective hood as described in Fig. 25c covers the instrument.

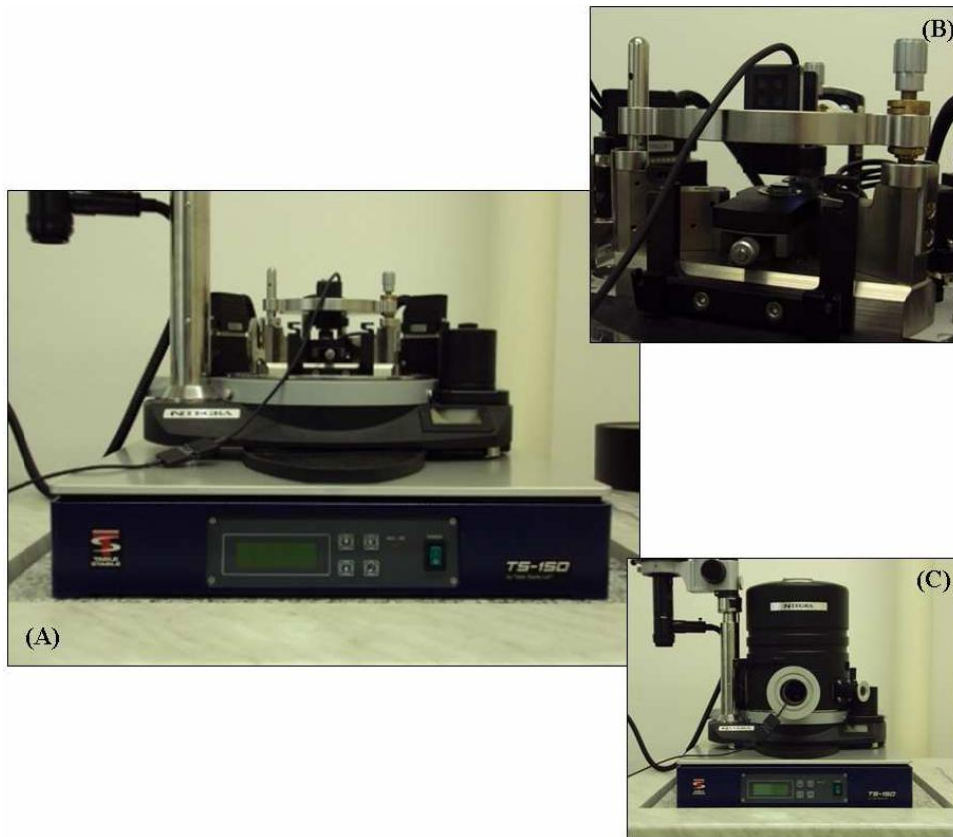


Fig. 25: Hysitron Triboscope system: A) Triboscope arrangement with NT-MDT SPM system, B) close up look of triboscope head, C) protective hood

Triboscope transducer

The three-plate capacitive force/displacement transducer could be referred as the heart of the testing instrument. It is a pattern technology from Hysitron Company, USA. This transducer provides high sensitivity, large dynamic range, and a linear force or displacement output signal. The schematic of Triboscope transducer is mentioned in Fig. 26. The centre plate of the transducer has a lower mass (200 mg) which facilitates to minimize the instrument's sensitivity to external vibrations and also allows light load (less than 25  $\mu\text{N}$ ) indentations to be made. [28]

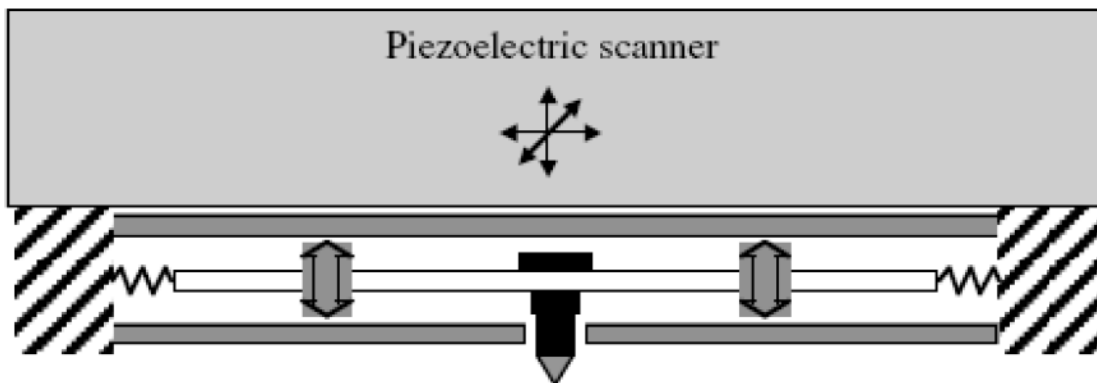


Fig. 26: Schematic diagram of Triboscope transducer

The sensor also consists of two fixed outer electrodes (drive plates). They are driven by AC signal 180 ° out of phase with each other. At any instance the signals applied to drive plates are equal in magnitude but with different polarity. The input impedance of the synchronous demodulator is larger than the output impedance, thus the pickup electrode will assume the same potential present at its position between the drive plates. A large DC charge is applied to the lower plate of the transducer, which thereby applies force to the tip. Varying the amount of charge will vary the applied force. According, to the Hysitron manual maximum load force available from a standard transducer is approximately 10 mN, while it would be increased to 30 mN with an optional extended force transducer.

#### Berkovich tip

Berkovich tip is a three-sided pyramidal tip with a total included angle of 142.35 ° and a half-angle of 65.35 °. Some details and an optical microscope image (Fig. 17) of it are mentioned in theoretical part chapter. In our nanoindentation study, the Berkovich tip with a radius of curvature 150 nm were used for the analysis of pure PEI or xGnP/PEI foil on silicon substrate. The Berkovich tip with known tip area function is important for correct indentation and scratch experiment. Hence, at proper interval of time, the tip area calibration is carried out.

#### Sample preparation

The sample preparation is necessary to be carried out with care. For nanoindentation and scratch test, special cyanoacrylate adhesive glue (Loctite 495) is used to stick the sample on steel ring sample holder or sapphire plate sample holder. In most of the cases, the steel ring sample holder is used because it is cheaper.

### **4.5.2 Nanoindentation measurements**

Two types of nanoindentation experiments were carried out with this instrument:

- (a) Conventional nanoindentation test,
- (b) Cyclic nanoindentation test.

The drift measurement is very important parameter in indentation test. The drift measurement is performed immediately before the testing. The displacement versus time of linear character was measured at 40 s (default) or 120 s (suggested) and the drift rate was evaluated using the linear regression for last 20 s (default) or 100 s (suggested), respectively. The drift rate was used to correct the acquired data from the real indentation testing. The drift rate was maintained in a range of 0.05 nm/s to 0.5 nm/s during indentation experiment.

#### Conventional nanoindentation

Conventional indentation test consist of three segments (1) loading, (2) dwell time or hold time and (3) unloading. Here, the loading segment is followed by a dwell time at maximum load, and followed by an unloading segment. The graphical presentation of conventional nanoindentation test is mentioned in Fig. 27.

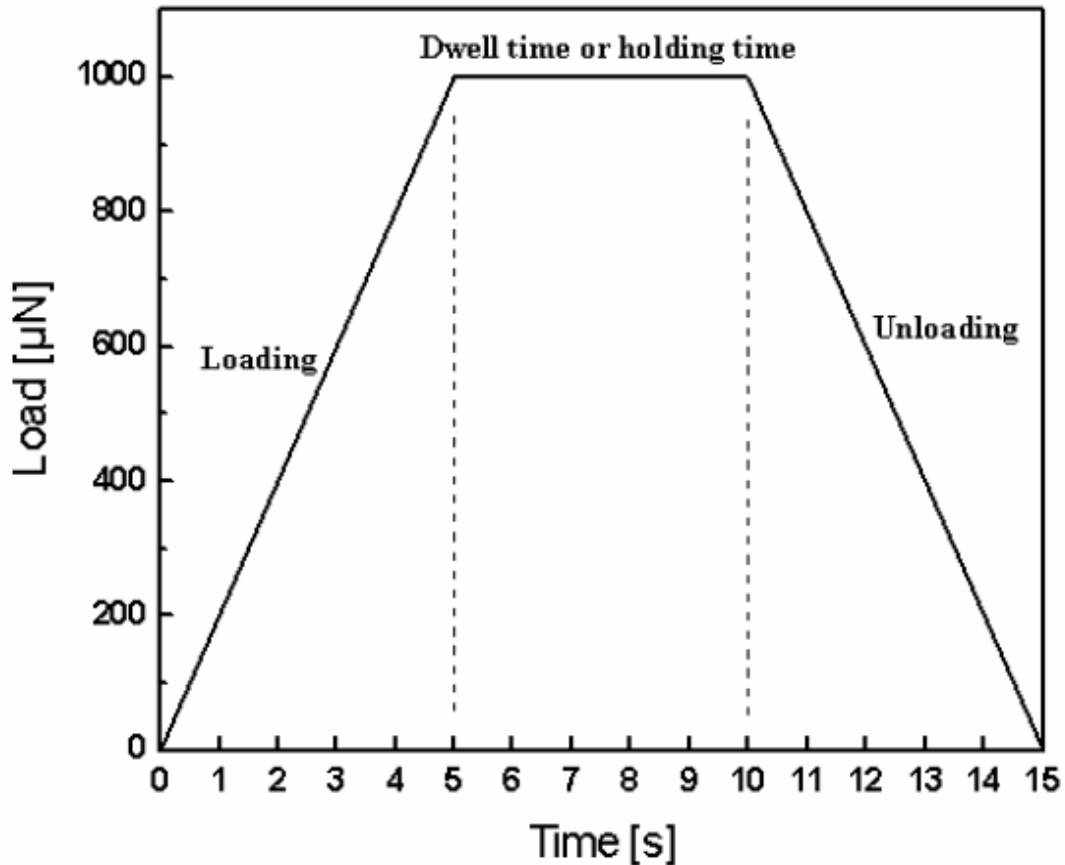


*Fig. 27: Graphical presentation of conventional nanoindentation test*

The main variable parameters for conventional test are the different loads ( $\mu\text{N}$ ) and measurement time (s) of experiment. One can change the load, from  $1 \mu\text{N}$  to  $10 \text{ mN}$  and also experiment time from minimum 3 sec to minutes. The load/unload vs. displacement curve (Fig. 28) is obtained by indentation experiment. In general, the loading causes both elastic and plastic deformation under the indenter, while unloading is dominated by recovery of elastic deformation. The upper portion of the unloading curve can be used to calculate the mechanical properties at a given contact depth of the indenter according to the Oliver-Pharr method. [25]

A conventional indentation experiment gives only a single value of mechanical properties at a particular load at a time. Hence, one needs to do many conventional indentation experiments at different loads to produce a depth profile of mechanical properties.

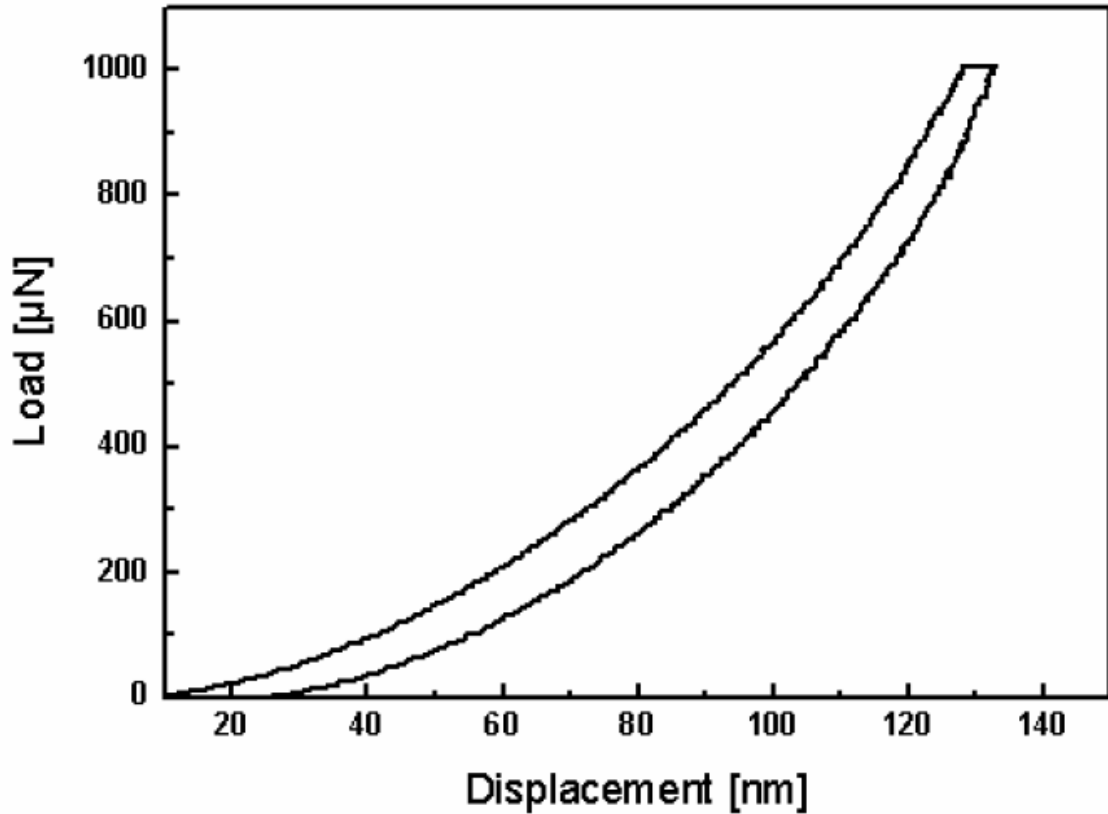
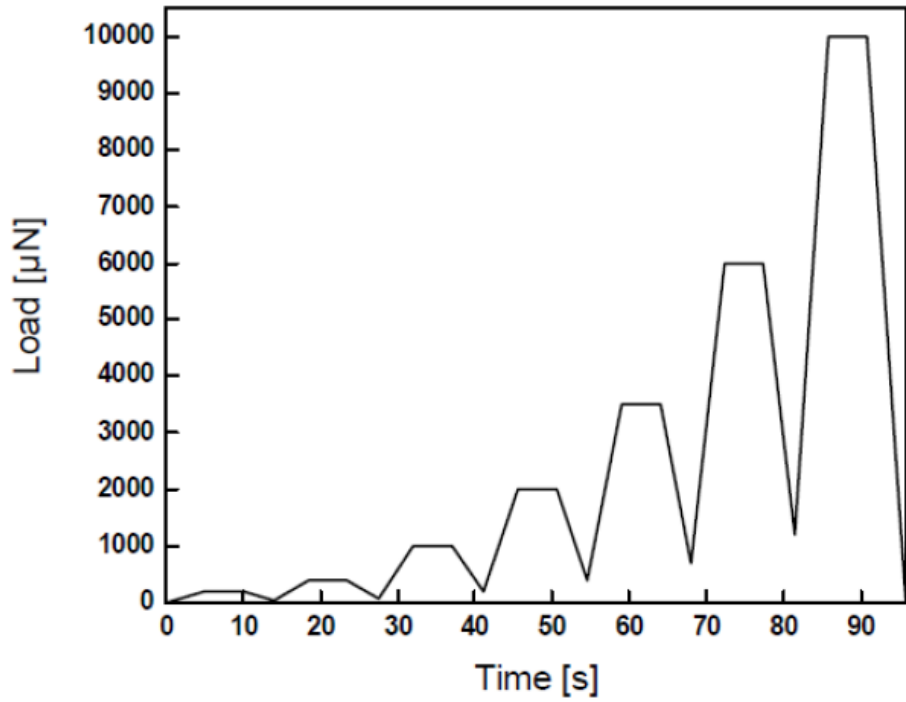


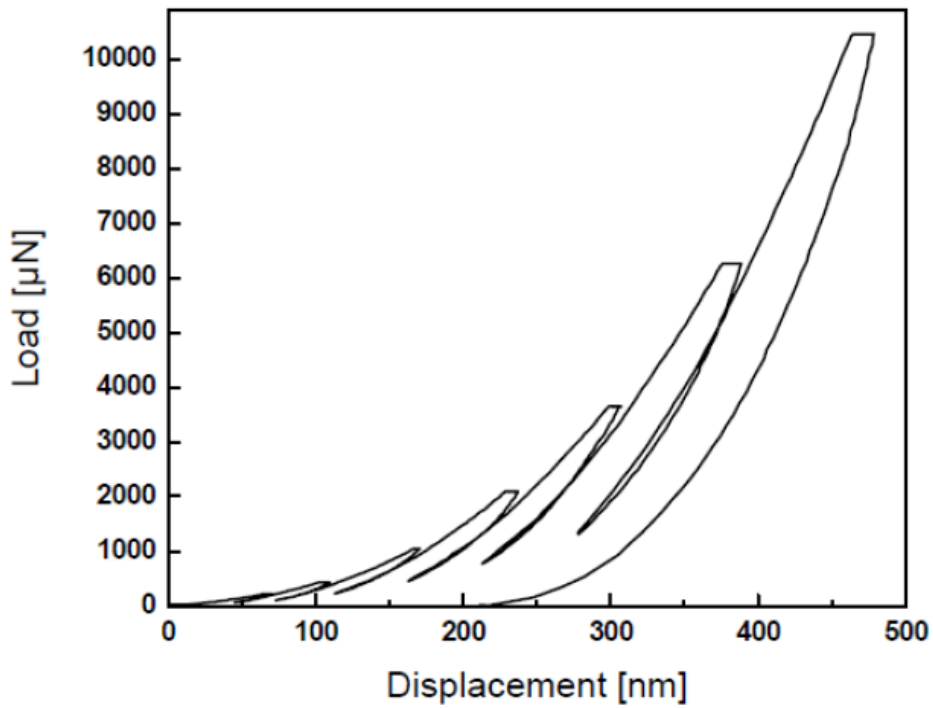
*Fig. 28: Load/unload vs. displacement curves obtained by conventional nanoindentation test*

For creep behaviour or strain sensitivity experiment, dwell time is the important parameter. The variation of dwell time from few second to minutes helps to study the creep behaviour or strain sensitivity of materials.

A new variation of the conventional test is the cyclic nanoindentation test, where the sample is reloaded immediately to higher loads/depths than previous loading cycle. The important variable parameters in cyclic test are number of cycles, maximum load, displacement exponent, unloading fraction and segments (loading/hold/unloading) time. The number of cycles can vary from 2 to 650. Here, the maximum load can change from 1  $\mu\text{N}$  to 10 mN. One can change the rest parameters like displacement exponent, unloading fraction and segments time to create the desired experiment conditions. Graphical presentation of seven cycle indentation is on Fig. 29 a, load/unload vs. displacement curves are mentioned on Fig. 29b.



(a)



(b)

Fig. 29: a) Graphical presentation of seven cycle indentation, b) Load/unload vs. displacement curve of cyclic nanoindentation

The Oliver-Pharr method is used in a similar way like conventional method to calculate the mechanical parameters from load/unload vs. displacement curve.

### 4.5.3 Nanoscratch test

The scratch test was used to study the adhesion between xGnP nanoplatelets and PEI. The conospherical tip with radius of curvature of 1  $\mu\text{m}$  was used for all the scratch testing. The proper tip area calibration was carried out before the experiment and obtained calibrated curve was used to correct the experimental data. The drift rate was measured immediately before every experiment like mentioned in indentation experiment and resulted drift rate (nm/s) was used to correct the experimental data. The X-axis and Z axis calibration was also carried out for Triboscope transducer calibration.

For scratch testing, the ramp force scratch positive direction experimental condition was used, as mentioned in Fig 30. The variable parameters in ramp force experiment are the peak force ( $\mu\text{N}$ ), time (s) of experiment, segment time (s), displacement ( $\mu\text{m}$ ) and lateral displacement ( $\mu\text{m}$ ). The Fig. 30 shows that the plots of normal force ( $\mu\text{N}$ ) vs. time (s) and x displacement ( $\mu\text{m}$ ) vs. time (s) are used for scratch test.

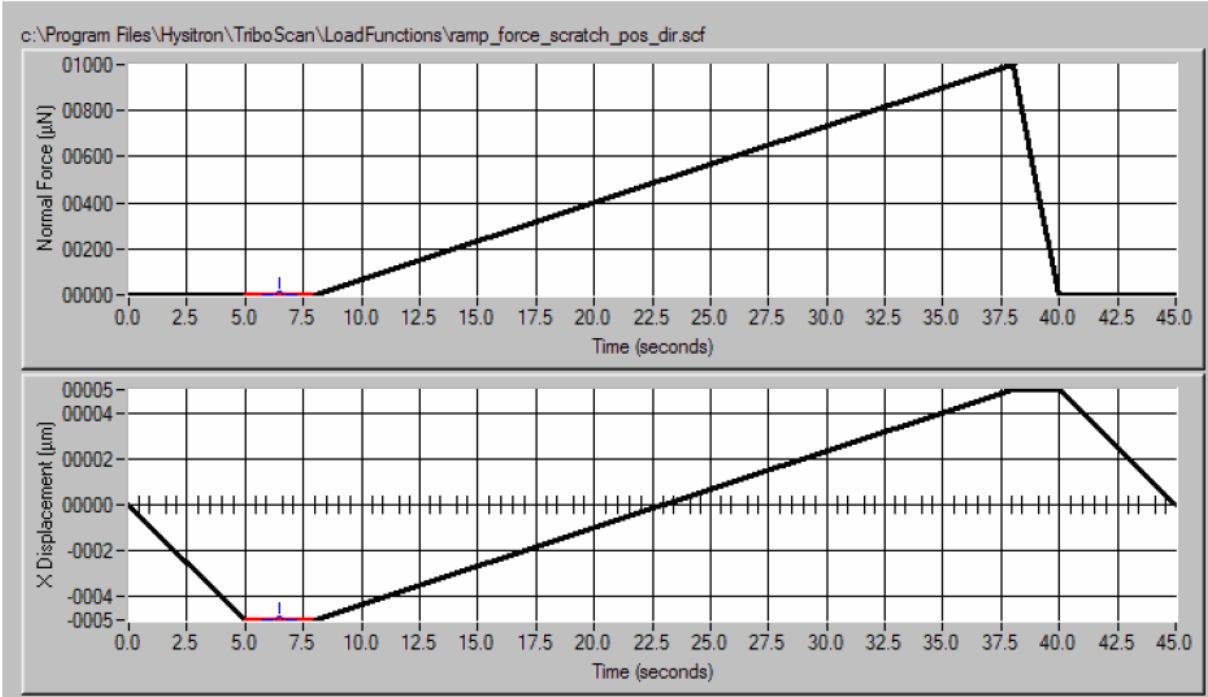


Fig. 30: Ramp Force scratch test in positive direction

The data obtained from scratch experiment was in terms of plots of normal force ( $\mu\text{N}$ ) vs. time (s), normal displacement (nm) vs. time (s), lateral force ( $\mu\text{N}$ ) vs. time (s) and lateral displacement ( $\mu\text{m}$ ) vs. time (s) as shown in Fig. 31. It gives information about the adhesion failure of thin films on substrate. The friction coefficient information was available from friction coefficient vs. time plot.

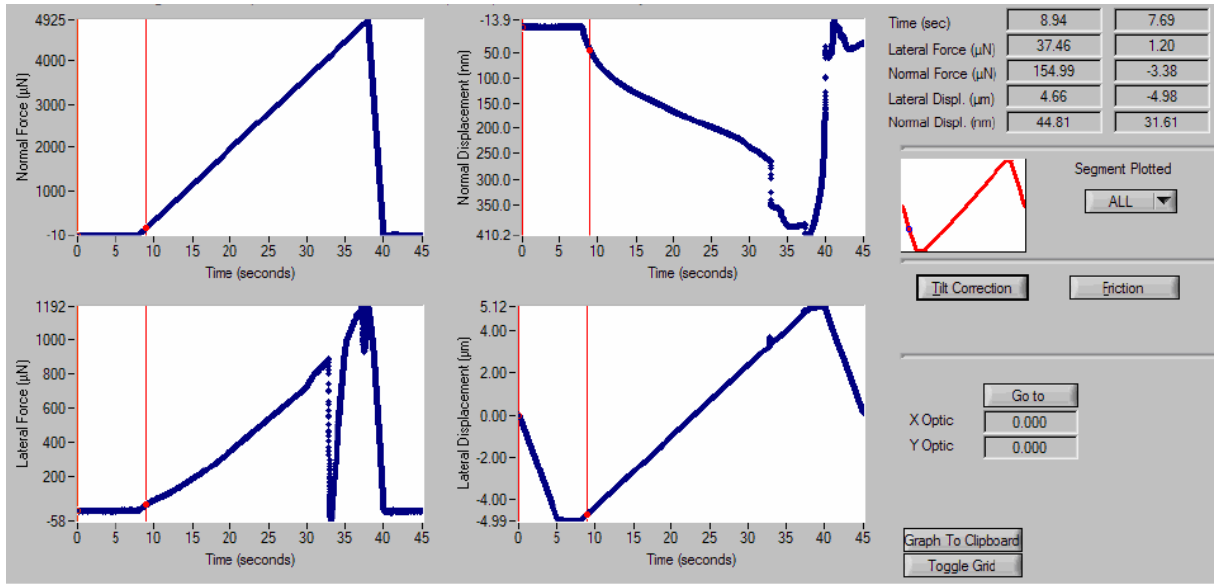


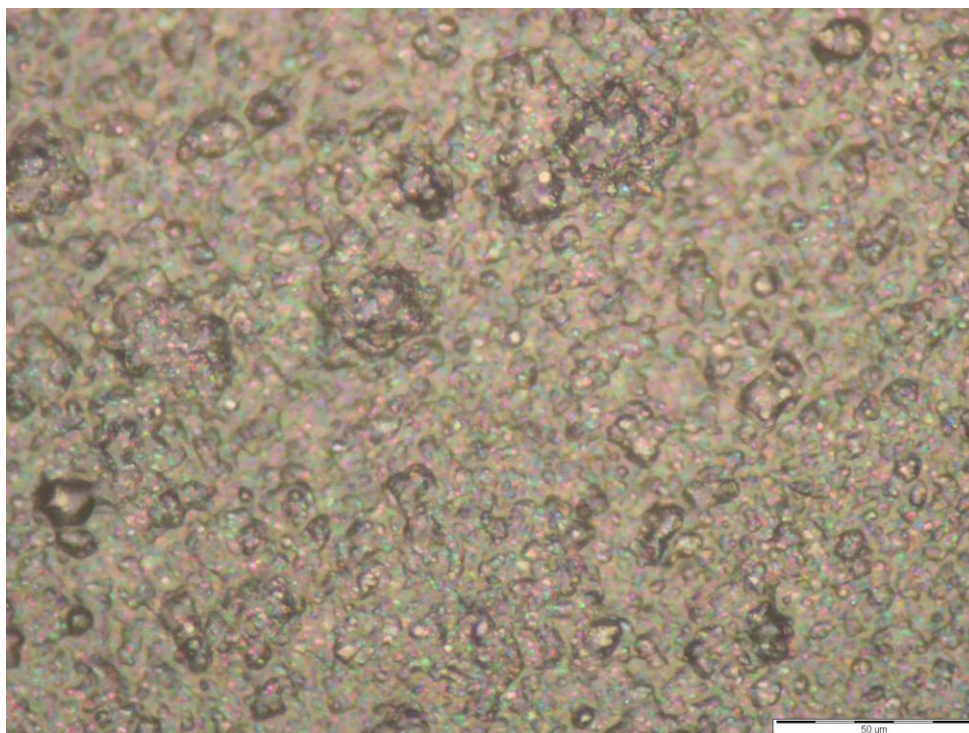
Fig. 31: Analysis data of scratch test

## 5 RESULTS AND DISCUSSION

### 5.1 Plasma etching and optical microscopy

Influence of etching time of argon plasma on the morphology of nanocomposite foil will be discussed in this chapter. Times of etching were suggested on a basis of background research and previous experience with argon and oxygen plasma used for polymer etching. Two samples did not undergo to etching, one pure PEI and one xGnP/PEI sample. These samples had very smooth morphology. Etching times were 1, 3 and 10 hours. It was supposed that PEI layer overcoating the nanoplatelets embedded in nanocomposite foil will be removed employing argon plasma etching without chemical modification of polymer or nanoplatelets.

Samples were observed on polarization optical microscope for detection of differences between not etched and etched surfaces after etching procedure. However, optical microscopy did not serve for analysis, but only for the surface imaging. There was not some difference in etched or not etched samples on optical microscope. Imaging was important for right choice of scanning place for Atomic force microscope. SPM device described in chapter 4.4 has the optical microscope for orientation imaging of sample surface. Creating of scale or various defined magnification is not possible on SPM optical microscope. This is the reason, why polarization optical microscope was used. Not etched surface of nanocomposite PEI/xGnP is shown below (Fig. 32).



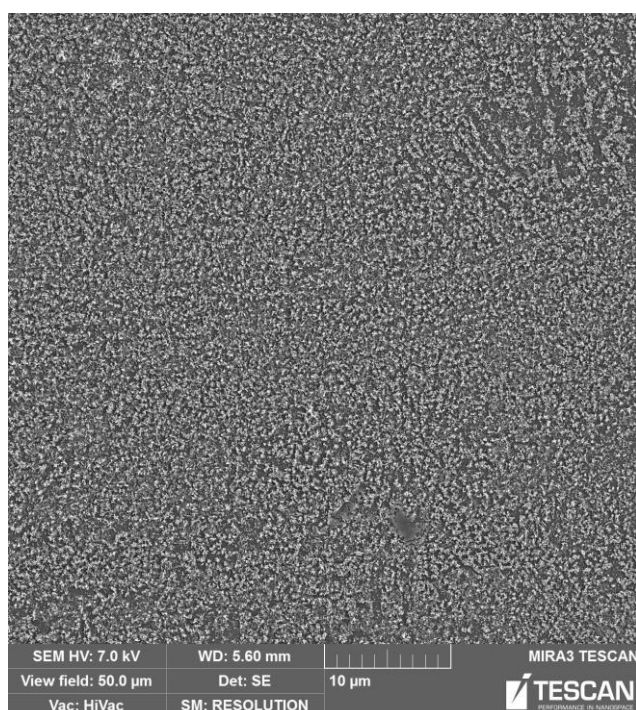
*Fig. 32: Polarization optical microscopy image of not etched nanocomposite xGnP/PEI*

Image represents particles of exfoliated graphite nanoplatelets of various diameters covered by PEI. Simple optical microscope is also part of SPM device, but it has not so much possibilities to set up. This optical microscope was used for finding of scanning area on the sample surfaces.

## 5.2 Scanning electron microscopy

Images from SEM served for comparison of etched and not etched surfaces. Not etched and 10 hours etched pure PEI, not etched, 1, 3 and 10 hours etched nanocomposite xGnP/PEI and xGnP nanosheets on Si substrate were used for SEM analysis. Images with dimensions  $50 \times 50 \mu\text{m}$  and  $10 \times 10 \mu\text{m}$  were performed. All samples were covered by very thin gold layer to avoid charging. In the case of foils layer was 4 nm thick and sample with xGnP on Si substrate had 3 nm thick layer of Au. This layer was created because scanning electron microscopy is usable only for conductive samples and polymer foil is not this case. Method used for covering process is plasma sputtering.

Differences in structure and local etching were observed in the case of pure PEI foil. Structure of the not etched foil is shown on the Fig. 33 and its detail on Fig. 34.



*Fig. 33: SEM image of not etched pure PEI surface  $50 \times 50 \mu\text{m}$*

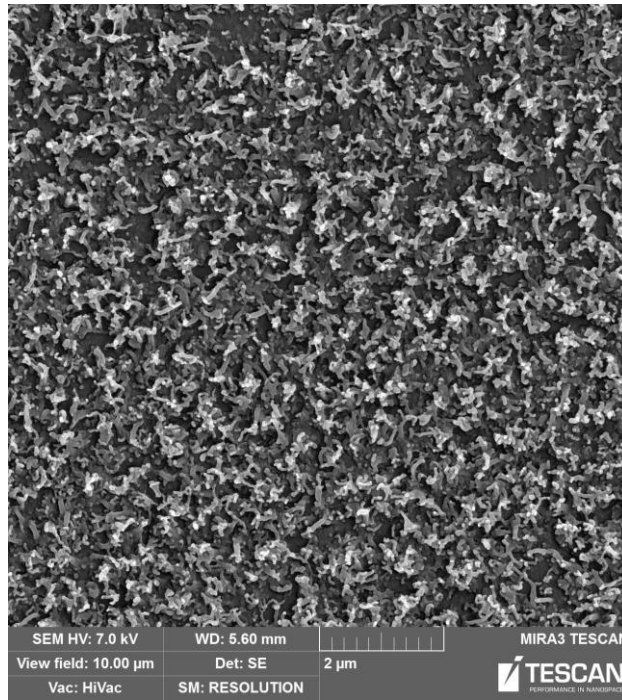


*Fig. 34: SEM image of not etched pure PEI surface  $10 \times 10 \mu\text{m}$*

As mentioned above, surface of the foils was covered by 4 nm thick layer of gold. Formations on the surface could be flaking layer of gold and we are unable to observe covered structure of the PEI foil. Reason is probably bad adhesion of gold layer to PEI surface. On the big image are seen some defects. It probably created during manufacturing of the PEI foil. Detail image shows moss structure of polyetherimide. Changes in the structure of PEI are shown on the 10 hours etched sample (Fig. 35) and detail local etches are mentioned on the Fig. 36.

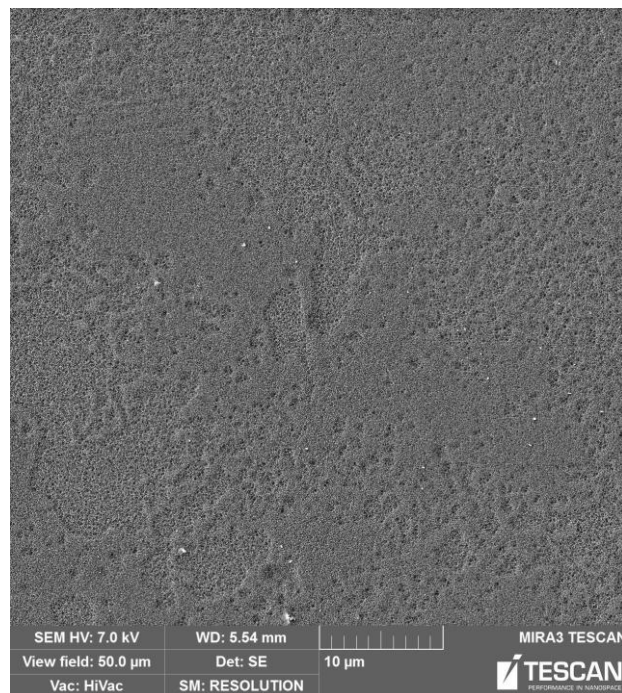


*Fig. 35: SEM image of 10 hours etched pure PEI surface  $50 \times 50 \mu\text{m}$*

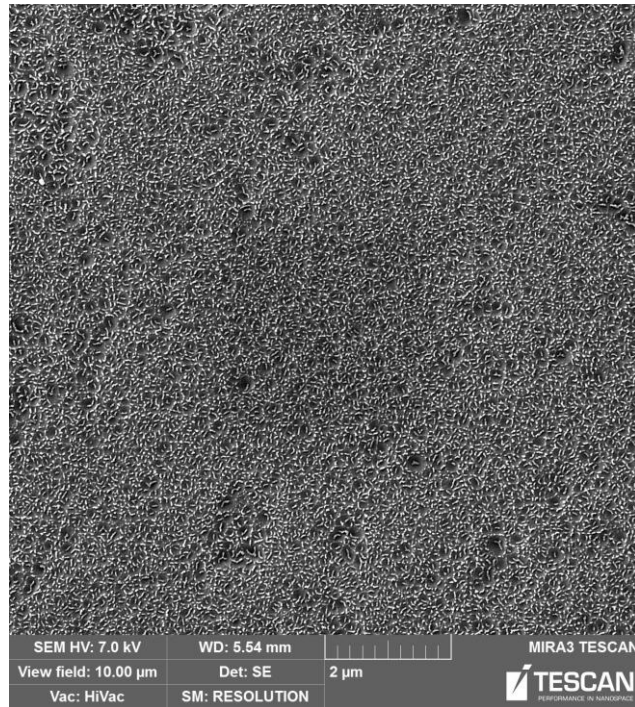


*Fig. 36: SEM image of 10 hours etched pure PEI surface  $10 \times 10 \mu\text{m}$*

This sample has different structure unlike not etched PEI foil. Local etches are visible on the detail image as a small wells. Etching was on all area, but some places were etched deeper and somewhere only on surface.

In the case of nanocomposite foil are visible changes in the times of etching.

Not etched sample is imaged on the Fig. 37 and its detail on the Fig. 38.

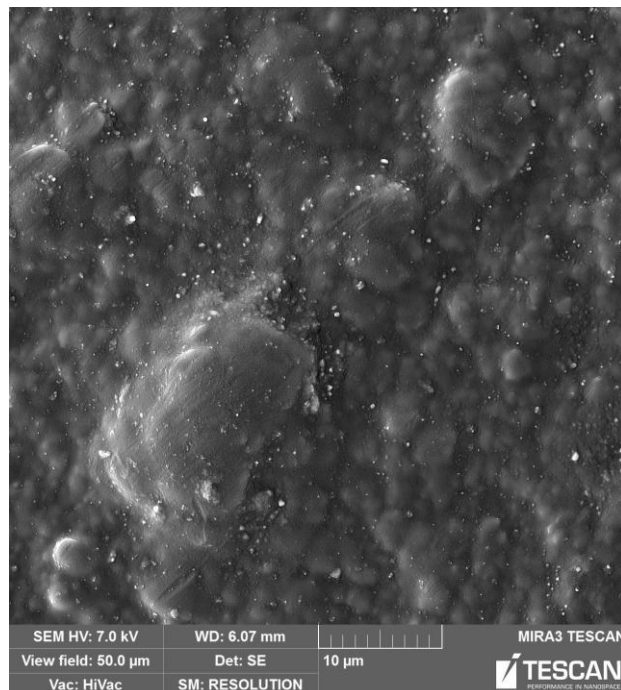


*Fig. 37: SEM image of not etched xGnP/PEI surface  $50 \times 50 \mu\text{m}$*

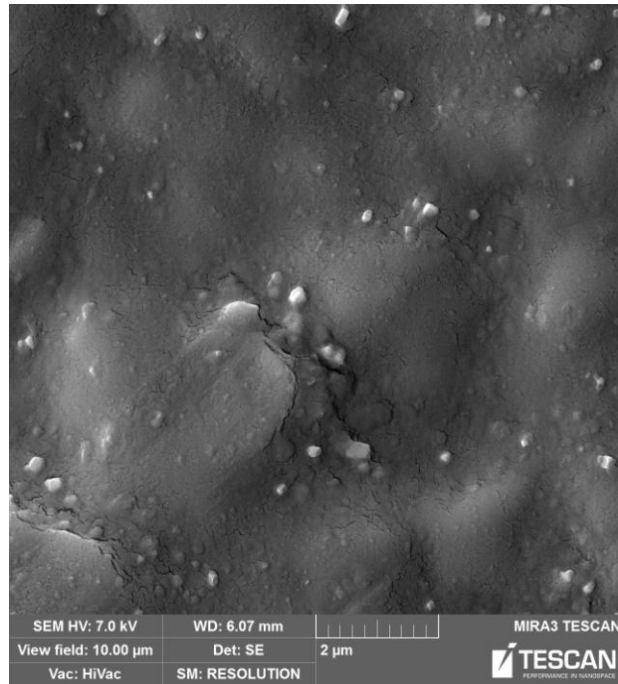


*Fig. 38: SEM image of not etched xGnP/PEI surface  $10 \times 10 \mu\text{m}$*

Exfoliated graphite nanoplatelets are visible on the images and are covered by thin layer of polymer, which was etched away in further cases. Agglomerates of xGnP and separate nanoplatelets are visible on the Fig. 37. Edges of xGnP are visible in the middle of the image. Drzal et al. [2] showed structure of HDPE with xGnP, common features are obvious, but xGnP/HDPE system has larger diameter of reinforcement.

Sample, which was etched by plasma 1 hour, is shown in the Fig. 39. Detail of xGnP in PEI is on the Fig. 40.

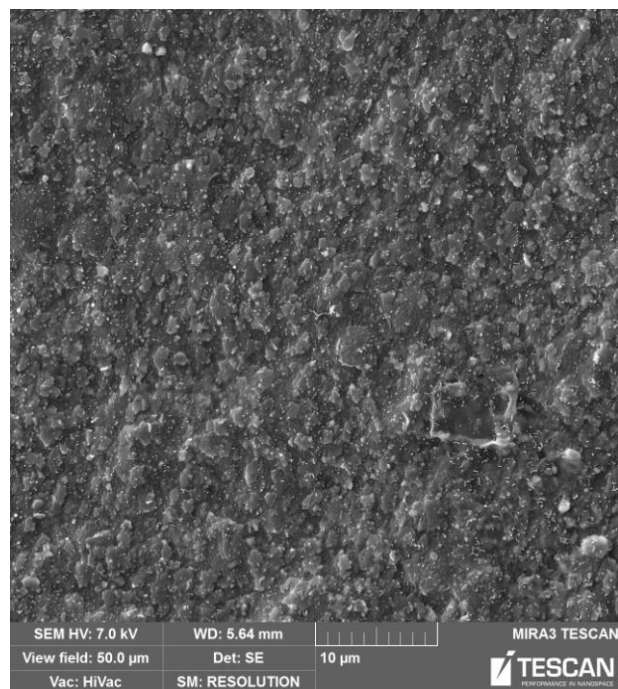


*Fig. 39: SEM image of 1 hour etched xGnP/PEI surface  $50 \times 50 \mu\text{m}$*

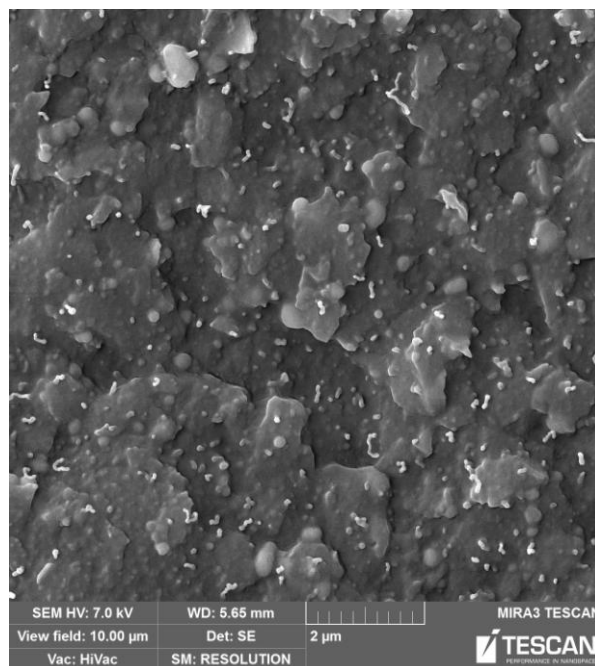


*Fig. 40: SEM image of 1 hour etched xGnP/PEI surface  $10 \times 10 \mu\text{m}$*

Small white formations are visible on both images; it could be flaking gold layer as in the case of not etched PEI foil. Particularly embedded nanoparticles are visible in PEI matrix. Some of them are completely covered by polymer. Graphene nanosheets are deployed in many planes of the foil thickness. It can be seen that nanoplatelets have various diameters and shapes and are similar to particles embedded in PP, observed by Drzal et al. [3]

Some remains of polymer PEI are also visible on the sample, which was etched for 3 hours. Surveillance image and its detail are shown on the Fig. 41 and 42, respectively.

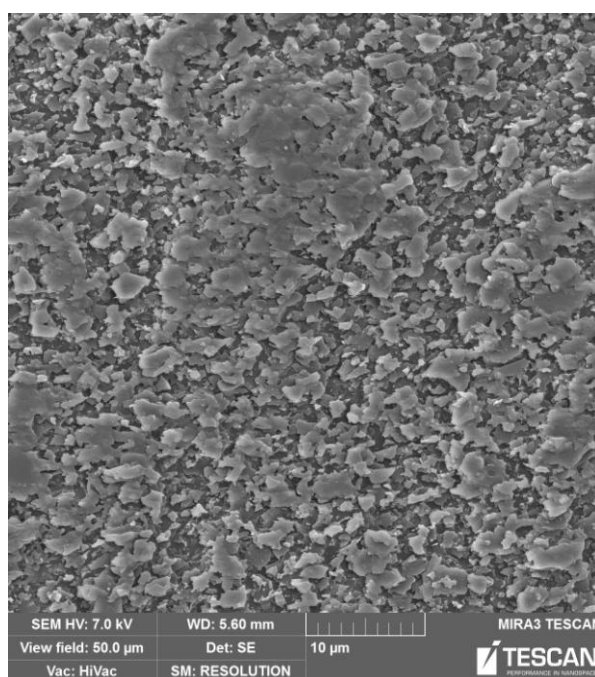


*Fig. 41: SEM image of 3 hours etched xGnP/PEI surface  $50 \times 50 \mu\text{m}$*

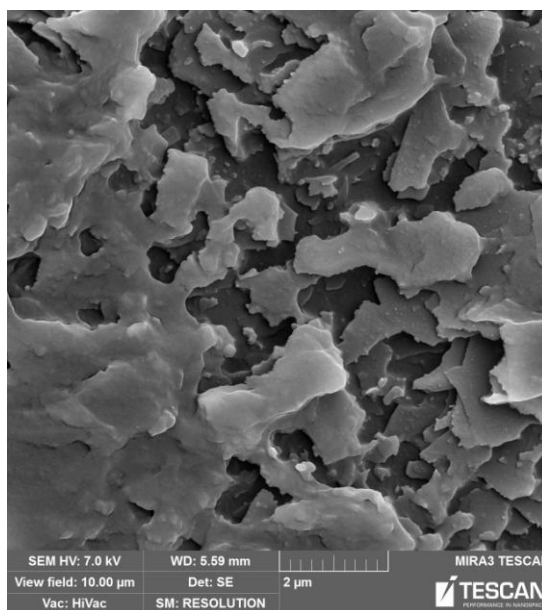


*Fig. 42: SEM image of 3 hours etched xGnP/PEI surface  $10 \times 10 \mu\text{m}$*

Both agglomerates and separately nanoparticles we can see here. Exfoliated graphite nanoplatelets of various shapes and diameters are visible. Detailed image shows agglomerate of xGnP particularly covered by polymer. Three hours of plasma etching allowed uncovering most of xGnP particles. Shape and diameter of particles corresponds with research of Drzal et al. [15], where influence of compounding and effect of reinforcement content was observed.

10 hours of etching were enough for removal of polymer from the surface. Some remains of polymers could be under nanoparticles, but it is not visible. (Fig. 43). Detail of particles is on Fig. 44.

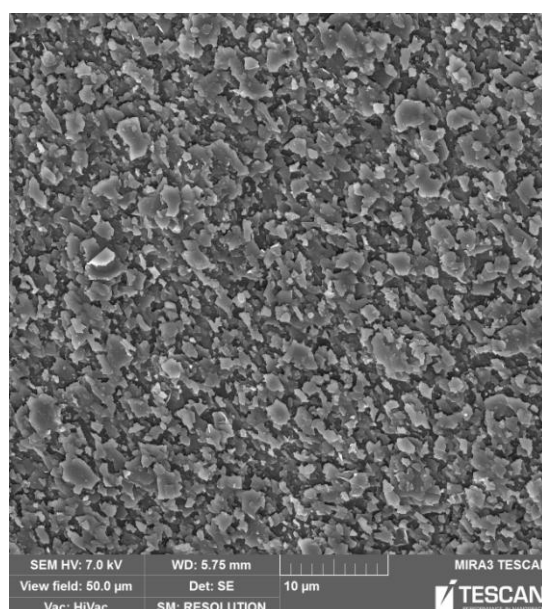


*Fig. 43: SEM image of 10 hours etched xGnP/PEI surface  $50 \times 50 \mu\text{m}$*

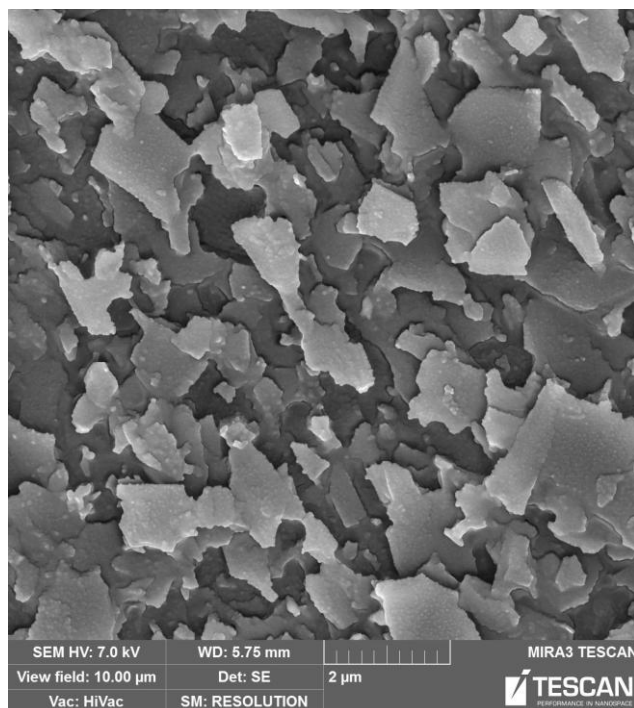


*Fig. 44: SEM image of 10 hours etched xGnP/PEI surface  $10 \times 10 \mu\text{m}$*

Ten hours of etching allows complete removing of the polymer from the surface of the sample. Graphite nanoplatelets are clearly visible both in the form of agglomerates and separate nanoparticles. Exfoliated graphite nanoflakes have various diameters and shapes. It is probably not possible to control distribution of diameters during manufacturing of both acid intercalated graphite and microwave expanded graphite. [4]

One sample was prepared for evidence of identity xGnP particles. This sample was prepared on the silicon substrate. Self assembled layer was prepared on this Si substrate for cover of hydrophobic surface. Agglomerates of xGnP particles were dispersed in pure chloroform. One small drop was transferred due the capillary on the surface. This sample was observed by scanning electron microscope. Image of big agglomerate and separate group of nanoplatelets are shown on the Fig. 45 and 46, respectively.

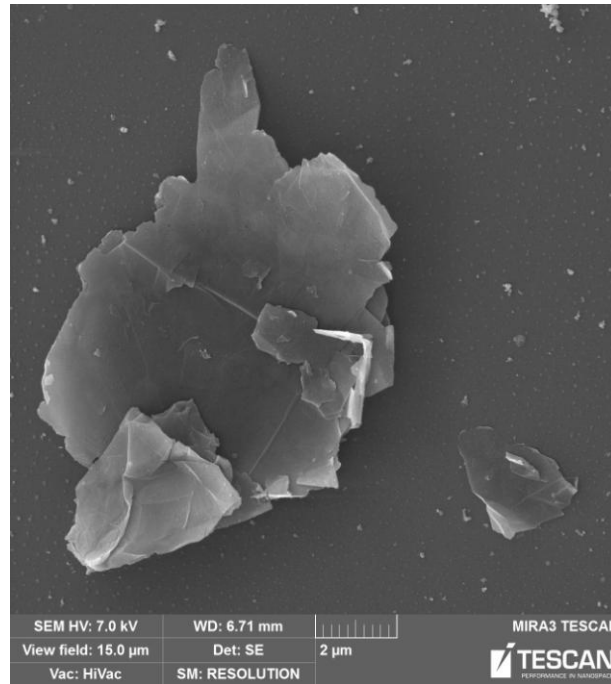


*Fig. 45: SEM image of xGnP agglomerate  $15 \times 15 \mu\text{m}$*

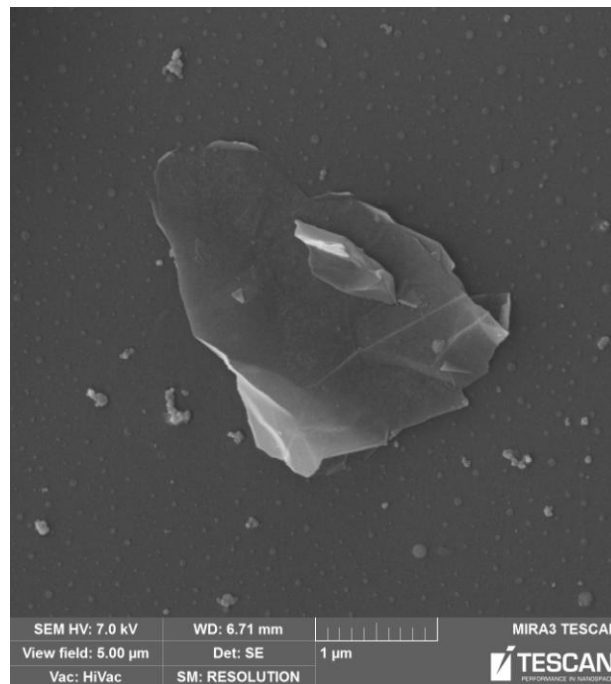


*Fig. 46: SEM image of single xGnP particle  $5 \times 5 \mu\text{m}$*

It is visible from Fig. 45 above that graphite nanoflakes have irregular shapes and lay under various angles. Diameters of agglomerates are very similar to exfoliated graphite (xGnP15) manufactured by Drzal et al. [4] Nanoplatelet consisted from few graphite particles is seen on the lower image. Edges of these particles are apparent. Nanoplatelets on this image are very similar to poly(diallyldimethylammonium chloride)/sulfated poly(styrene) PDAC/SPS-xGnP observed by Drzal's group [13], but our particles have larger diameter.

### 5.3 Atomic force microscopy

Atomic force microscopy is one from possible modes on SPM device. It was used for imaging of surface morphology of prepared samples. Both pure PEI and xGnP/PEI were analysed with all times of etching. NSG 03 cantilever was used for imaging due its good resonance frequency. Parameters of all tips are mentioned in Table 12 in chapter 4.4.3. Sizes of all scans were  $50 \times 50 \mu\text{m}$  and details with size  $10 \times 10 \mu\text{m}$  were chosen from these images.

Changes in surface structure of the PEI foil were observed. It was expected that higher time of etching leads to creation of local failures of surface. Nanocomposite xGnP/PEI has rich morphology and uncovering of nanolayered particles of graphite is aim of etching of this material. Higher time of etching leads to disappearance of polymer. Differences in etching process in the case both pure PEI and xGnP/PEI can be seen on images below.

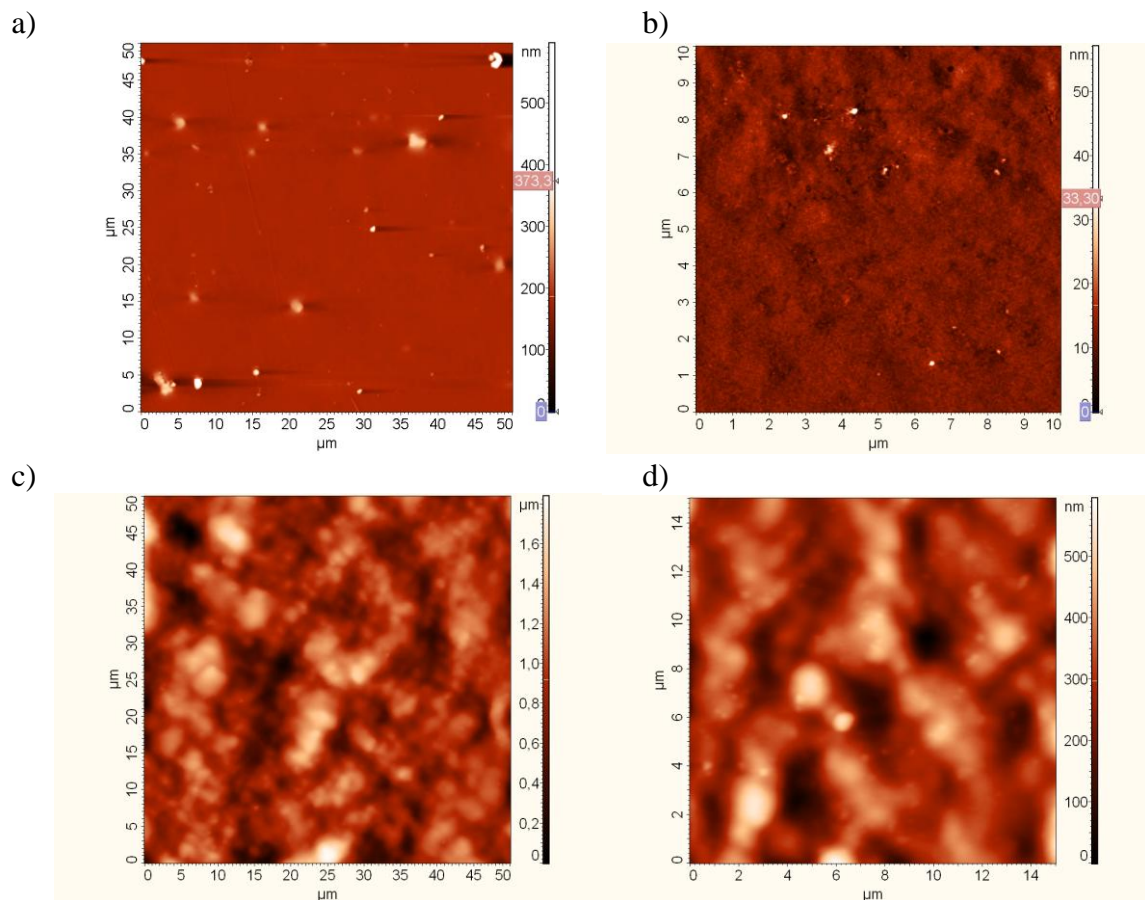


*Fig. 47: AFM image of not etched pure PEI  $50 \times 50 \mu\text{m}$  (a) and its detail  $10 \times 10 \mu\text{m}$  (b) and nanocomposite xGnP/PEI  $50 \times 50 \mu\text{m}$  (c) and its detail  $10 \times 10 \mu\text{m}$  (d)*

Big differences between pure and composite foil in the morphology can be observed. Pure PEI foil is relatively smooth with defects on surface, see on Fig. 47a, and composite foil has hilly surface with visible areas, where are xGnP particles, see on Fig. 47b. Defects and formations, for example disparities or hollows on the PEI foil, can be caused during manufacturing of the foils. Nanocomposite sample has similar defects, but it is not seen due the morphology.

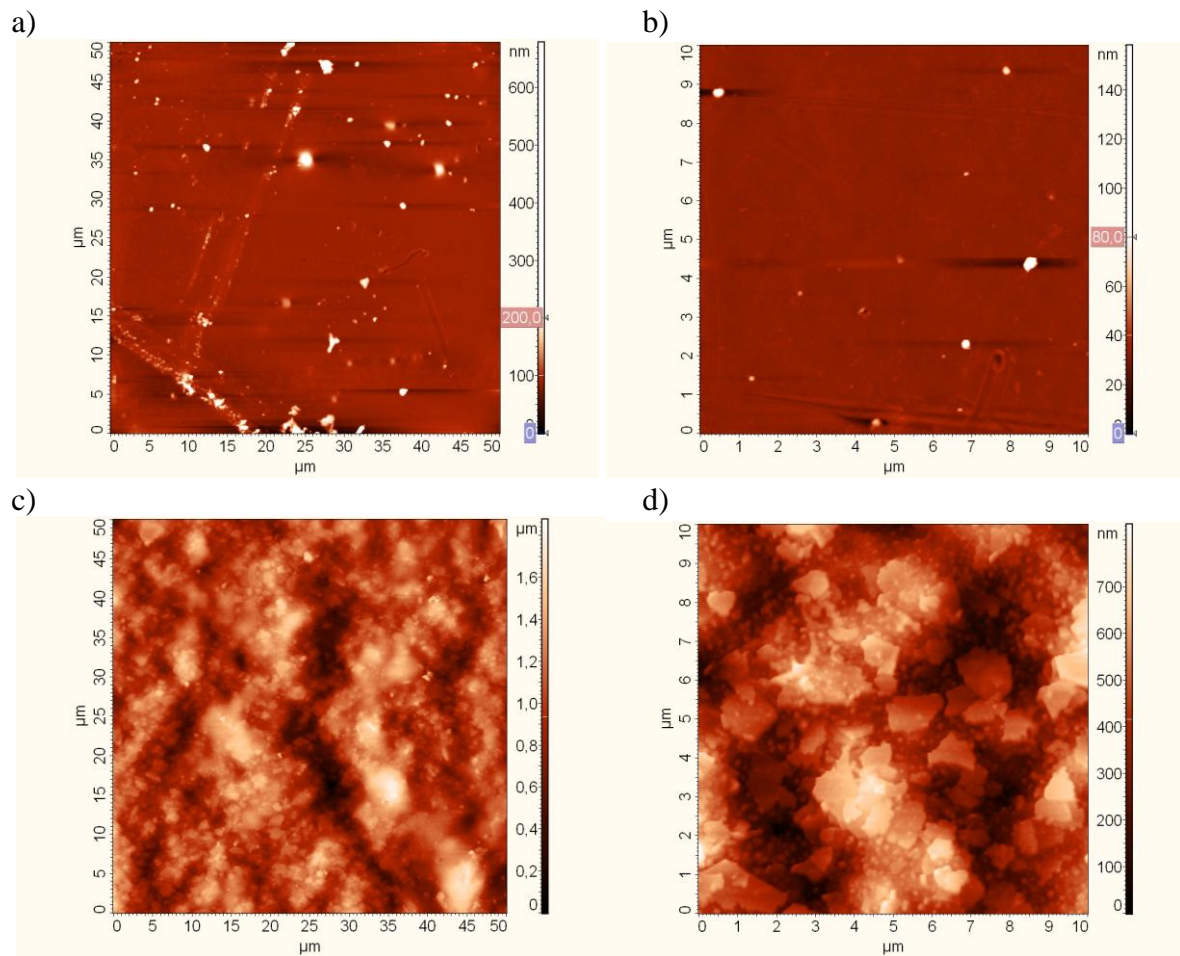


*Fig. 48: AFM image of 1 hour etched pure PEI  $50 \times 50 \mu\text{m}$  (a) and its detail  $10 \times 10 \mu\text{m}$  (b) and nanocomposite  $x\text{GnP/PEI } 50 \times 50 \mu\text{m}$  (c) and its detail  $10 \times 10 \mu\text{m}$  (d)*

Defects of the PEI foil are seen on the pictures, which created during manufacturing of the foil (Fig. 48a, b). These formations on the surface have influence on height topography and roughness properties of the sample. Influence of etching is not visible after one hour. Etching of nanocomposite foil showed exfoliated graphite nanoplatelets on some places of scanned area (Fig. 48c). It could be seen better on the detail of the image. It is distinct from the picture that some nanosheets of graphite are lower than another. Darker colour means that the particle is below. Diameters of particles are in range from  $0.5\text{--}2 \mu\text{m}$ . Some rests of polymer are still visible.

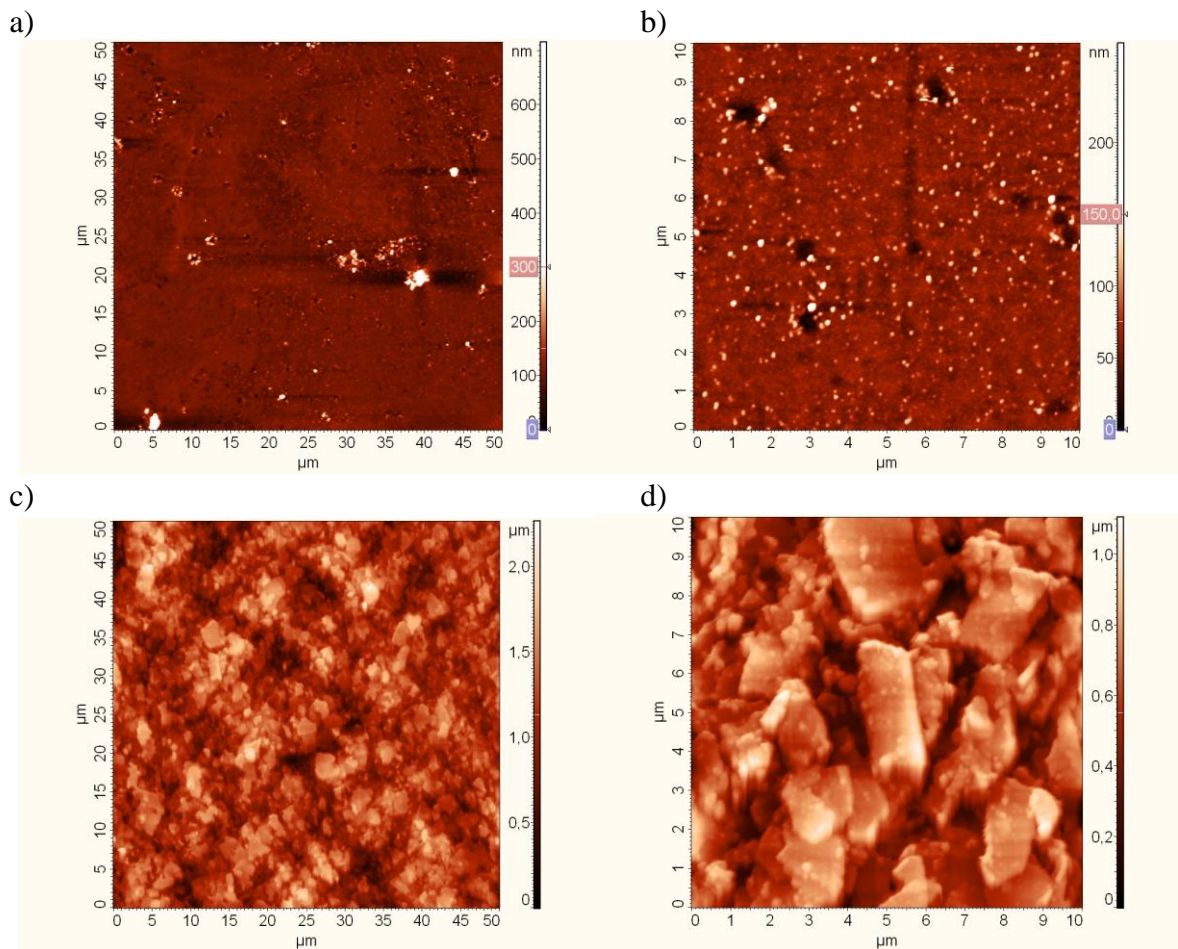


*Fig. 49: AFM image of 3 hours etched pure PEI  $50 \times 50 \mu\text{m}$  (a) and its detail  $10 \times 10 \mu\text{m}$  (b) and nanocomposite xGnP/PEI  $50 \times 50 \mu\text{m}$  (c) and its detail  $10 \times 10 \mu\text{m}$  (d)*

Some etched places are seen on the pure PEI foil. One can see from the picture that etching took place locally in depth to the sample (Fig. 49b). Some holes are larger. It can mean a presence of some defects of the material. These defects can be bubbles or disparities and can impinge structure of the sample. Nanocomposite foil has etched surface and xGnP particles are seen very good. Some rests of polymer are among and on the particles. Angles of tilt of particles are various, seen on the detail image. Particles diameters are very different, and unlike from 1 hour etched samples one can see particles large up to  $4 \mu\text{m}$ .

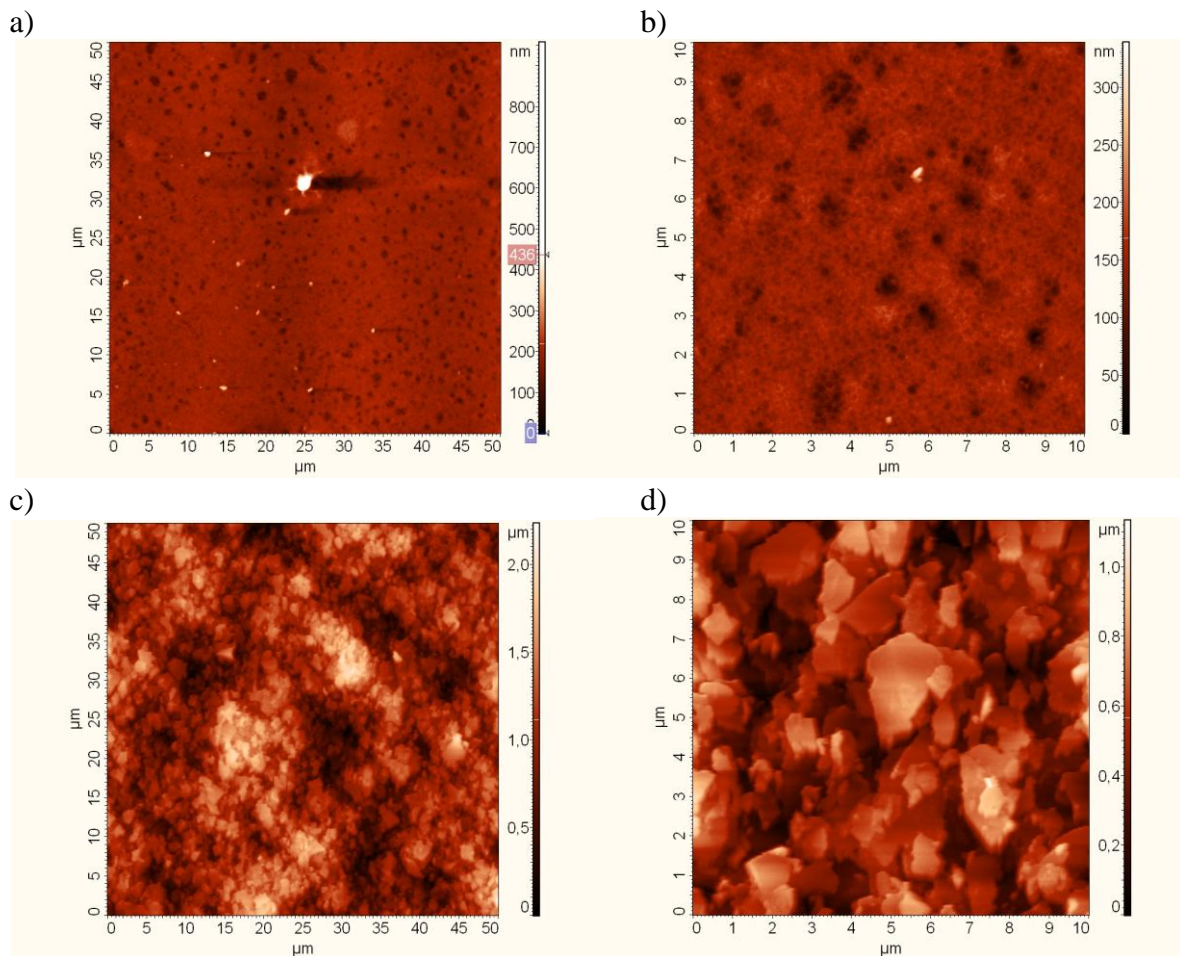
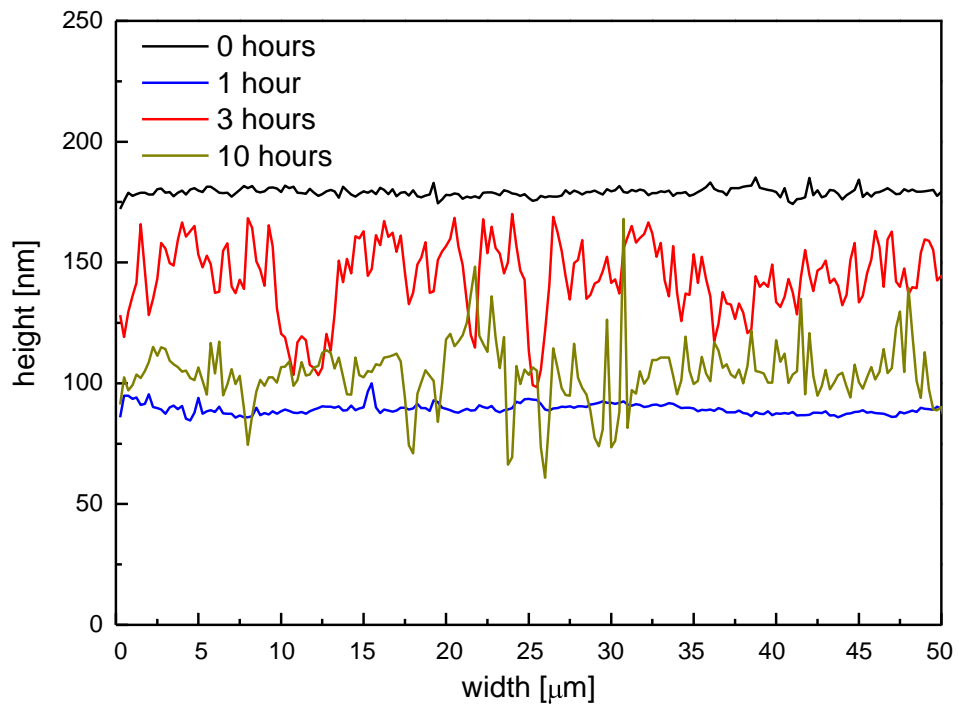


*Fig. 50: AFM image of 10 hours etched pure PEI  $50 \times 50 \mu\text{m}$  (a) and its detail  $10 \times 10 \mu\text{m}$  (b) and nanocomposite  $x\text{GnP/PEI } 50 \times 50 \mu\text{m}$  (c) and its detail  $10 \times 10 \mu\text{m}$  (d)*

10 hours of etching time is enough for visible changes in the structure of both PEI sample without xGnP particles and xGnP/PEI nanocomposite (Fig. 50). A lot of dark fields of various diameters can be seen on  $50 \times 50 \mu\text{m}$  area of the PEI foil. Etched surface of the sample are these areas. On the detail image is seen that one larger etched area contains from small holes. In the case of polymer nanocomposite is clear that matrix is totally etched from the surface. It is possible that some polymer is under the particles, but it is not seen. Other variant can be that under particles can be other particles. This is a reason, why can material exhibit different mechanical properties in various places of the surface. Mechanical properties are probably unevenly distributed over the surface.

Two dimensional mapping in the software is recorded during scanning. Profiles are summarized in plots as a dependence of height in nm on width for better demonstration (one size of scanning area, this mean 50 or 10  $\mu\text{m}$ ). First two plots (Fig. 51) show morphologies of the PEI foil a) and nanocomposite xGnP/PEI  $50 \times 50 \mu\text{m}$  b). Fig. 52 shows same properties, but for detail view.

a)



b)

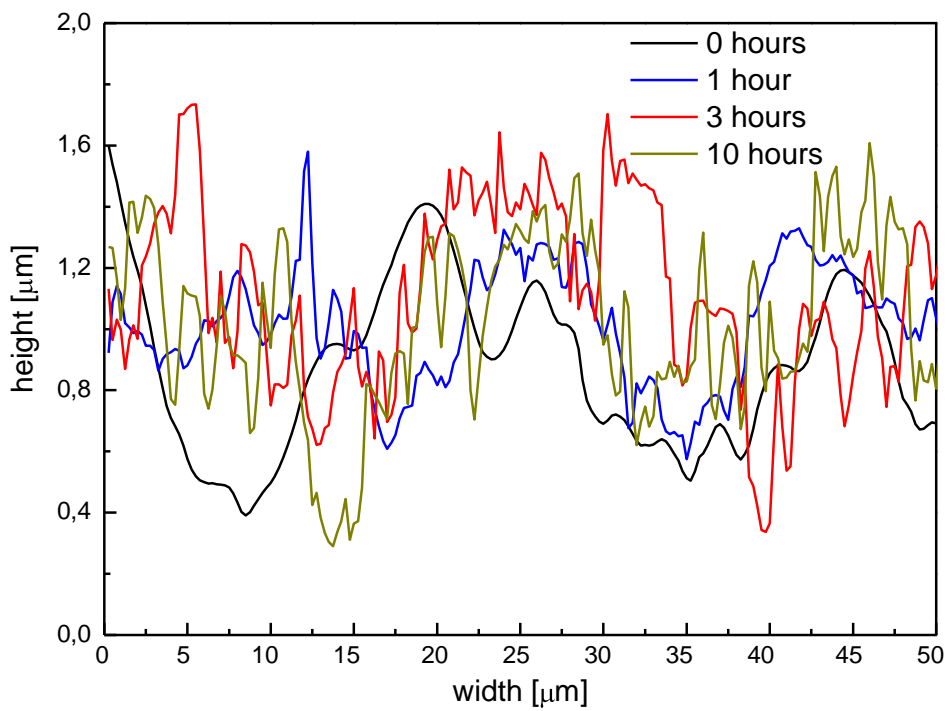
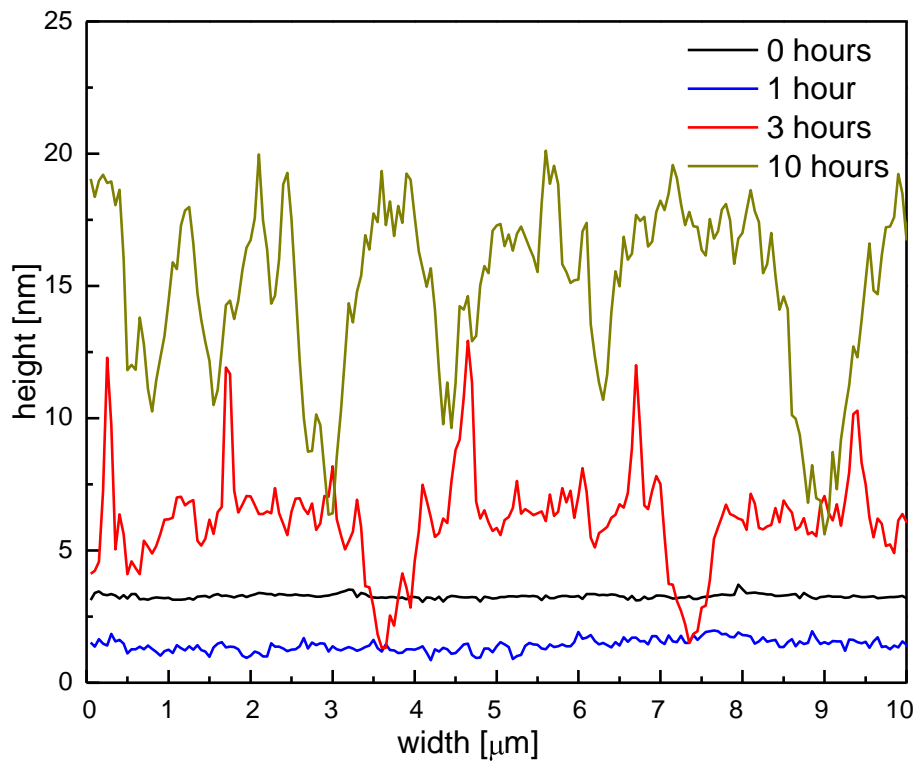


Fig. 51: Profiles showing morphology of samples  $50 \times 50 \mu\text{m}$  a) pure PEI, b) xGnP/PEI

a)



b)

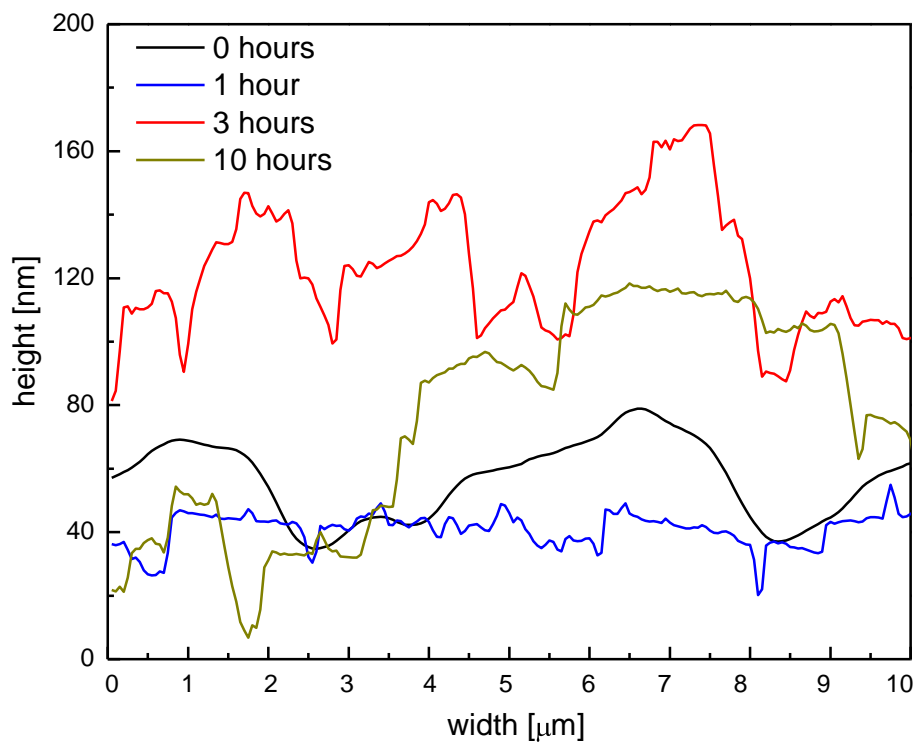


Fig. 52: Profiles showing morphology of samples  $10 \times 10 \mu\text{m}$  a) pure PEI, b) xGnP/PEI

Both Fig. 51 and 52 shows that surface of pure PEI is relatively smooth. Samples, which have not etched and 1 hour etched surfaces, have not failures in structure. Etching is not seen here. Local holes are visible on the samples of the PEI foil, which were etched 3 and 10 hours. Nanocomposite sample, which was not etched (black line) has hilly morphology, but it is continuous without sharp edges. This means that nanosheets of graphite platelets are covered with polyetherimide in this case. This polymer is also apparent on 1 hour etched sample, but local etchings are visible. In the case of 3 and 10 hours etched sample is polymer either under particles or only at the edges of the particles.

Detail profiles show holes after etching, it is especially visible in the case of 3 and 10 hours etched pure PEI foil. On 3 hours etched sample are visible probably deposited particles (five red peaks). Detail profiles of composites show gradual uncovering of particles with increasing times of etching. Outlines of xGnP are visible from this plot.

Roughness properties as Root Mean Square (RMS) roughness, peak to peak and autocorrelation length (ACL) were evaluated for all samples. RMS is a parameter characterizing various disparities in Z-axis. Peak to peak is the difference between the highest and the lowest point on the analyzed area. ACL characterizes surface roughness in X and Y directions and it is suitable for relatively smooth properties with topography in range of nanometres. This is a reason, why results of this parameter were not reproducible for nanocomposite xGnP/PEI.

All roughness properties for analyzed samples are summarized in Table 13 for  $50 \times 50 \mu\text{m}$  and 14 for  $10 \times 10 \mu\text{m}$ .

Table 13: Roughness properties of the samples –  $50 \times 50 \mu\text{m}$

<b>pure PEI</b>			<b>xGnP/PEI</b>		
<b>not etched</b>	RMS [nm]	15.9	<b>not etched</b>	RMS [nm]	245
	peak to peak [nm]	596		peak to peak [ $\mu\text{m}$ ]	1.83
	ACL [ $\mu\text{m}$ ]	0.59		ACL [ $\mu\text{m}$ ]	2.15
<b>1 hour etched</b>	RMS [nm]	18.1	<b>1 hour etched</b>	RMS [nm]	253
	peak to peak [nm]	677		peak to peak [ $\mu\text{m}$ ]	1.87
	ACL [ $\mu\text{m}$ ]	0.39		ACL [ $\mu\text{m}$ ]	1.96
<b>3 hours etched</b>	RMS [nm]	26.3	<b>3 hours etched</b>	RMS [nm]	284
	peak to peak [nm]	714		peak to peak [nm]	2.26
	ACL [ $\mu\text{m}$ ]	0.39		ACL [ $\mu\text{m}$ ]	1.18
<b>10 hours etched</b>	RMS [nm]	37.8	<b>10 hours etched</b>	RMS [nm]	323
	peak to peak [nm]	989		peak to peak [ $\mu\text{m}$ ]	2.23
	ACL [ $\mu\text{m}$ ]	2.74		ACL [ $\mu\text{m}$ ]	2.16

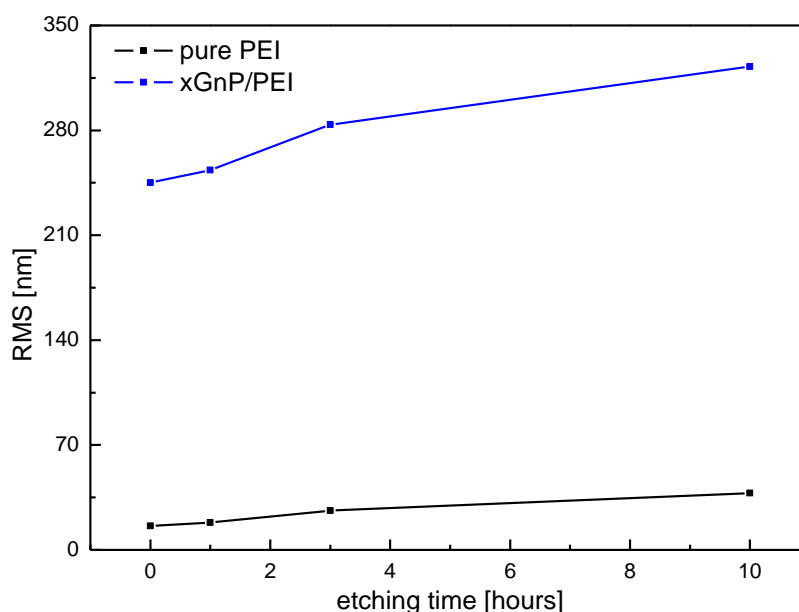
Table 14: Roughness properties of the samples –  $10 \times 10 \mu\text{m}$

pure PEI			xGnP/PEI		
not etched	RMS [nm]	2.11	not etched	RMS [nm]	84.6
	peak to peak [nm]	57.0		peak to peak [nm]	594
	ACL [ $\mu\text{m}$ ]	0.08		ACL [ $\mu\text{m}$ ]	0.70
1 hour etched	RMS [nm]	3.96	1 hour etched	RMS [nm]	99.3
	peak to peak [nm]	158		peak to peak [nm]	737
	ACL [ $\mu\text{m}$ ]	0.12		ACL [ $\mu\text{m}$ ]	0.70
3 hours etched	RMS [nm]	14.9	3 hours etched	RMS [nm]	142
	peak to peak [nm]	269		peak to peak [ $\mu\text{m}$ ]	1.10
	ACL [ $\mu\text{m}$ ]	0.16		ACL [ $\mu\text{m}$ ]	0.35
10 hours etched	RMS [nm]	19.6	10 hours etched	RMS [nm]	174
	peak to peak [nm]	338		peak to peak [ $\mu\text{m}$ ]	1.13
	ACL [ $\mu\text{m}$ ]	0.15		ACL [ $\mu\text{m}$ ]	0.39

Values of RMS and peak to peak were plotted with time of etching for pure PEI foil and for nanocomposite foil. Plots are both for  $50 \times 50 \mu\text{m}$  and details of these images. Fig. 53 shows increasing trend of root mean square (a) and peak to peak (b) with time of etching.

Both values are higher in the case of nanocomposite, because of an influence of nanoparticles. Value for 3 hours etched sample is bigger than value of 10 hours etched sample in the case of peak to peak of xGnP/PEI nanocomposite. Reason could be defects and holes in the 3 hours etched sample, these factors have influence to roughness properties. Plots for detail images ( $10 \times 10 \mu\text{m}$ ) are shown on Fig. 54a, b.

a)



b)

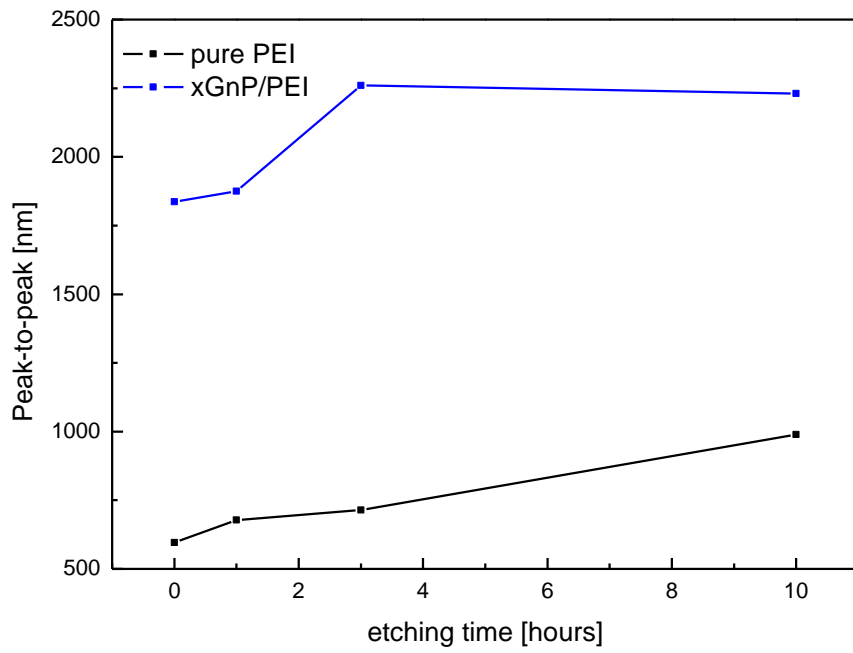
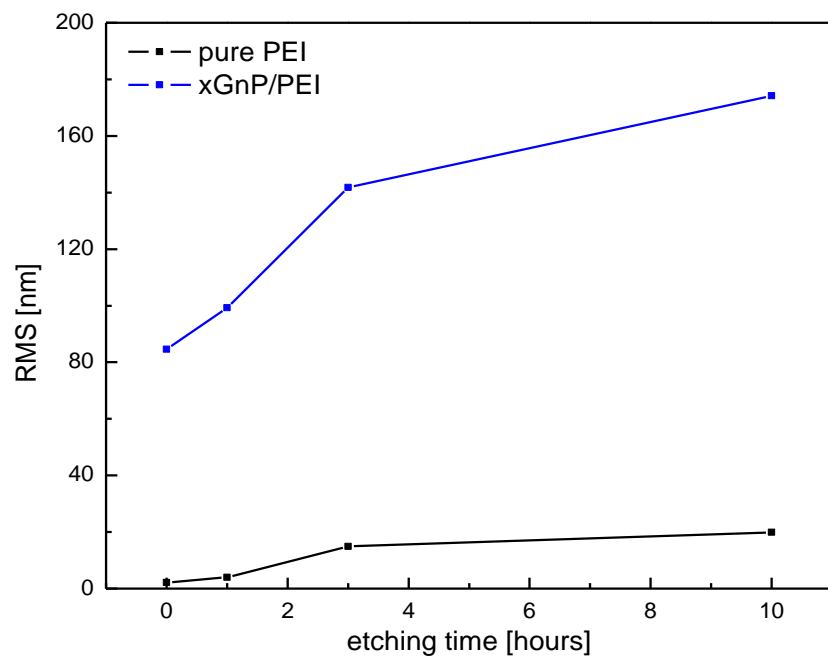


Fig. 53: dependence of a) RMS, b) peak to peak on etching time for  $50 \times 50 \mu\text{m}$

a)



b)

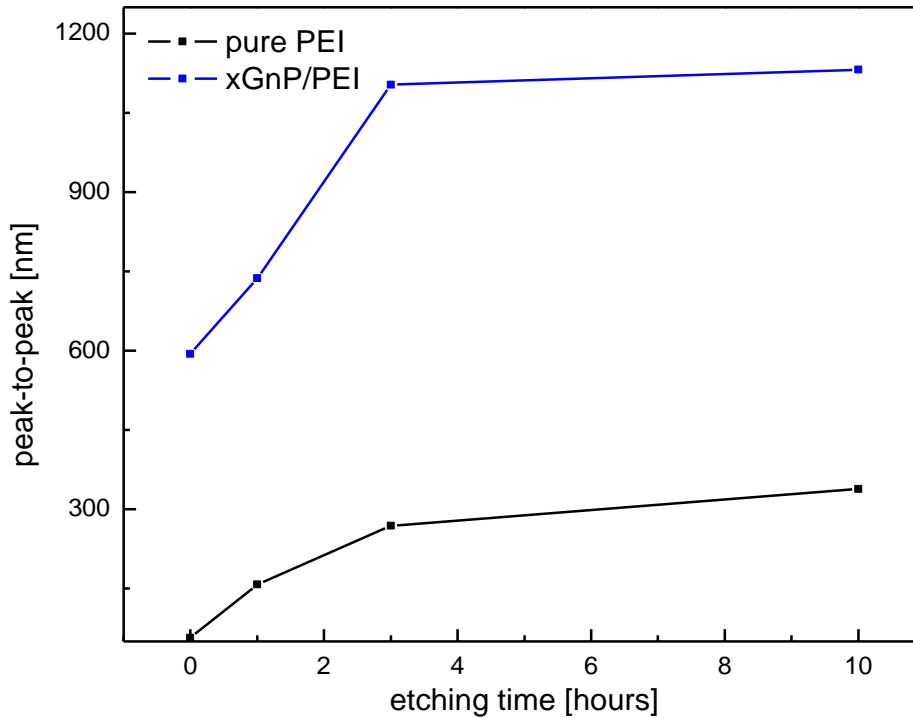


Fig. 54: dependence of a) RMS, b) peak to peak on etching time  $10 \times 10 \mu\text{m}$

### 5.3.1 AFM analysis of separate xGnP

Atomic force microscopy was also performed on separate exfoliated graphite nanoplatelets. Nanosheets in agglomerates were dispersed in chloroform and applied on treated silicon wafer. Thin layer of self-assembled layer was on the silicon wafer.

Optical microscopy is a part of SPM device and served for finding available area for scanning. When single nanoparticle was scanned, profiles were performed for detecting of the nanosheet surface. It was expected that surface of the nanoplatelets will be very smooth and height between highest point of the nanoparticle and silicon wafer will be in units of nanometres. AFM image of xGnP agglomerate is shown on the next side. On the picture below (Fig. 55) is shown that some graphene nanosheet is in horizontal position and other in vertical position. Vertical position of xGnP in agglomerate leads to bigger height deviation. Surface of the nanoparticle is very rough and does not resemble single graphene nanosheet. Particle could be included to microscale rather than nanoscale. AFM image of xGnP was performed also by Deng et al. [17], but nanoplatelets were imaged only in vertical position. Shape and dimensions of xGnP are not visible from this AFM images.

Profile across the surface of imaged graphite nanoplatelet is shown on Fig. 56 a) the highest point, b) the deepest point. Profiles were performed three times in horizontal direction and two times in vertical direction (yellow lines on the Fig. 55). Profiles show relatively big height difference between nanoplatelet and substrate.

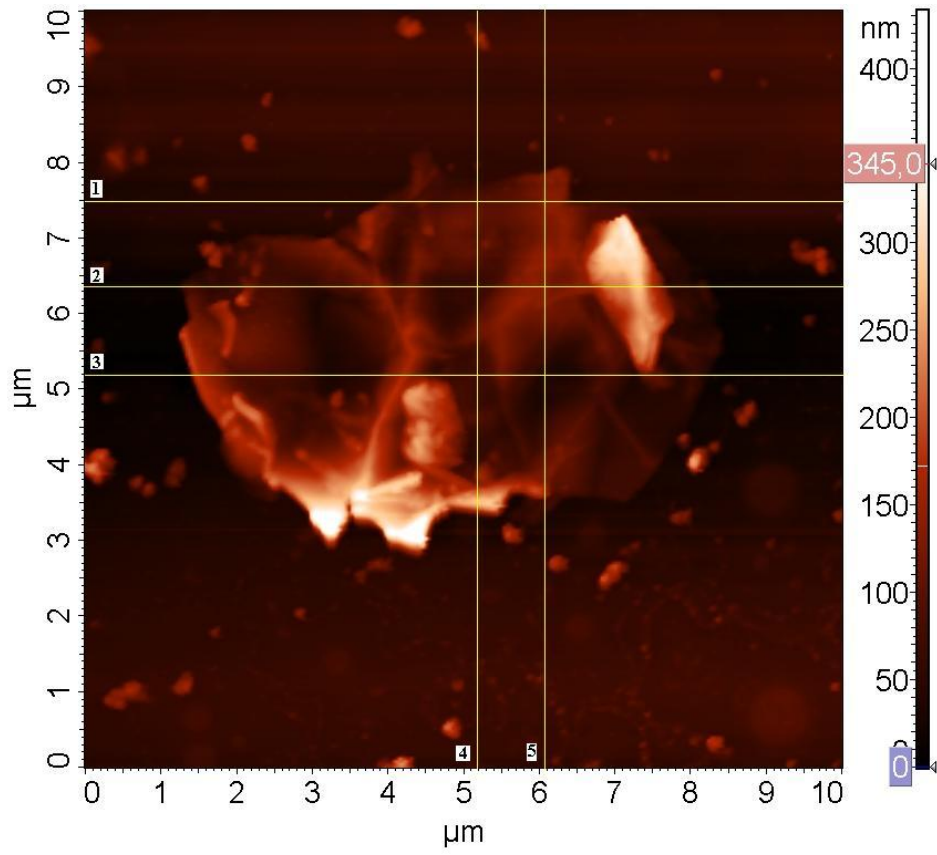
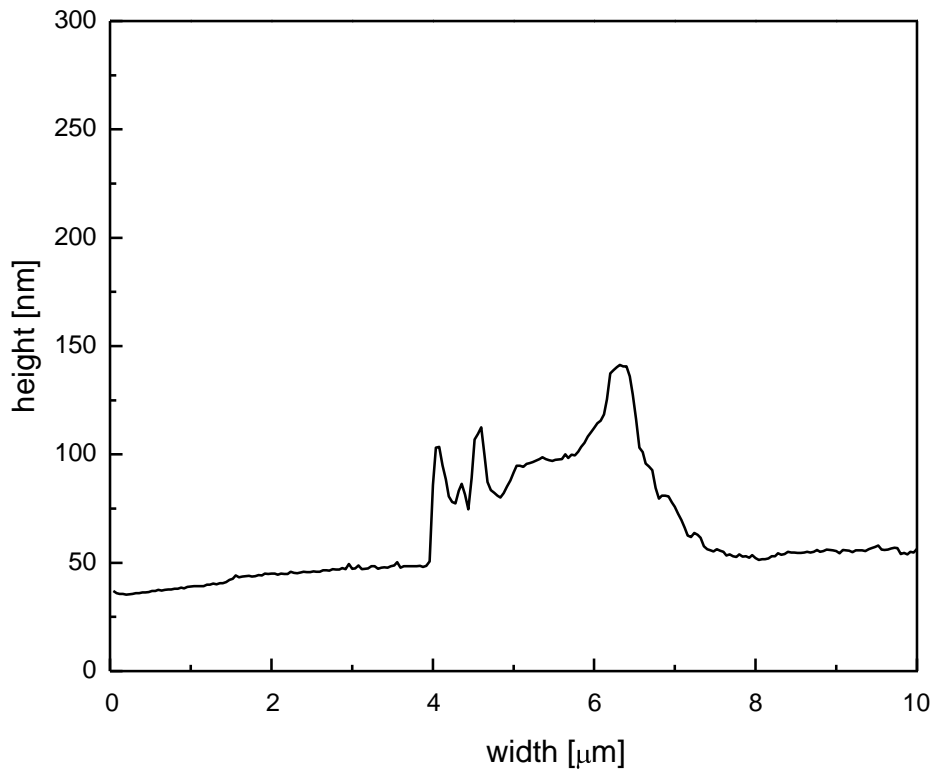
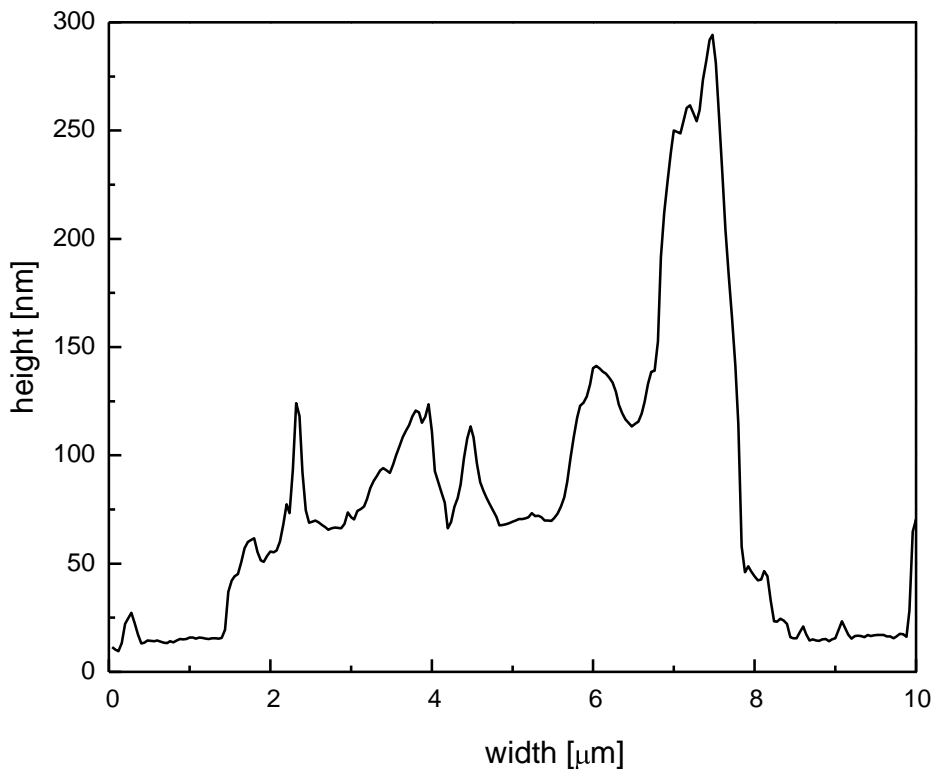


Fig. 55: AFM image of agglomerate of xGnP with profile cuts

a)



b)



*Fig. 56: Horizontal profiles of xGnP a) line 1, b) line 2*

Shape of the nanoparticle and lines, where were profiles performed is shown on the AFM image. Line 1 is for showing of height difference between Si substrate and the nanoparticle. This difference is approximately 100 nm, which is shown on Fig. 56a. One graphene sheet has tenths of nanometres so this layer consists from tens or hundreds of graphene nanosheets. Fig. 56b shows topography of the nanoparticle. It is apparent that the nanoparticle is broken on some places and AFM image shows edges of these breaks. It is mentioned as high peaks on the plot. The highest peak illustrates xGnP in the vertical direction and increases the height axis.

### **5.3.2 Atomic force acoustic microscopy (AFAM)**

Atomic force acoustic microscopy is useful method for mapping of smooth surfaces with anisotropic distribution of mechanical properties. This method was used for distinction of mechanical properties of polymer matrix and xGnP particles. Cantilevers CSG10 and FMG01 were used for scanning. Height and magnitude signal were recorded. Surface is very rough for this analysis and method is not suitable for our samples. Height signal (a) and magnitude signal (b) of 1 hour etched nanocomposite foil is seen on the Fig. 56. Magnitude image shows edges of the nanoparticles, this means, that surface was too ragged for right imaging.

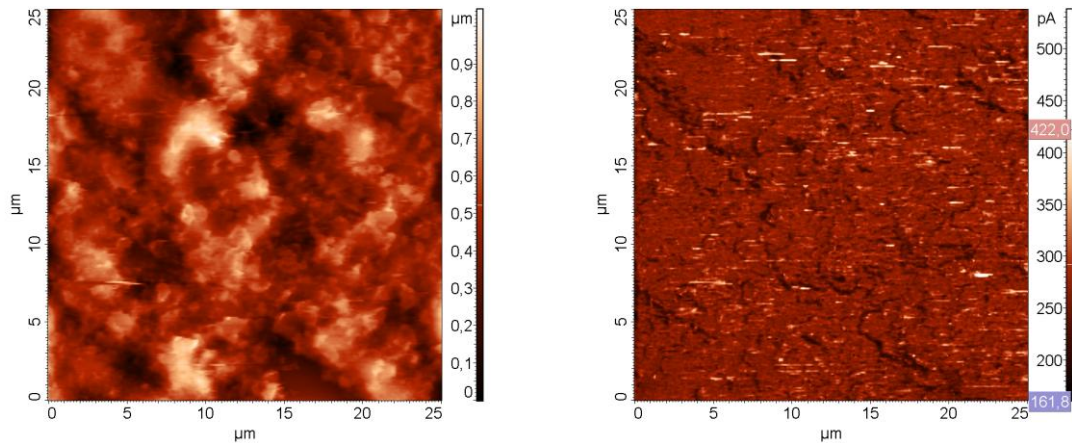
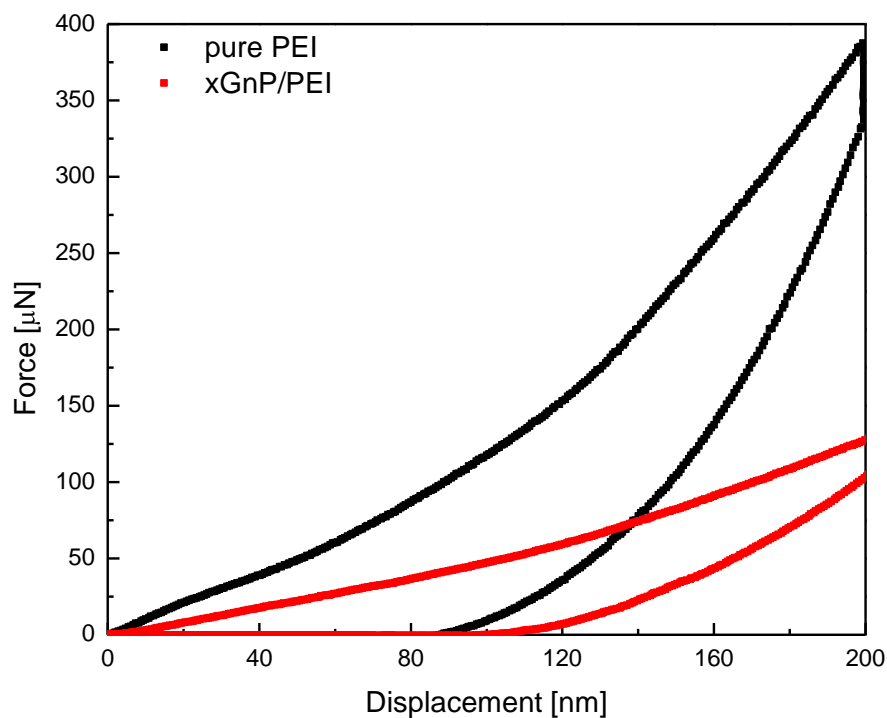


Fig. 56: Image of 1 hour etched xGnP/PEI nanocomposite; a) height map, b) mag signal

#### 5.4 Nanoindentation test

Nanoindentation tests were performed on not etched sample of pure PEI and 3 hours etched sample of nanocomposite xGnP/PEI foil. This method was not ever performed on xGnP particles before. Nanoindentation consisted from measuring of force – displacement dependence of pure PEI and xGnP/PEI, where displacement values were 100, 150, 200, 250, 300, 350 and 400 nm. Maximal values of peak force were plotted as the dependence of load – displacement. Values of Young’s modulus and hardness were established and plotted with contact depth in the Triboscan programme. Average values of Young’s modulus and hardness were calculated and marked to the plot. Examples of force – displacement curves are shown on the Fig. 57 a) 200 nm and b) 400 nm.

a)



b)

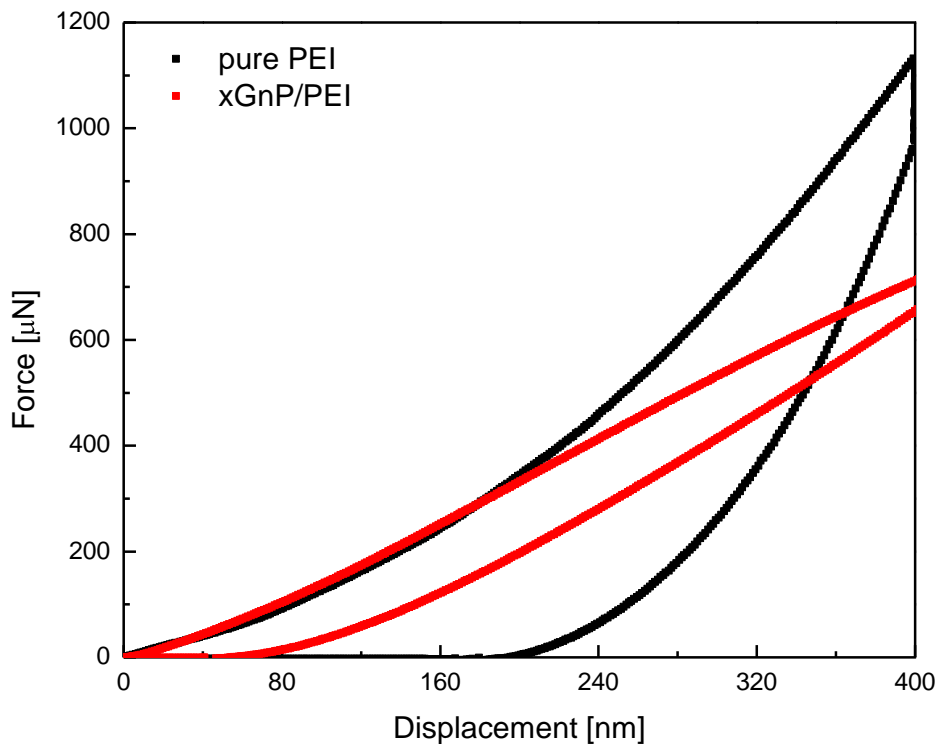


*Fig. 57: Force – displacement plots for displacements 200 and 400 nm*

It was expected that force necessary for penetration of the tip to set depth will be bigger in case of nanocomposite foil. Bigger force for pure PEI foil was observed in all cases of displacement setup. Reason is that nanocomposite foil was etched by plasma and polymer matrix could be removed not only from the surface, but also under xGnP particles and it has big influence on the behaviour of the particles. Nanocomposite foil has various mechanical properties on various place of the surface due the distribution of xGnP particles and etching effect. This trend is visible at all cases of various displacements; here are shown only 200 and 400 nm displacements. Maximal values of the force were established from all these dependences and plotted with displacement for comparison of pure PEI and nanocomposite xGnP/PEI foil. This plot is shown below (Fig. 58).

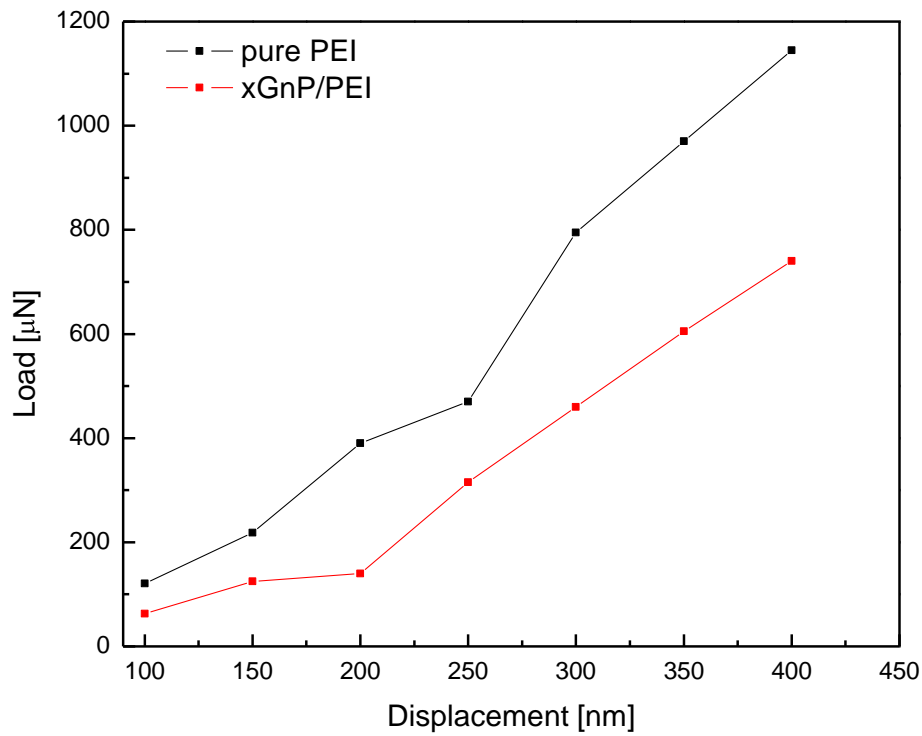


*Fig. 58: Comparison of values of maximal forces for the PEI and nanocomposite foil*

Bigger necessary load for penetration of Berkovich tip is seen on this plot in all cases of the PEI foil. Difference between load value of the PEI and xGnP/PEI is with increasing displacement greater.

Depth profile was performed for not etched PEI foil. Values of Young's modulus and hardness are shown in next plot (Fig. 59). Black line is the average value of Young's modulus evaluated from Hysitron Triboscan programme. Red line is the average value of hardness, which was evaluated same way as Young's modulus.

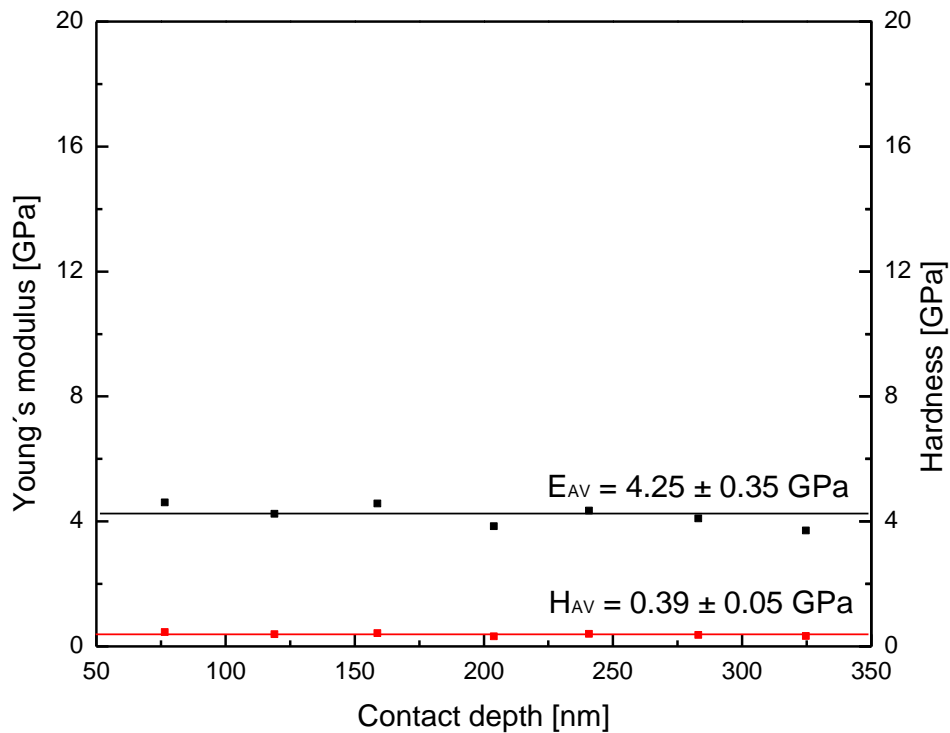


*Fig. 59: Values of Young's moduli and hardness and average values plotted with contact depth*

Values are very similar. It can be seen that values of hardness are lower than Young's modulus. Dispersion of the values is bigger in the case of Young's moduli values.

### 5.5 Nanoscratch test

This test was performed at 10 hours etched sample for indicating of state of xGnP particles after performing of scratch. Hysitron measuring head with conospherical tip was used for scratches. Tip radius was 1  $\mu\text{m}$ . Value of the force for scratching was chosen 5000  $\mu\text{N}$ . Scratches with lower force were not visible on the surface after scanning.

Fig. 60 shows image of scratch in nanocomposite foil.

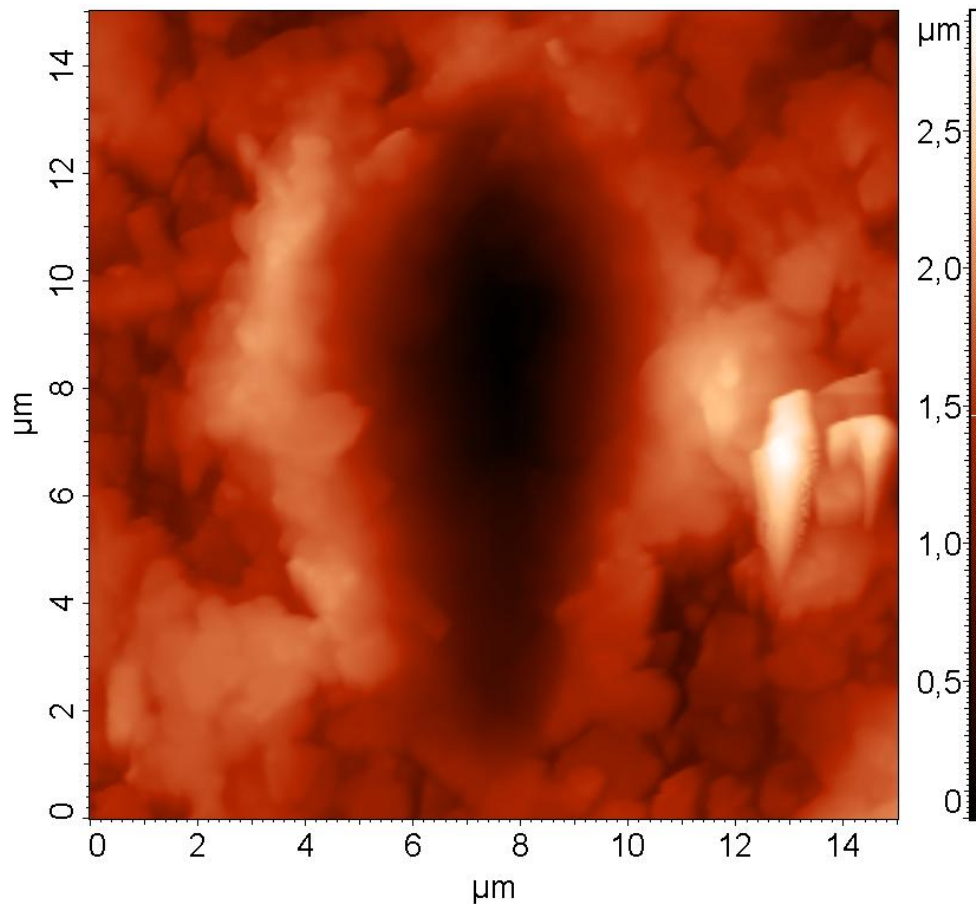


*Fig. 60: AFM image of nanoscratch performed at a maximum force of 5000  $\mu\text{N}$*

Scratch is 10  $\mu\text{m}$  long and approximately 7  $\mu\text{m}$  wide. Distribution of xGnP particles causes that value of width is so high. Exfoliated graphite nanoplatelets can be observed on the edges of the scratch. Tip pressed nanoparticles to left or right side (brighter areas along the scratch). Some particles were moved by tip deeper to the structure of the polymer. From these facts follows that 10 hours etched sample has not matrix on the surface. Nanoplatelets are movable on the surface and polymer is only under nanoparticles on some places. Depth of the scratch in the deepest place is approximately 2.2  $\mu\text{m}$ .

Plot of profile (height-width dependence) was performed on this place. Soft increasing of the height at the beginning can be seen, which is caused by presence of nanoparticles after scratching (Fig. 61). Shape of the tip and xGnP assembling from the picture is visible. All nanoparticles are assembled in the direction of the tip slope. It is not possible to evaluate mechanical properties of the nanocomposite foil from this information.

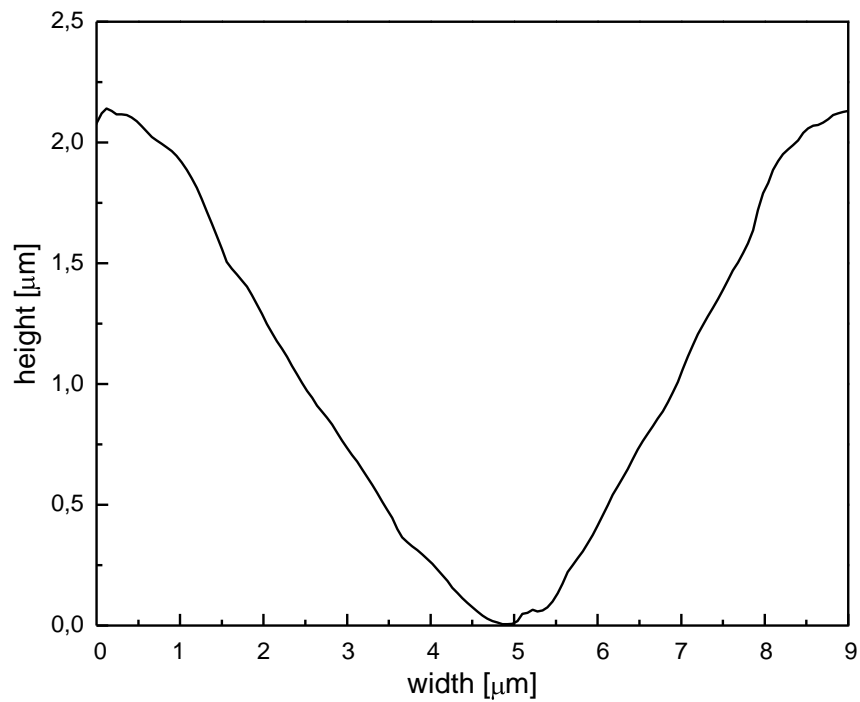


*Fig. 61: Show of profile from the middle of the scratch*

## 5.6 Wear test

Wear test was performed within nanoscratch test with the same tip. Area  $15 \times 15 \mu\text{m}$  was chosen and scanned with force  $80 \mu\text{N}$  six times. Scan of the area was performed after it. We can see scanned area on the Fig. 62. Damaged and not damaged area is compared on this picture.

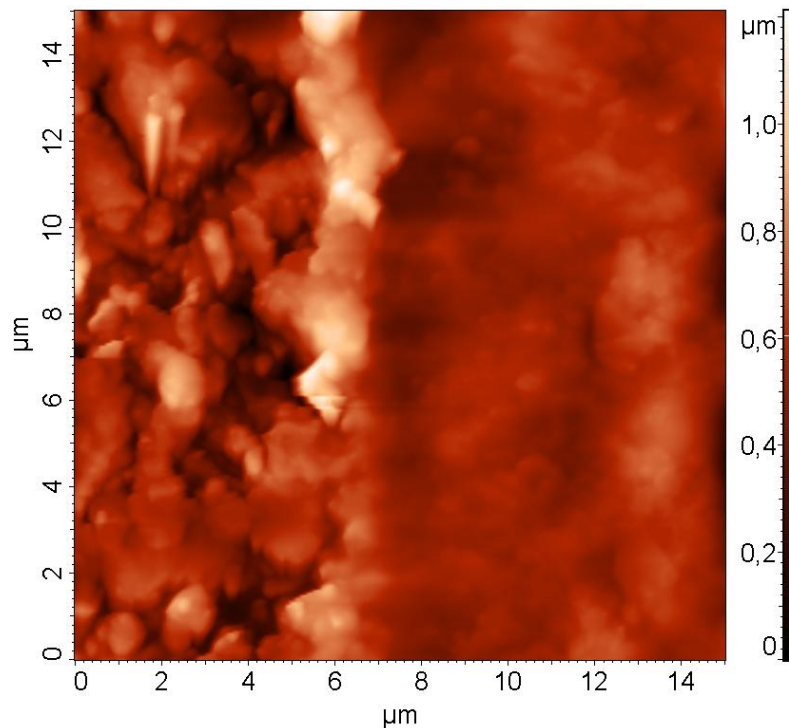


*Fig. 62: AFM image of damaged area (right half of image) by wear test*

Visible area with graphite nanoplatelets under various angles is on the left side. This area was not scanned by conospherical tip. Right side is damaged by conospherical tip. Tip moved some nanoparticles from this area and some particles were pushed to the polymer matrix and surface looks very plastic. Interface of damaged and not damaged area is visible. Graphite nanoplatelets are accumulated in the line. Reason why nanoparticles are movable is time of etching; this sample was etched 10 hours and polymer matrix PEI was completely removed from the surface and also from the space under nanosheets in some cases. That allowed moving of the particles with tip and pushing to the polymer.

## 6 CONCLUSION

This Diploma thesis dealt with surface analysis of nanocomposite foil, where poly(etherimide) was the matrix and exfoliated graphite nanoplatelets (xGnP) served as the reinforcement. Issues of surface analysis of xGnP were researched few times, but with other conventional polymers, for example high density poly(ethylene) (HDPE) [2], poly(propylene) (PP) [3], linear low density poly(ethylene) (LLDPE) [4] or ethylvinylacetate (EVA) [16] and many more. Analysis of xGnP/PEI nanocomposite was performed for the first time. The PEI foil without xGnP and agglomerates of xGnP on the silicon substrate was also observed within surface analysis. Plasma etching used argon gas was used for uncovering of xGnP. Etching was for various times. It allowed analysis of nanocomposite foil and influence of etching on the xGnP imaging. Nanoindentation was performed on the PEI foil and nanocomposite foil for indication of materials response and nanoscratch and wear test of etched nanocomposite for assessment of state of xGnP after scratch performing.

Etching times were chosen 0, 1, 3 and 10 hours on previous experience with argon and oxygen plasma used for polymer etching. Both the PEI and xGnP/PEI nanocomposite were etched. Polarization optical microscopy was used as the first method for preliminary indicating of xGnP on etched samples. Scanning electron microscopy was used for comparison of the structure of the PEI foil and times of etching and imaging of graphite nanoplatelets. Local places after etching are visible on the 10 hours etched PEI foil. Influence of etching is visible on nanocomposite foil. Some parts of nanoplatelets are covered by polymer both in the case of 1 hour etched sample and 3 hours etched sample. Ten hours of etching is enough time for uncovering of all exfoliated graphite nanoplatelets. Scanning electron microscope allowed imaging both of agglomerates and separate xGnP.

Atomic force microscopy was performed on samples of the PEI foil and nanocomposite foil. Prepared sample of separate xGnP was also analysed. Influence of etching time to the structure of the PEI foil and xGnP state, height imaging and separate xGnP imaging were observed. Both foils show increasing roughness properties with etching time. In the case of the PEI foil local etchings arose and increasing time led to widening of these etchings. Nanoparticles were uncovered in the case of nanocomposite foil. Increasing time of etching led to decline of polymer both on the surface of the foil and in the space among the nanoparticles. Values of root mean square, peak to peak and ACL values were established due the program Nova 1138 and plotted with etching time. Increasing trend both in the case of surveillance images  $50 \times 50 \mu\text{m}$  and detail images  $10 \times 10 \mu\text{m}$  can be seen. Separate xGnP were imaged. It consists from few graphene nanosheets and creates agglomerates with various shapes of the particles laid under various angles.

Atomic force acoustic microscopy was performed on 1 hour etched nanocomposite and height and magnitude signal were recorded. Surface of our nanocomposite is very rough for used cantilevers. This method did not give us required results about elastic response of nanocomposite.

Nanoindentation test was performed on not etched PEI foil and 3 hours etched nanocomposite foil. Three hours of etching for xGnP/PEI sample were chosen, because, polymer was removed from the surface, but not from the space among and under the nanoplatelets. Polymer under xGnP served as a support in this case. 10 hours etched sample had not matrix under xGnP, so results of nanoindentation would be not reproducible. Results showed that the PEI foil is tougher for all chosen forces, than in the case of

nanocomposite. Plot comparing maximal achieved forces shows bigger elasticity of nanocomposite foil in all cases, which was not expected. Reason could be angle, under which were xGnP in time of NI. Values of Young's modulus and hardness were evaluated for the PEI foil in Hysitron Triboscan program and plotted with contact depth. Average value of Young's modulus is  $(4.25 \pm 0.35)$  GPa and average value of hardness is  $(0.39 \pm 0.05)$  GPa.

Nanoscratch and wear tests were performed on 10 hours etched sample. Scratch showed moving of the xGnP to the edges of the path of scratch and pushing to the polymer matrix, as well as wear test, but area was scanned six times for deformation of the surface.

Scanning electron microscopy and atomic force microscopy were very useful methods for imaging of this material. Nanoindentation did not give us expected results. Particles in our nanocomposite have thickness approximately 50 nanometers. Particles prepared at MSU have thickness about 10 nm. [18] It is possible that in nanocomposite foil, are few xGnP particles together and create agglomerates. It leads to increasing of thickness. In my opinion, microindentation is more suitable method for characterization of mechanical properties. It was not possible to image indents by AFM due the averages of the particles.

Agglomerates of xGnP are also suitable for characterization by nano or microindentation and measurements could give us very interesting information about mechanical properties of very perspective reinforcement – xGnP.

## 7 REFERENCES

- [1] VENTA, M., EVOY, S., HEFLIN, J. R. *Introduction to Nanoscale Science and Technology*. Boston: Kluwer Academic Publishers, 2004. ISBN 1-4020-7720-3.
- [2] JIANG, X., DRZAL, L.T. Multifunctional High Density Polyethylene Nanocomposites Produced by Incorporation of Exfoliated Graphite Nanoplatelets 1: Morphology and Mechanical Properties. *Polymer Composites*. 2010 (48), 1091-1098.
- [3] KALAITZIDOU, K, FUKUSHIMA, H., DRZAL, L. T. A New Compounding Method for Exfoliated Graphite-Propylene Nanocomposites with Enhanced Flexural Properties and Lower Percolation Threshold. *Composites Science and Technology*. 2007 (67), 2045-2051.
- [4] KIM, S., DO, I., DRZAL, L. T. Thermal Stability and Dynamic Mechanical Behaviour of Exfoliated Graphite Nanoplatelets-LLDPE Nanocomposites. *Polymer composites*. 2010 (1226), 755-761.
- [5] BIJWE, J., RATTAN, R. Carbon Fabric Reinforced Polyetherimide Composites: Optimization of Fabric Content for Best Combination of Strength and Adhesive Wear Performance. *Wear*. 2007 (262), 749-758.
- [6] ADVANI, S. G. *Processing and Properties of Nanocomposites*, World Scientific, Singapore 2007, ISBN 981-270-390-X.
- [7] CECH, V. New Progress in Composite Interphases: A Use of Plasma Technologies. In: *FRC 2000 Composites for the Millennium*. University of Newcastle: Woodhead Publishing Ltd, 2000, s. 246-252.
- [8] HULL, D., CLYNE, T.W. *An Introduction to Composite Materials*. 2nd edition. United Kingdom, Cambridge: Cambridge University Press, 2003. 320 s. ISBN 0-521-38190-8.
- [9] SHARMA, M., RAO, I. M., BIJWE, J. Influence of Orientation of Long Fibers in Carbon Fiber-Polyetherimide Composites on Mechanical and Tribological Properties. *Wear*. 2009 (267), 839-845.
- [10] BOR, K. C., et al. Preparation of Polyetherimide Nanocomposites with Improved Thermal, Mechanical and Dielectric Properties. *Polymer Bulletin*. 57, s. 671-681.
- [11] KUMAR, S., et al. Dynamic Synergy of Graphitic Nanoplatelets and Multi-Walled Carbon Nanotubes in Polyetherimide Nanocomposites. *Nanotechnology*.
- [12] RATTAN, R., BIJWE, J. Influence of Impingement Angle on Solid Particle Erosion of Carbon Fabric Reinforced Polyetherimide Composite. *Wear*. 2007(262), 568-574.

- [13] LU, J., DO, I., FUKUSHIMA, H., LEE, I., DRZAL, L. T. Stable Aqueous Suspension and Self-Assembly of Graphite Nanoplatelets Coated with Various Polyelectrolytes. *Journal of Nanomaterials*. 2010(486), 1-11.
- [14] JAKESH, R., YOSHIMURA, M., K., KUMAR, A. Graphene. *Journal of Nanomaterials* 2010, 37.
- [15] KIM, S., DO, I., DRZAL, L. T. Multifunctional xGnP/LLDPE Nanocomposites Prepared by Solution Compounding Using Various Screw Rotating Systems. *Macromolecular Materials and Engineering*. 2009 (294), 196-205.
- [16] KIM, S., DRZAL, L. T. Comparison of Exfoliated Graphite Nanoplatelets (xGnP) and CNTs for Reinforcement of EVA Nanocomposites. Fabricated by Solution Compounding Method and Three Screw Rotating Systems. *Journal of Adhesion Science and Technology*. 2009 (23), 1623-1638.
- [17] XU, D., SRIDHAR, V., PHAM, T. T., KIM, J. K., Dispersion, Mechanical and Thermal Properties of Nano Graphite Platelets Reinforced Fluoroelastomer Composites. *E-Polymers*. 2008 (23), 1-19.
- [18] FUKUSHIMA, H., DRZAL, L. T., ROOK, B. P., RICH, M. J. Thermal Conductivity of Exfoliated Graphite Nanocomposites. *Journal of Thermal Analysis and Calorimetry*. 2006(85), 235-238.
- [19] HE, F., LAU, S., CHAN, H. L., FAN, J. High Dielectric Permittivity and Low Percolation Threshold in Nanocomposites based on a poly(vinylidene fluoride) and exfoliated graphite nanoplatelets. *Advanced materials*. 2009(21), 710-715.
- [20] KALAITZIDOU, K., FUKUSHIMA, H., MIYAGAWA, H., DRZAL, L. T. Flexural and Tensile Moduli of Polypropylene Nanocomposites and Comparison of Experimental Data to Halpin-Tsai and Tandon-Weng Models. *Polymer engineering and science*. 2007 (1002), 1796-1803.
- [21] HEATH, J.P. *Dictionary of Microscopy*. England: Chichester, 2005. ISBN 978-0-470-01199-7.
- [22] OHRING, M. *Materials Science of Thin Films: Deposition and Structure*. Department of Materials Science and Engineering, Stevens Institute of Technology, Hoboken, New Jersey: Academic Press, 2002. ISBN 0-12-524975-6.
- [23] MIRONOV, V. L. *Fundamentals of Scanning Probe Microscopy, The Textbook for Students of the Senior Courses of Higher Educational Institutions*, 1st edition The Russian Academy of Sciences, Nizhniy Novgorod, 2004, 98 s.

- [24] MEYER, E., HUG, H. J., BENNEWITZ, R. *Scanning Probe Microscopy The lab on a Tip*. 1st edition. New York: Springer, 2004. 207 s. ISBN 3-540-43180-2.
- [25] OLIVER, W. C., PHARR, G. M. An Introduction Technique for Determining Hardness and Elastic Modulus Using Load and Displacement Sensing Indentation Experiments. *Journal of Materials*. 1992, 7 (6), 1564-1582.
- [26] PRIKRYL, R., SALYK, O., VANEK, J., CECH, V. Czech. J. Phys. 52 (2002) D816.
- [27] TESCAN, a.s. Specification of the High Resolution Schottky FE SEM: MIRA 3 XMU. Brno, 2010.
- [28] NT-MDT. *Performing Measurements: AFM and STM measurements Spectroscopy, Many-pass techniques, Lithography*. Zelenograd, Russia, 2006.
- [29] HYSITRON INCORPORATED. *Triboscope User Manual*. Minneapolis, 2006.

## 8 LIST OF USED SYMBOLS AND ABBREVIATIONS

ACL	autocorrelation length function
AES	Auger electron spectroscopy
AFAM	atomic force acoustic microscopy
AFM	atomic force microscopy
Al	aluminium
Al <sub>2</sub> O <sub>3</sub>	aluminium oxide
BPADA	4,4'-(4,4'-isopropylidene diphenoxy) bis(phthalic anhydride)
BSE	back scattered electrons
C	carbon
Ca	calcium
CF	carbon fibres
CMCs	ceramic matrix composites
CNTs	carbon nanotubes
Cu	copper
DC	direct current
EFM	electric force microscopy
EVA	ethylvinylacetate
EG	expandable graphite
Fe	iron
Fe <sub>2</sub> O <sub>3</sub>	iron (III) oxide
Fe <sub>3</sub> O <sub>4</sub>	iron (II,III) oxide
FE-SEM	field-emission scanning electron microscopy
GaAs	gallium arsenide
GICs	graphite intercalation compounds
$\gamma_l$	surface energy of liquid
GO	graphite oxide
$\gamma_s$	surface energy of solid
$\gamma_{sl}$	surface energy of interface of solid and liquid
HDPE	high density polyethylene
Ir	irridium
KPM	Kelvin probe microscopy
LDPE	low-density polyethylene
LFM	lateral force microscopy
LLDPE	linear low density polyethylene
LVSTD	low vacuum secondary electron TESCAN detector
MBE	molecular beam epitaxy
MFM	magnetic force microscopy
MMCs	metal matrix composites
mPDA	m-phenylene diamine
MSU	Michigan State University
MWCNTs	multi wall carbon nanotubes

Na	sodium
Nb	niobium
NI	nanoindentation test
NS	nanoscratch test
O	oxygen
OM	optical microscopy
PAA	poly(amic acid)
PDAC	poly(diallyldimethylammonium chloride)
PEI	poly(etherimide)
PIs	Poly(imides)
PLD	pulsed laser deposition
PMMA	poly(methymetacrylate)
POM	polarization optical microscopy
PP	poly(propylene)
PS	poly(styrene)
Pt	platinum
PVD	physical vapor deposition
PZT	piezoelectric tube
$\theta$	contact angle
RF	radiofrequency
RMS	root mean square
sccm	standard cubic centimeters
SCM	scanning capacitance microscopy
SE	scattered electrons
SEM	scanning electron microscopy
SFM	scanning force microscopy
Si	silicon
SiC	silicon carbide
SIMS	secondary-ion mass spectroscopy
SiO <sub>2</sub>	silicon oxide
SPM	scanning probe microscopy
SPS	sulfated poly(styrene)
SWCNTs	single wall carbon nanotubes
TEM	transmission electron microscopy
W	tungsten
xGnP	exfoliated graphite nanoplatelets